The Dissertation Committee for Harish Potti certifies that this is the approved version of the following dissertation:

Seeing a single top quark: Search for $pp \to tq\gamma$ production and The combination of ATLAS searches for flavor changing neutral currents in $t \to Hq$ decays

Committee:

Peter Onyisi, Supervisor

Timothy R Andeen Jr

Karol Lang

Can Kilic

Matthew A Hersh

Seeing a single top quark: Search for $pp \to tq\gamma$ production
and
The combination of ATLAS searches for flavor changing neutral currents in $t \to Hq$ decays

by

Harish Potti

Dissertation
Presented to the Faculty of the Graduate School of
The University of Texas at Austin
in Partial Fulfillment
of the Requirements
for the degree of
Doctor of Philosophy

The University of Texas at Austin
December 2020

Dedicated to my parents: Vijaya Lakshmi Potti and Venkateswarlu Potti.

Acknowledgment

Completing this PhD is certainly the most challenging and adventurous task I have ever done. I would like to thank all the people, who have provided a great deal of support and assistance through the past six and half years.

I would always be indebted to my supervisor, Peter Onyisi, for showing me that doing physics is nothing but fun and adventure. Thank you, Peter, for giving me freedom to grow, but at the same time providing insightful feedback to sharpen my thinking. I have always found the scientific conversations we had on a wide range of topics to be engaging and stimulating. Overall, it's been an honor and a pleasure to work with you.

Next, I would like to express my gratitude to all the members of the UT ATLAS group, who are incredibly awesome and supportive. I would like to thank Tim Andeen for giving me an opportunity to work on the LAr upgrade project. I have greatly enjoyed the company of all the ATLAS graduate students, Aaron Webb, Avik Roy, Chuck Burton, Devanshu Panchal, Marc Tost, Mesut Unal, and would like to thank them for their companionship. I would also like to thank Rohin Narayan, Nikiforos Nikiforou, Yuriy Ilchenko, Kyungeon Choi, Tom Cartwright, Bryce Holloway, Dennis Lu, Mohammadali Ghaznavi, for being the absolute best colleagues. Special thanks to Ray Xu for helping me with electronics and FPGA programming.

I have thoroughly enjoyed my time as a member of the ATLAS collaboration at CERN. I wouldn't have been successful without the support from all the members of $t\bar{t}H \rightarrow$ multileptons, top quark properties and top + X subgroups. I would like to acknowledge my colleagues on the $tq\gamma$ project, Björn Wendland and Johannes Erdmann, for their wonderful collaboration. I would also like to appreciate the help provided by my colleagues on the FCNC analysis project, Aurelio Juste Rozas, Nicola Orlando, Robert Wolff, Jean-Baptiste de Vivie, Daniel Fournier, Xin Chen and Boyang Li.

I am immensely thankful to all my friends in Austin who made my time in UT

even more pleasurable. I would like to thank my flatmates - Debanjan Datta and Reetam Biswas. I also received an amazing support from Anamika Kumari, Prachi Singh, Shaleen Yadav, Rahul Verma, Vivek Khetan, Mukul Bhattacharya, Ajesh Kumar, Soumik Das, Sourav Sen, Hongfeng Yang, Dung Duc Phan, Sarbartha Banarjee, Manisha Banarjee and Pankaj Mishra.

Finally, none of this would have been possible without the support from my parents - Vijaya Lakshmi and Venkateswarlu. Their hard work and dedication is always an inspiration for me to be the best I can be. I would also like to thank my brother - Praveen and sister - Sirisha for always being there for me.

Seeing a single top quark: Search for $pp \to tq\gamma$ production
and
The combination of ATLAS searches for flavor changing neutral currents in $t \to Hq$ decays

Harish Potti, Ph.D.
The University of Texas at Austin, 2020

Supervisor: Peter Onyisi

The top quark is the heaviest known elementary particle. With a coupling to the Higgs boson close to unity, the top quark plays a special role in electroweak symmetry breaking as well as in physics beyond the Standard Model. An accurate measurement of its properties can provide key information for understanding the physics at the TeV scale. In this dissertation, two measurements of the top quark properties are presented.

The first part of this dissertation presents the first-ever ATLAS search for the associated production of a single top quark and a photon. This analysis is performed with 139 fb^{-1} of pp collision data collected by the ATLAS detector at the LHC at $\sqrt{s} = 13$ TeV. Only final states with exactly one lepton and at least one photon are considered in this analysis. Major backgrounds for the signal are $t\bar{t}\gamma$, $W\gamma$ and $t\bar{t}$. A deep learning, neural network approach is used for separating signal and background events. A binned profile likelihood fit is performed with neural network output as the discriminant. The expected best-fit value of the ratio of the observed $tq\gamma$ cross-section to that of the SM prediction is $1.0^{+0.14}_{-0.14} = 1.0\ ^{+0.05}_{-0.05}$ (stat.) $^{+0.13}_{-0.13}$ (syst.). This corresponds to an expected p-value of 6.5 σ for the no-signal hypothesis.

In the second part, results from the combination of ATLAS searches for flavor changing neutral currents (FCNC) in $t \to Hq$ decays are presented. Four FCNC

analyses, probing different Higgs decay modes, performed with 36.1 fb^{-1} of proton-proton collision data collected by the ATLAS detector in 2015-2016 are considered in the combination. They search for top-quark pair events in which one top quark decays into Wb and the other top quark decay into Hq. The targeted Higgs decay modes are: $\gamma\gamma, WW^*, \tau\tau, ZZ^*, b\bar{b}$. The combination of these searches yields observed (expected) 95% CL upper limits on the $t \to Hc$ and $t \to Hu$ branching ratios of 1.1×10^{-3} (8.3×10^{-4}) and 1.2×10^{-3} (8.3×10^{-4}), assuming $\mathscr{B}(t \to Hu)$ =0 and $\mathscr{B}(t \to Hc)$ =0 respectively. The corresponding combined observed (expected) upper limits on the $|\lambda_{tcH}|$ and $|\lambda_{tuH}|$ are 0.064 (0.055) and 0.066 (0.055) respectively. These results are the most restrictive direct bounds on tqH interactions measured to date.

Contents

List of Figures

List of Tables

Chapter One: Motivation

Particle Physics is the study of the nature of the fundamental building blocks that constitute our universe. The Standard Model (SM) of particle physics [1–3], constructed from our observations from centuries of experimental and theoretical research, is the most successful theory to date for understanding the elementary particles and their interactions. However, it is still considered as an incomplete theory as it can not explain many experimentally observed phenomenon like the existence of dark matter and dark energy, matter-antimatter asymmetry, etc. Precise measurements of all SM parameters and searches for physics beyond the SM are needed to further improve understanding of our universe.

Motivation for this dissertation is presented in this chapter following a brief summary and shortcomings of the SM.

1.1 Summary of the Standard Model

According to the SM, all known matter in the universe consist of spin $\frac{1}{2}$ particles, called fermions. Interactions between these fermions are mediated by the exchange of spin-1 particles, called gauge bosons.

1.1.1 Fermions

There are 12 fermions in the SM. Based on the color charge, these are classified into two groups of six particles, quarks (u, d, c, s, t, b) and leptons $(e^-, \mu^-, \tau^-, \nu_e, \nu_\mu, \nu_\tau)$. For each fermion in the SM, there is an anti-particle corresponding to it which has same mass and properties but opposite electric charge.
Leptons and quarks are further divided into three generations. All three generations are identical to each other except for mass and flavor quantum number. A fermion in the higher generation has greater mass than the corresponding particle of the lower

generation.
Each quark generation consists of an up-type quark and its down-type partner. Up-type quarks have an electric charge (Q) of $+\frac{2}{3}e$ and a weak isospin (T_3) of $+\frac{1}{2}$. For down-type quarks, $Q = -\frac{1}{3}e$ and $T_3 = -\frac{1}{2}$. Each lepton generation consist of a charged lepton ($Q = -e$ & $T_3 = +\frac{1}{2}$) and its corresponding neutrino ($Q = 0$ & $T_3 = -\frac{1}{2}$). In the SM, neutrinos are assumed to be massless particles.

1.1.2 Gauge bosons

In the SM, three types of fundamental interactions between fermions are described using four gauge bosons:

- Photons (γ) are the force carriers of the electromagnetic interaction. Photons are massless particles with $Q = 0$.
- $W^{\pm}$ and Z bosons mediate weak interaction. $W^{\pm}$ boson are electrically charged particles with mass = (80.379±0.012) GeV/c^2 and $Q = \pm 1e$ [4, 5]. Z bosons are neutral particles with mass = (91.1876±0.0023) GeV/c^2 [6, 7].
- Gluons (g) are the mediators of strong interaction between color carrying particles. They are massless particles with $Q = 0$. Gluons carry the color charge. Due to *color confinement*, they can not be observed in isolation.

Gravitational interaction is not included in the SM.

1.1.3 Higgs boson

The Higgs boson is the only elementary scalar particle in the SM. It plays a key role in the electroweak symmetry breaking, which explains how fundamental particles acquire mass [8–10].
The Higgs boson, the last unverified SM particle for several years, was discovered in 2012 by ATLAS and CMS experiments [11, 12]. The mass of the Higgs boson is (125.09 ± 0.21) GeV/c^2 [13]. It has no color charge and no electric charge.

1.1.4 Mathematical representation

Mathematically, the SM can be described using a quantum field theory in which all particles are represented as the excited states of more fundamental objects, called the *quantum fields*, that pervade space-time. The SM consists of the fermion fields (ψ), the electroweak boson fields (W_1, W_2, W_3 and B), the gluon field (G_a) and the higgs field (ϕ).

The dynamics of these fundamental fields are determined by the following Lagrangian density ($\mathcal{L}$), that exhibits the local $SU(3) \times SU(2) \times U(1)$ gauge symmetry as an internal symmetry,

$$\mathcal{L}_{\text{SM}} = -\frac{1}{4} F^a_{\mu\nu} F^{\mu\nu}_a + \bar{\psi}(i\not{D}\psi) + y_{ij}\bar{\psi}_i\psi_j\phi + |D_\mu\phi|^2 + \mu^2\phi^\dagger\phi - \lambda(\phi^\dagger\phi)^2 \tag{1.1}$$

Where, $F^a_{\mu\nu} = \partial_\mu A^a_\nu - \partial_\nu A^a_\mu + g f^{abc} A^b_\mu A^c_\nu$,
$\not{D} = \gamma^\mu D_\mu$ and $D_\mu = \partial_\mu - igA^a_\mu t^a$.
Here, $F^a_{\mu\nu}$ represents the field strength tensor for a specific gauge field A with gauge coupling constant g. The structure constants for a given gauge group, represented in above equation as f^{abc}, are determined from the commutation between the generators (t^i) of that group, i.e., $[t^a, t^b] = if^{abc}t^c$.
The Yukawa coupling, y_{ij}, describes the strength of the interaction between the higgs field and the fermion field. The values of the parameters λ and μ signify the strength of the interaction of the Higgs boson with itself.

1.2 Successful predictions of the SM

All particles of the SM and their properties are summarized in Table 1.1. With just this concise particle composition, the SM has been enormously successful in predicting many experimental phenomena. It predicted the existence and properties of many particles like W and Z bosons, Higgs boson, top quark, charm quark and tau neutrino before they were observed. Experimental confirmation of these particles demonstrated the phenomenal predictive power of the SM.
Figure 1.1 shows the comparison of the SM predictions and the ATLAS measurements of production cross-sections for various physics processes at $\sqrt{s}$ = 7, 8 and 13 TeV. The agreement between them, with cross-section values spanning over 15 orders of

Type	Generation	Particle	Mass	Spin	Color	I_3	Q	Y
Leptons	1	Electron neutrino (ν_e)	0	1/2	–	+1/2	0	-1/2
		Electron (e^-)	511 keV	1/2	–	-1/2	-1	-1/2
	2	Muon neutrino (ν_μ)	0	1/2	–	+1/2	0	-1/2
		Muon (μ^-)	105.7 MeV	1/2	–	-1/2	-1	-1/2
	3	Tau neutrino (ν_τ)	0	1/2	–	+1/2	0	-1/2
		Tau (τ^-)	1.78 GeV	1/2	–	-1/2	-1	-1/2
Quarks	1	Up quark (u)	2.16 MeV	1/2	Triplet	+1/2	+2/3	+1/6
		Down quark (d)	4.67 MeV	1/2	Triplet	+1/2	-1/3	+1/6
	2	Charm quark (c)	1.27 GeV	1/2	Triplet	+1/2	+2/3	+1/6
		Strange quark (s)	93 MeV	1/2	Triplet	+1/2	-1/3	+1/6
	3	Top quark (t)	172.76 GeV	1/2	Triplet	+1/2	+2/3	+1/6
		Bottom quark (b)	4.18 GeV	1/2	Triplet	+1/2	-1/3	+1/6
Bosons		Photon (γ)	0	1	–	0	0	0
		Gluon (g)	0	1	Octet	0	0	0
		$W^\pm$ boson	80.38 GeV	1	–	$\pm$ 1	$\pm$ 1	0
		Z boson	91.19 GeV	1	–	0	0	0
		Higgs boson (H)	125.10 GeV	0	–	-1/2	0	+1/2

Table 1.1: Properties of all Standard Model particles. Particle masses are extracted from the Particle Data Group website (2020) [14].

magnitude at 3 different energy scales, illustrates yet another remarkable success of the SM.

1.3 Open questions in Particle Physics

The SM, despite being successful in explaining many physics phenomenon, is considered as an insufficient theory due to many limitations. Some shortcomings of the SM are listed below.

- **Baryon asymmetry**: Equal amounts of baryonic matter and antibaryonic matter should have been created in the early universe from the big bang. However, experimental observations indicate that our observable universe is dominated by baryonic matter [16]. This asymmetry can not be explained by the SM.

- **Dark matter and Dark energy**: Cosmological observations indicate that the

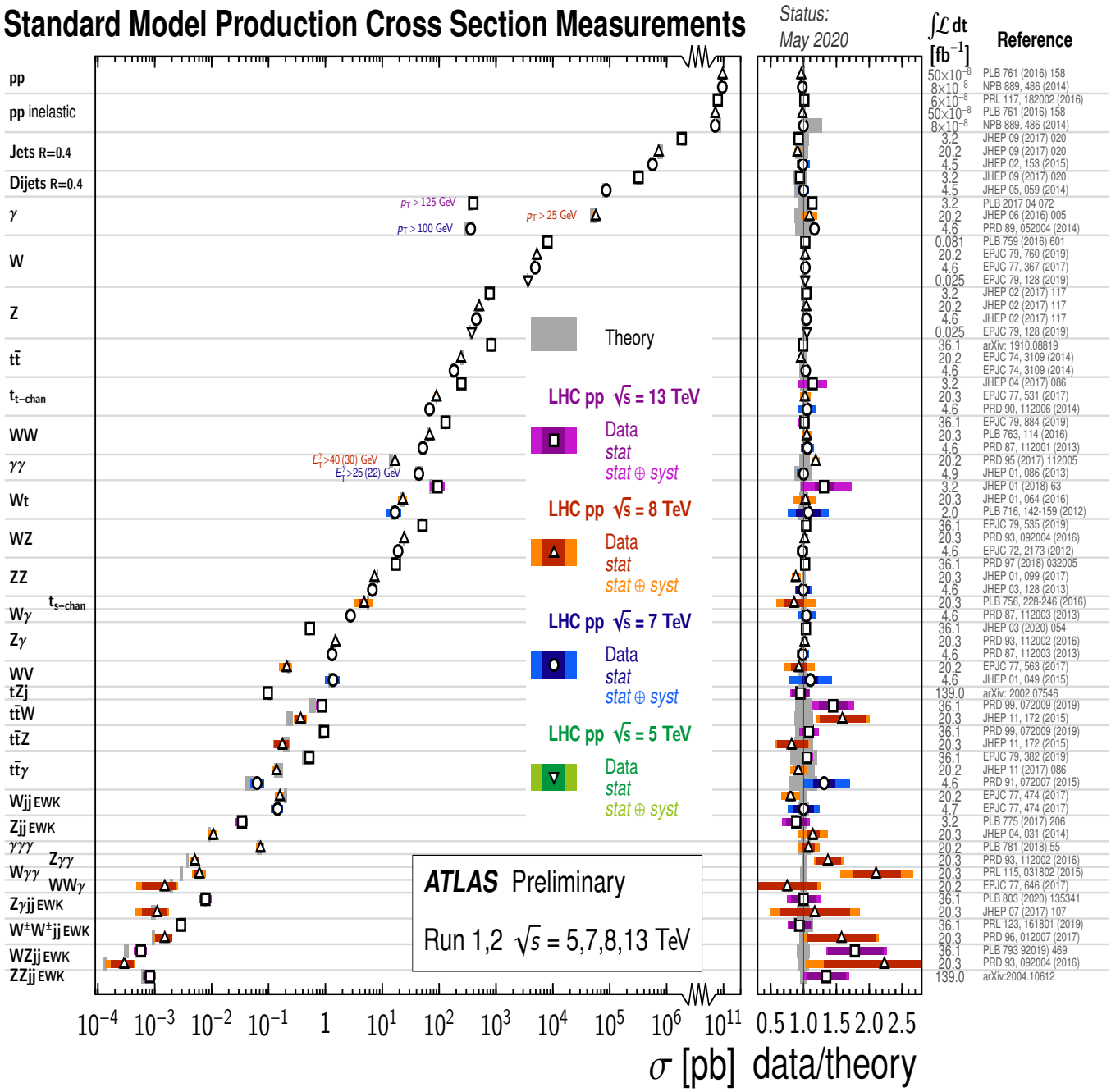

Figure 1.1: Production cross-sections of various processes measured by the ATLAS experiment at $\sqrt{s} = 7$, 8 and 13 TeV, compared to the corresponding SM predictions. Figure taken from Ref. [15].

total mass-energy of the universe contains 5% ordinary matter and energy that is described by the SM, 27% dark matter and 68% dark energy [17–20]. The SM does not have any elementary particles that can describe the observed dark matter. Physics behind the dark energy is unknown.

- **Origin of neutrino mass**: In the SM, neutrinos are massless particles. However, neutrino oscillation experiments have shown that at least two flavors of neutrinos have a non-zero mass [21]. This can be fixed by adding Majorana neutrino mass terms to the SM Lagrangian. The problem with this is that the neutrino masses are extraordinarily small ($\sim 10^5$ smaller) compared to other known particles.

- **Dark matter and Dark energy**: Cosmological observations indicate that the total mass-energy of the universe contains 5% ordinary matter and energy that is described by the SM, 27% dark matter and 68% dark energy [17–20]. The SM does not have any elementary particles that can describe the observed dark matter. Physics behind the dark energy is unknown.

- **Origin of neutrino mass**: In the SM, neutrinos are massless particles. However, neutrino oscillation experiments have shown that at least two flavors of neutrinos have a non-zero mass [21]. This can be fixed by adding Majorana neutrino mass terms to the SM Lagrangian. However, the origin of the Majorana mass terms is unknown.

- **Gravity** The SM does not include the description of the gravitational force. Extending the SM, simply by adding a graviton, a hypothetical mediator particle for gravitational interaction, does not work as the mathematical framework of the SM is incompatible with the general theory of relativity.

1.4 Search for New Physics

There is no single way to address these open questions. Two popular approaches taken by the collider physicists to answer them are:

- **Precision measurements of Standard Model parameters:** The precision measurements of all particle properties provide an important test for the

SM predictions. Any deviations in measurements from predictions will provide indirect information about the new physics.

- **Search for new particles/interactions predicted by beyond Standard Model theories:** There are many beyond the Standard Model (BSM) theories like supersymmetric models, the Two-Higgs-doublet model [22], which provide elegant solutions to the open questions listed in section 1.3. In this approach, validity of those BSM theories are tested by directly searching for the new particles and/or interactions predicted by them.

In the past 6.5 years, I have contributed to analyses related to both of the previously mentioned approaches. The first part of this dissertation presents the search for the production of a single top quark in association with a photon. In Part II, a search for flavor changing neutral currents in $t \to Hq$ decays is presented.

Chapter Two: The Experimental Setup

The work described in this thesis is done using the data collected by the ATLAS experiment at the Large Hadron Collider (LHC) at CERN. In this chapter, a technical overview about the LHC and the ATLAS experiment is presented.

2.1 The Large Hadron Collider

The Large Hadron Collider (LHC) [23] is a circular particle accelerator at the European Organization for Nuclear Research (CERN). It is 27 km in circumference and located 100 m beneath the French-Swiss border, just outside of Geneva, Switzerland [24, 25]. Four major experiments are located along the LHC: ALICE [26], ATLAS [27], CMS [28] and LHCb [29]. The ATLAS and CMS are general purpose detectors, i.e., they are built for probing broad range of physical processes, whereas the ALICE and LHCb are specialized detectors designed for probing heavy-ion physics and b-hadron physics, respectively.

2.1.1 The LHC Injection Chain

The proton beams pass through a series of small accelerator systems, referred to as the LHC *injector chain* [30], before they are introduced into the LHC ring. The accelerator systems of the LHC injection chain are depicted in Figure 2.1.

The proton beams are created by ionizing the hydrogen atoms with an intense electric field. They are first passed through Linac-2, a linear accelerator, which accelerates the protons to 50 MeV. They then enter the first circular accelerator, the Proton Synchrotron Booster (PSB), to attain an energy of 1.4 GeV. They are subsequently accelerated up to 25 GeV by the Proton Synchrotron (PS), and to 450 GeV by the Super Proton Synchrotron (SPS). Finally, proton beams are injected into the LHC in two separate beams travelling in opposite directions. Inside the LHC

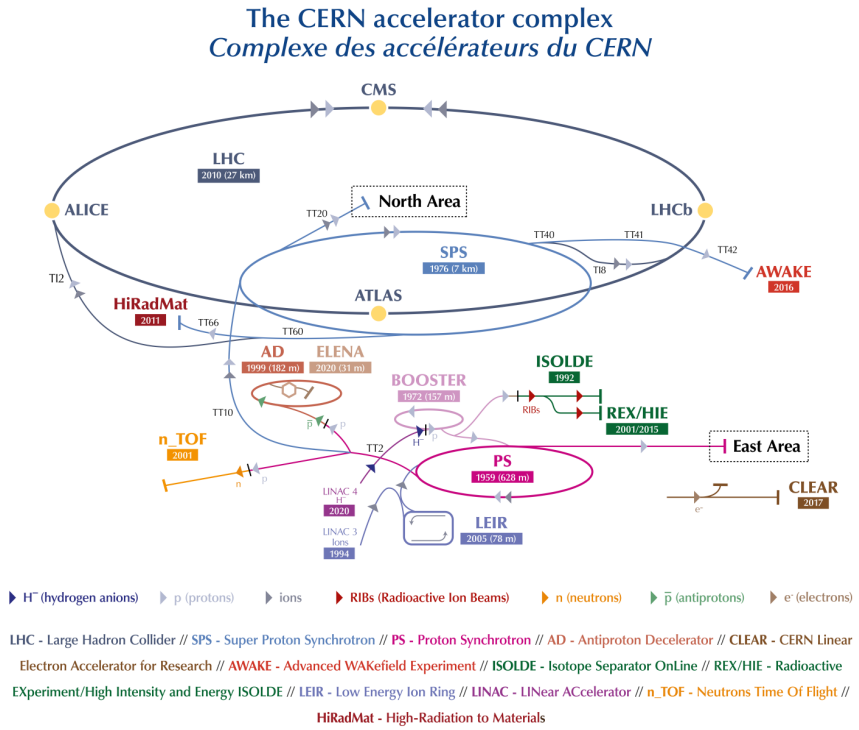

Figure 2.1: The chain of particle accelerators at the CERN accelerator complex that is used for boosting the proton beams to a center-of-mass energy of $\sqrt{s} = 13$ TeV. Figure taken from Ref. [31].

ring, super conducting radio-frequency (RF) cavities are used to accelerate the proton beams up to a center of mass energy of $\sqrt{s} = 14$ TeV [32]. The LHC magnet system also consists of 1232 dipole magnets to guide the beam around the ring and 392 quadrupole magnets to focus the beam. They are made of superconducting coils of Niobium-Titanium (NbTi) alloy and provide a magnetic field of up to 8.3 T. As NbTi behaves as a superconductor only for temperatures below 10 K, the LHC magnets are housed in cryostats filled with superfluid Helium operated at a temperature of 1.9 K. In total, the LHC uses approximately 120 tonnes of superfluid Helium, making it the largest cryogenic facility in the world.

2.1.2 Bunch Structure and Luminosity

The proton beams at the LHC are not a continuous stream of protons, instead, they are grouped into *bunches*. At full intensity, each LHC beam consists of 2808 bunches of protons spaced by 25 ns, with 1.15×10^{11} protons in each bunch.

The number of collision that can be produced per cm^2 per second is measured using a quantity known as the *instantaneous luminosity* [33], defined by the following equation:

$$\mathcal{L} = \frac{N_b^2 n_b f_{\text{rev}} \gamma}{4\pi\sigma_x\sigma_y} F \tag{2.1}$$

where N_b is the number of protons in each bunch, n_b is the number of bunches, f_{rev} is the bunch revolution frequency, σ_x and σ_y are the horizontal and vertical beam size and F is the geometric reduction factor due to non-zero crossing-angles of the colliding beams.

The LHC is designed to provide a maximum instantaneous luminosity of 1×10^{34} cm^{-2} s^{-1}. However, it exceeded the design goal by achieving an instantaneous luminosity of 2.1×10^{34} cm^{-2} s^{-1} in 2018. The total luminosity delivered by the LHC, referred to as the *integrated luminosity*, can be obtained from the integral of instantaneous luminosity with respect to time.

$$L = \int \mathcal{L} dt. \tag{2.2}$$

The integrated luminosity is useful in predicting the number of collision events (N_i) that produce a specific physics process with cross-section σ_i, using

$$N_i = L\sigma_i. \tag{2.3}$$

The integrated luminosity is typically expressed in *inverse femtobarns* (fb^{-1}), where 1 fb = 10^{-39} cm^{-2}.

One consequence of high instantaneous luminosity is the occurrence of multiple *pp* interactions at the same time. This is quantified with the average number of interactions per bunch crossing $< \mu >$, referred to as the *pileup*. It can be caused by

additional *pp* interactions within the same bunch crossing (*in-time* pileup) or neighboring bunch crossings (*out-of-time* pileup). The pileup scales with instantaneous luminosity, via the relation:

$$< \mu >= \frac{\mathcal{L}\sigma_{\text{inelastic}}}{n_b f_{\text{rev}}}. \tag{2.4}$$

As the pileup causes additional energy deposits in the detector, it degrades the the performance of the ATLAS object reconstruction algorithms.

2.1.3 LHC Run-2 performance

During Run-2 data taking period, the LHC delivered 156 fb^{-1} of *pp* collisions, out of 139 fb^{-1} of data were recorded by the ATLAS experiment with stable beams and detector conditions. Cumulative integrated luminosity delivered to the ATLAS experiment as a function of time is presented in Figure 2.2. The pileup ($< \mu >$) distribution for each year of Run-2 data taking period is shown in Figure 2.3.

2.2 The ATLAS experiment

A Toridal LHC ApparatuS (ATLAS), located at the Point-1 on the LHC ring, is a general purpose detector built for probing p-p and Pb-Pb collisions. It is designed to discover the Higgs boson and to search for the physics beyond the SM. The ATLAS detector is cylindrical in shape, with a length of 25 m, a diameter of 44 m and weighing about 7000 tonnes. It is coaxial with beam line and forward-backward symmetric with respect to the interaction point. The ATLAS detector is hermetic and provides a coverage of near 4π radians in solid angle around the interaction point.

To identify a wide variety of final state particles and topologies, the ATLAS detector is designed as a nesting of several sub-detector systems, each of which are optimised for the measurement of different particles. Each sub-detector system is composed of a barrel system, centered around the interaction point, and an end-cap system placed further along the beam axis. The inner detector (ID), which consists of silicon and transition-radiation based detectors, is closest to the beam pipe. It

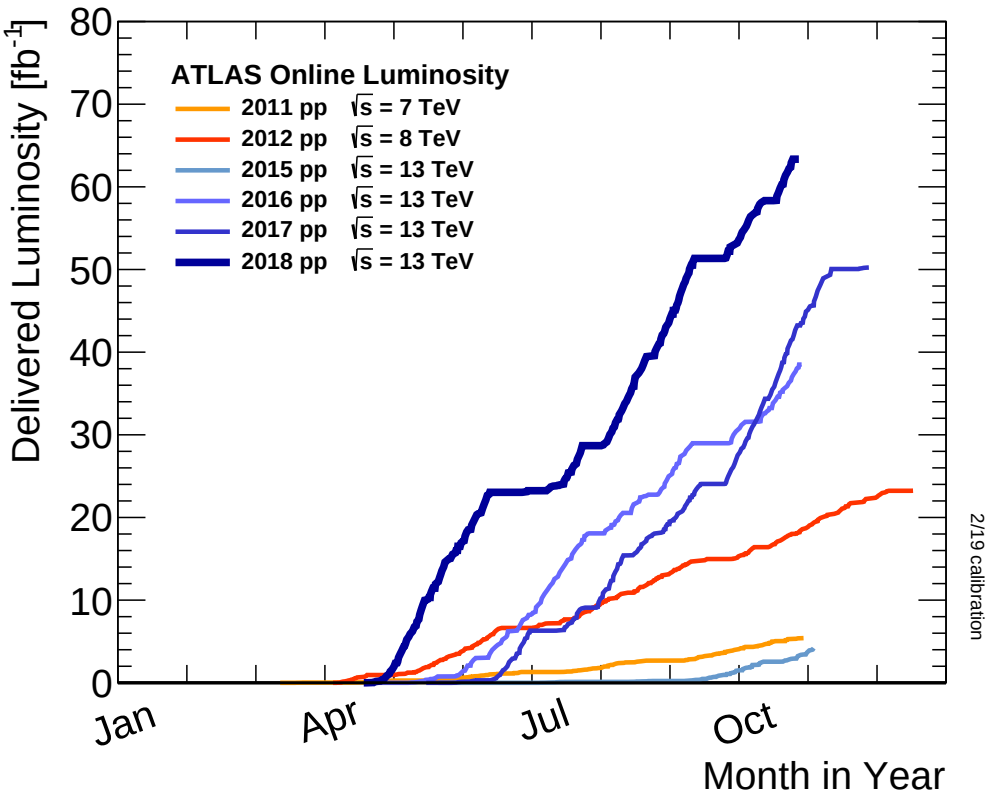

Figure 2.2: Cumulative integrated luminosity delivered to the ATLAS experiment by year for high energy *pp* collisions.

is used for tracking, momentum and vertex measurements, electron identification. The electromagnetic and hadronic calorimeters, which surround the ID, allow the measurement of energies of electrons, photons and hadrons through their electromagnetic and hadronic showers. Finally, the muon spectrometer, outermost layer of the ATLAS detector, allows the tracking and triggering of muons. A schematic of the ATLAS detector is shown in Fig. 2.5.

2.2.1 Coordinate system

The ATLAS detector uses a right-handed coordinated system. The interaction point, where the two proton beams cross-over, is designated as the origin of the coordinate system. The z-axis is defined by the beam direction. The positive x-axis points to-

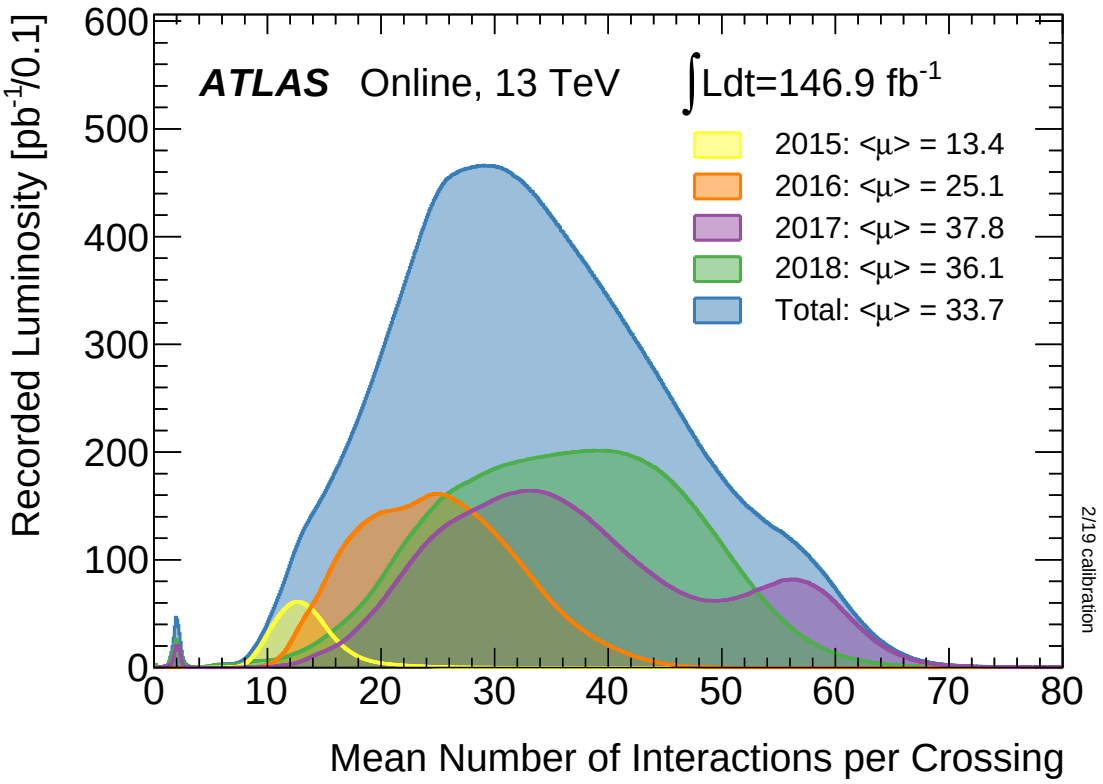

Figure 2.3: Average number of pp interactions per bunch crossing (μ) during Run-2 data taking period.

wards the center of the LHC ring and the positive y-axis points upwards. The side of the detector in the positive z-direction is labelled as the side-A, while the side in the negative z-direction is labelled as the side-C. The azimuthal angle ϕ is measured around the z-axis, such that $\phi = 0$ along the positive x-axis. The polar angle θ is measured with respect to the z-axis.

The momentum of an object in the direction i is labelled as p_i and the total energy is labelled as E. The transverse momentum (p_T) and the transverse energy (E_T) are defined by the momentum and the energy in the x-y plane respectively. The rapidity y of an object is defined as

$$y = \frac{1}{2}\frac{E + p_z}{E - p_z}. \tag{2.5}$$

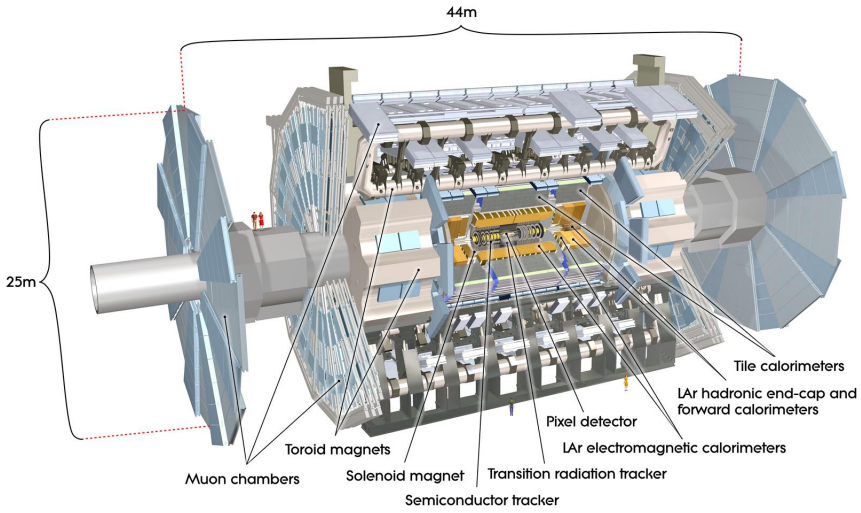

Figure 2.4: Illustration of the ATLAS detector with its sub-detectors. Figure taken from Ref. [27].

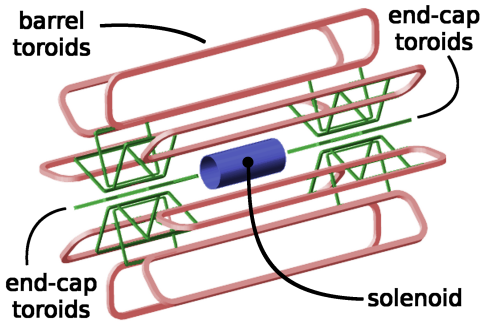

Figure 2.5: The layout of the ATLAS magnetic system. Figure taken from Ref. [34].

If the object is massless or ultra-relativistic ($m << p_T$), then the rapidity of the object will be equivalent to its pseudorapidity η, defined as

$$\eta = -\ln tan(\theta/2). \tag{2.6}$$

The distance between two objects in the pseudorapidity - azimuthal angle plane, denoted by ΔR, is defined as

$$\Delta R = \sqrt{\Delta\phi^2 + \Delta\eta^2}. \tag{2.7}$$

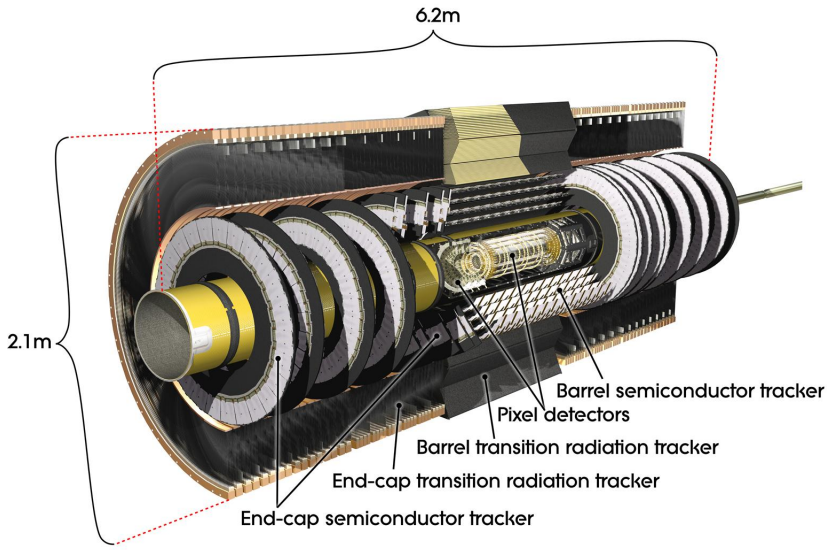

Figure 2.6: A cross-sectional view of the ATLAS inner detector. Pixel, SCT and TRT detectors are shown for barrel and endcap regions. Figure extracted from Ref. [27].

2.2.2 Inner Detector

The Inner Detector is designed to measure the trajectories of the charged particles with $p_T > 0.5$ GeV and $|\eta| < 2.5$ [35]. It is located inside a central solenoid, which produces a 2 T magnetic field and extends over a length of 5.3 m with a diameter of 2.5 m. The magnetic field in the z-direction produced by the solenoid, bends the incoming charged particles in the $x - y$ plane, providing information necessary for measuring the momentum. As shown in Figure 2.6, the ID is composed of three sub-detectors, listed in order of increasing radial distance from the beam line: the Pixel detector, the Semiconductor Tracker (SCT), and the Transition Radiation Tracker (TRT). These detectors allow the reconstruction of tracks associated with 1000 charged particles emerging from each proton-proton collision occurring at every 25 ns. A cut-away view of the inner detector is presented in Figure 2.7.

2.2.2.1 The Pixel detector

The Insertable B-Layer (IBL), located at a radius of 33.25 mm, is the innermost layer of the Pixel detector [36]. It was installed before the beginning of Run-2 data

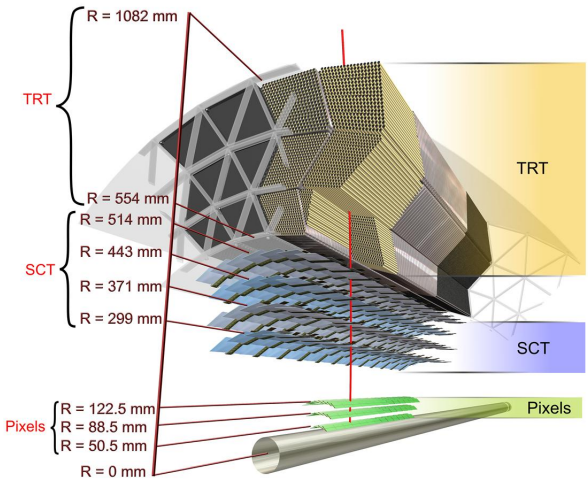

Figure 2.7: A cut-away view of the ATLAS inner detector. Radial distance for all layers of pixel, SCT and TRT detectors is indicated. Figure extracted from Ref. [27].

taking period to improve the spatial resolution and the vertex reconstruction in the high-pileup environment. It alone has 8 million readout channels, with each pixel consisting of reverse-biased n-type silicon semiconductor material with size of 50 $\times$ 250 μm^2 in the $R-\phi$ $\times z$ plane. IBL provides a spatial resolution of 8 μm in the $x-y$ plane and 40 μm along z-axis.

After the IBL, the Pixel detector is arranged as three co-axial cylinders in the barrel region and three disks perpendicular to the z-axis in the endcap regions. The cylinders in the barrel region are at distances of R = 50.5, 88.5, 122.5 mm and the disks in the endcap are at z = 495, 580, 650 mm. In total, the last three layers of the Pixel detector consists of 1744 sensors with 80 million readout channels. Each pixel has a size in $R-\phi$ $\times z$ of 50 $\times$ 400 μm^2 and provides a spatial of resolution of 10 μm in the $x-y$ plane and 115 μm along the z-axis.

2.2.2.2 The Semiconductor Tracker

The Semiconductor Tracker (SCT) surrounds the Pixel detector and uses the same technology based on the Silicon sensors. It consists of 4 cylindrical layers in the barrel region and 9 disks perpendicular to the z-axis in the endcap regions. The cylindrical layers in the barrel region are located at $R = 299$, 371, 443, 514 mm, while the disks in the endcap regions are in the range [854, 2720] mm along the z-axis. The silicon sensors are in a 2-D strip-like geometry with each strip having a length of 12 cm and a pitch of 80 μm. In total, the SCT has 15912 sensors with 768 strips in each sensor, thus, corresponding to a total of $\sim$ 6.3 million readout channels. The SCT provides a spatial hit resolution of 17 μm in the $R - \phi$ plane and 580 μm along the z direction.

2.2.2.3 The Transition Radiation Tracker

The Transition Radiation Tracker (TRT) is the outermost part of the ID that surrounds the SCT. It consists of straw drift tubes with a diameter of 4 mm, and covers the region up to $|\eta| = 2.0$. Each straw tube, made from polyimides, is filled with a gas mixture of 70% Xe - 27% CO_2 - 3% O_2. A 31 μm diameter tungsten wire plated with gold is placed in each straw tube at its center. These wires, connected to the ground potential, act as anodes. While, the inner walls of each tube, operated at $\sim$ 1530 V, act as cathodes, resulting in a gain of 2.5×10^4. When a charged particle strikes the drift tube, it ionizes the gas and the electrons drift towards the wire while the ions drift to the walls. As the electrons approach the wire, an avalanche of electrons is induced due to the large potential difference between the wire and the walls. This induced current provides the timing information.

In the barrel region, the TRT is composed of 73 layers of 144 cm long straw tubes parallel to the z-axis. They are located in the region 563$< R <$1066 mm with $z <$712 mm. While in the each end-cap region, the TRT contains 80 layers of straw tubes of 37 cm long arranged radially in wheels. In the barrel region, the tungsten wires are divided into two halves at $\eta = 0$.

Additionally, a polypropylene-polyethylene fibre mat of thickness 3 mm is embedded between each straw tube. Charged particles traversing through the mats will

have a probability of emitting transition radiation as they are moving between media with different index of refraction. Since the transition radiation is proportional to the Lorentz factor γ, it will be higher for electrons due to their low masses than for pions and muons. This difference in response is a crucial information for discriminating electrons and pions and for enhancing the performance of ATLAS electron identification algorithms.

Overall, the TRT contains approximately 351,000 readout channels. It is capable of providing information in $r - \phi$ coordinates only (no z information), with a straw hit resolution of 130 μm. The hit resolution of the TRT is worse when compared with the Pixel or the SCT, however it is compensated by the large number hits per track in this sub-detector. Typically, a charged particle leaves 36 hits in the TRT.

2.2.3 Calorimeters

The ATLAS calorimeter system is situated outside of the ID and the central solenoid. As illustrated in Figure 2.8, it consists of two types of calorimeters: Electomagnetic Calorimeter to detect and measure the energy of electrons and photons; Hadronic Calorimeter to measure and absorb the energy from hadronic showers. Both calorimeters are sampling calorimeters, i.e., they consist of alternating layers of absorbers and active material. The absorber layer produces showers from incoming particles, while, the active layer measures the energy of the resulting shower.

2.2.3.1 Electromagnetic Calorimeter

The ATLAS Electromagnetic Calorimeter (ECAL) uses liquid argon as the active material, lead as the absorber, and is refered to as the Liquid Argon (LAr) Calorimeter [37]. When high-energy electrons interact with lead, they lose energy through scattering and by emitting Bremsstrahlung photons. These photons then convert into e^+e^- pairs, creating a "shower" as the process continues. When the resulting electrons and photons interact with LAr in the active layer, they cause ionization. These ionization signals are then measured using the interleaved readout electrodes. Readout electrodes, made of copper, are operated at a voltage of 2kV and are placed

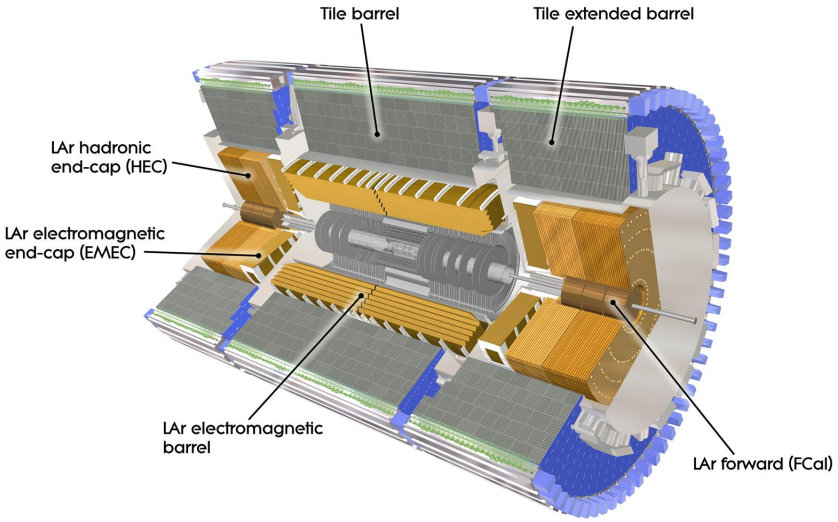

Figure 2.8: Schematic of the ATLAS calorimeter system. Different sub-systems are used in barrel, end-cap and forward regions. Figure taken from Ref. [27].

at a distance of 2.1 mm from the absorbing material.

The ECAL is designed in an accordion geometry to provide a complete coverage in ϕ. It is composed of a a barrel part ($|\eta| < 1.475$) and two end-cap sections ($1.375 < |\eta| < 3.2$). The barrel calorimeter is divided into two identical half-barrels, separated by a gap of 4 mm at $z = 0$. A cut-away view of the barrel LAr calorimeter is presented in Figure 2.9.

In the end-cap regions, the LAr calorimeter is divided into two coaxial wheels. The outer wheel covers the region $1.375 < |\eta| < 2.5$, while the inner wheel covers the region $2.5 < |\eta| < 3.2$.

The barrel part of the calorimeter is split into three layers, each with different thickness, depth and granularity. The first layer has a thickness of $4.3X_0$. Here, X_0 represents the radiation length, the distance in a given material over which an electron or a photon loses all but $1/e$ of its energy. The first layer is finely segmented into high granularity strips in the η direction, to distinguish single photons showers from those arising due to $\pi^0 \to \gamma\gamma$ decays. The second layer has a thickness of $16X_0$

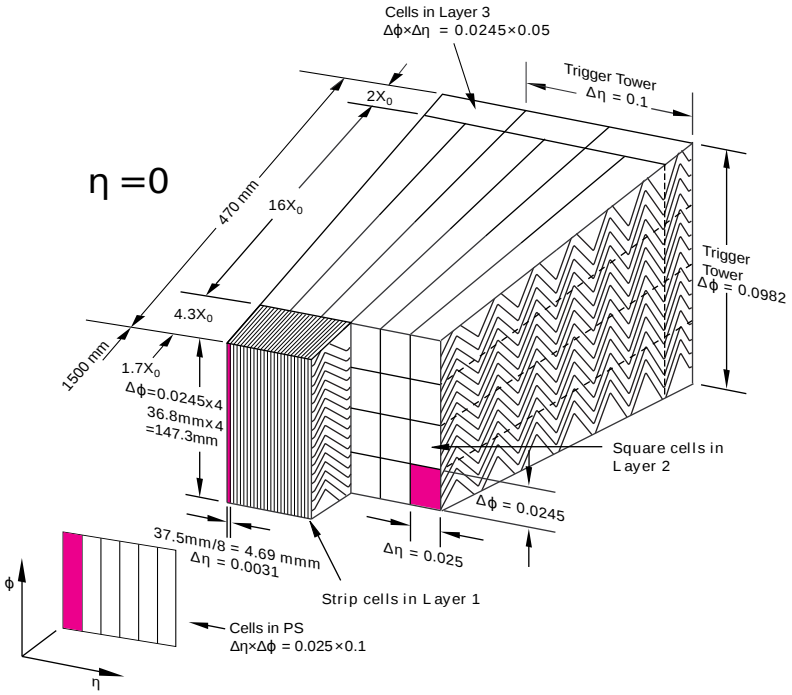

Figure 2.9: A view of the barrel LAr calorimeter. It has accordion geometry and contains three sampling layers. Absorption properties and granularity in $\Delta\phi \times \Delta\eta$ for each layer are indicated. Figure taken from Ref. [37].

and collects the majority of the EM shower energy. Finally, the third layer has a thickness of $2X_0$. It is used to correct for the leakage of EM shower energy into the Hadronic calorimeter.

Additionally, a pre-sampler detector is used in the region $|\eta| < 1.8$, to correct for energy lost by electrons and photons upstream of the ECAL. It consists of an active layer of LAr with a thickness of 1.1 cm (0.5 cm) in the barrel (end-cap) region.

2.2.3.2 Hadronic Calorimeter

The Hadronic Calorimeter system (HCAL) consists of two different calorimeters: a scintillating Tile Calorimeter and a Hadronic End-cap Calorimeter based on LAr-technology.

The Tile calorimeter is placed just outside the ECAL [38]. It consists of a barrel section covering the region $|\eta| < 1.0$ and two extended barrel sections covering the range $0.8 < |\eta| < 1.7$. It is a sampling calorimeter which uses tiles of steel as the absorber and tiles of scintillating plastic as the active material. The steel tiles produces hadronic showers when high-energy hadrons traverse through them, while the plastic tiles generate a light signal that is proportional to the number of minimum ionizing particles in the showers. These light signals are read-out by wave-length shifting fibers and delivered to photomultipliers. The tile calorimeter extends the region $2.28 < r < 4.25\ m$ and is segmented into three layers. They have a depth of 1.5, 4.1 and 1.8 interaction lengths (λ) in the barrel section and 1.5, 2.6, and 3.3 λ in the extended barrel sections.

The Hadronic End-cap Calorimeter (HEC) consists of two independent wheels in each end-cap section and covers the region $1.5 < |\eta| < 3.2$. It uses copper as the absorber and LAr as the active material.

2.2.3.3 Forward Calorimeters

To extend the coverage of the calorimetric system, a Forward Calorimeter (FCAL) system is used in the region $3.1 < |\eta| < 4.9$ [39]. As shown in Figure 2.10, it is composed of three layers in the z-direction: an electromagnetic layer (FCAL 1) and two hadronic layers (FCAL 2 & FCAL 3). All three layers use LAr is used as the active material. The EM layer uses Copper as the absorber, while the hadronic layers use tungsten as their absorber.

2.2.4 Muon spectrometer

The Muon Spectrometer (MS) is the outermost layer of the ATLAS detector and also the largest sub-system by volume [40]. It is designed to measure the momentum of muons in the region $|\eta| < 2.7$ and to trigger on these particles in the region $|\eta| < 2.4$. A large superconducting air-toroid magnetic system is used to deflect muons for measuring their momentum from the curvature. It consist of a large barrel toroid covering the region $|\eta| < 1.4$ and two end-cap toroids in the range $1.6 < |\eta| < 2.7$.

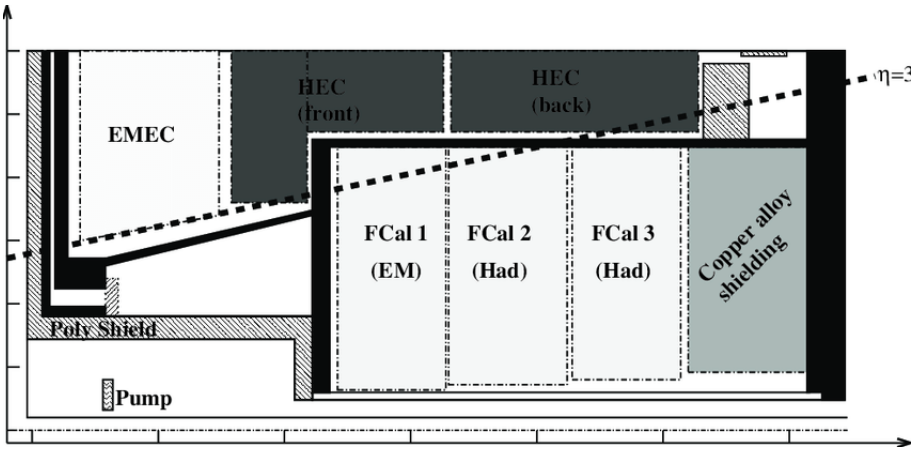

Figure 2.10: A view of the ATLAS forward calorimeter system. Figure taken from Ref. [39].

In between $1.4 < |\eta| < 1.6$, magnetic field is provided by a combination of barrel and end-cap magnets.

As illustrated in Figure 2.11, the MS uses four types of gaseous chambers: Monitored Drift Tubes (MDT) [42], Cathode Strip Chambers (CSC) [43], Resistive Plate Chambers (RPC) [44] and Thin Gap Chambers (TGC) [45]. MDTs and CSCs, referred as precision chambers, are used for providing precision measurements of track coordinates. RPCs and TGCs, referred as trigger chambers, have fast read-out times and are used for providing bunch-crossing identification.

In the barrel region, the MS contains three cylindrical layers of MDTs aligned parallel to the z-axis at radial distances 5, 7.5 and 10.5 m. MDT chambers have rectangular geometry and have multiple layers of drift tubes arranged perpendicular to the z-direction to make precision measurements along η. Each drift tube is filled with a gas mixture of 93% Ar- 10% CO_2 and has a diameter of 3 cm with a tungsten-rhenium wire operated at 3 kV running through its center. The last two layers of MDTs are surrounded by RPCs. Each RPC unit consists of two parallel resistive plates with a gap of 2 mm filled with $C_2H_2F_4$. RPCs operated at a very high potential difference of 9.8 kV to provide a timing resolution of 2 ns.

In the end-cap regions, the MS contains four wheels of MDT chambers at $z = 7.5$,

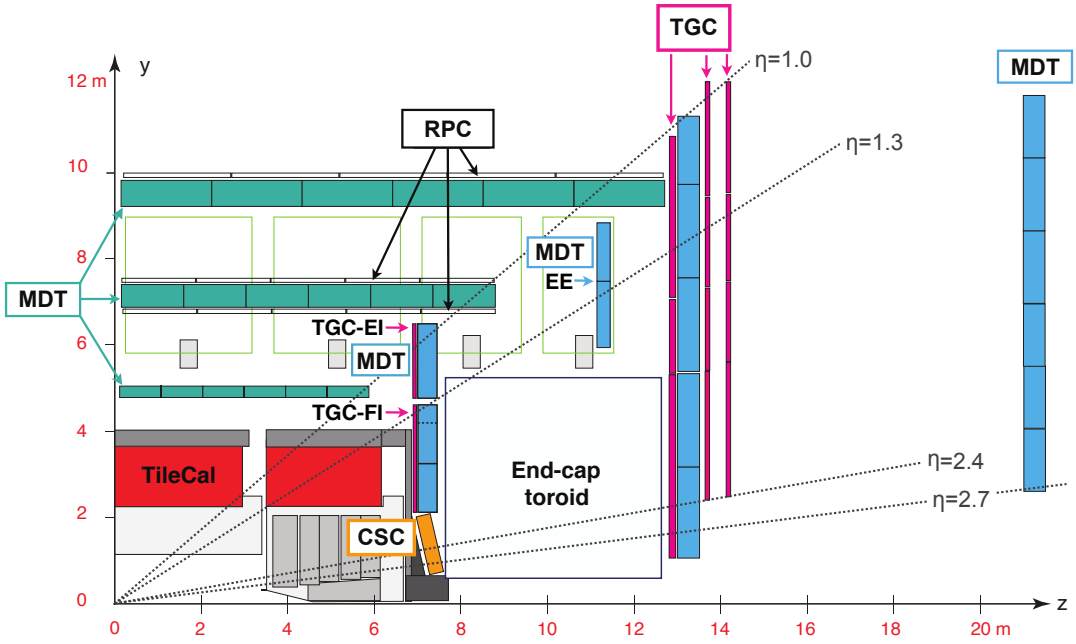

Figure 2.11: A view of the Muon Spectrometer system in the $r - z$ plane. Figure taken from Ref. [41].

10, 14 and 22 m covering the region $1 < |\eta| < 2.7$. The MDT tubes are arranged azimuthally to provide precision measurement in η. As the $2 < |\eta| < 2.7$ region in the first layer experiences a very high influx of particles, CSCs are used instead of MDTs to provide higher granularity. The CSCs are mutli-wire proportional chambers filled with $Ar/CO_2/CF_4$ mixture. The cathode in the CSC detectors is segmented into strips perpendicular to anode wires allowing spatial information measurement in both η and ϕ. The TGCs surround the third wheel of MDTs in three layers. Like CSCs, TGCs are also multi-wire proportional chambers filled with a gas mixture of CO_2 and n-pentane. They have gold plated tungsten wires as anodes separated by a distance of 1.8 mm operated at 2.9 kV. This allows TGCs to provide a timing resolution of 4 ns.

2.2.5 Trigger and Data Acquisition

During Run-2 data taking period, the LHC delivered proton beams to the ATLAS detector at a bunch crossing rate of 40 MHz. To record all events, it would require

a data-write speed of 60 TB/s, as each bunch-crossing event produces $\sim$ 1.5 MB of data. This is neither technically possible nor desirable as most of the events do not contain any interesting physics. A two level trigger system is used to reduce the rate from 40 MHz to 1 kHz [46].

The first level of the trigger system, referred to as the Level-1 (L1) trigger, is a hardware-based trigger consisting of fast electronics. It performs the first level selection within 2.5 μs based on the coarse grained information from the calorimeters and the MS. It is designed to reduce the 40 MHz rate to 100 kHz. The L1 trigger also defines Region of Interests (RoI) where it found interesting features. It delivers information about RoIs to the high level trigger if the event is accepted.

The second level of the trigger system, called the High Level Trigger (HLT), is a software-based trigger [47]. It uses a large farm of CPUs to perform refined measurements by reconstructing physics objects in RoIs. It reduces the rate from 100 kHz to 1 kHz. Events accepted by the HLT are sent to CERN's permanent storage facility.

A summary diagram of the ATLAS Trigger and Data Acquisition system is shown in Figure 2.12.

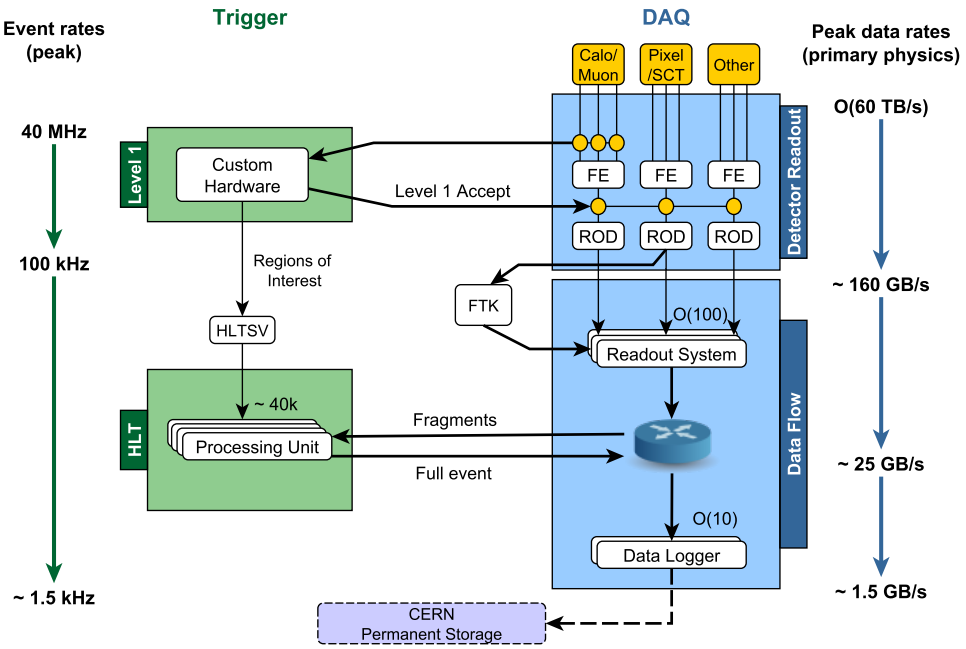

Figure 2.12: A summary of the ATLAS Trigger and Data Acquisition system used during Run2 data taking period. Figure taken from Ref. [47].

Chapter Three: Particle Reconstruction & Identification

Efficient and precise reconstruction of physics objects from raw detector signals is a necessary requirement for any physics analysis. This chapter presents an overview about methods used for the identification and isolation of physics objects like electrons, muons, photons, jets, b-jets and MET.

3.1 Charged Particle Tracks

Charged particle tracks are reconstructed using the information provided by the ID [48, 49]. Raw detector signals $-hits-$ from different layers of the ID are converted into three dimensional measurements, referred in to as *space-points*. In the Pixel detector, each hit in a layer will provide a space-point. Whereas in the SCT detector, a space-point is obtained by combining the information from both sides of a strip to get three dimensional information. The TRT detector provides only two dimensional information, along $r-\phi$ direction in the barrel region and $\phi-z$ direction in the endcaps.

Seeds for track finding algorithm are obtained from sets of three space-points. Track candidates are then built using a combinatorial Kalman filter algorithm. A dedicated ambiguity resolver algorithm is used to remove track candidates with incorrectly assigned space-points.

The track finding strategy includes two sequences: an *inside-out* track reconstruction and a *outside-in* track reconstruction. Inside-out track reconstruction is the primary pattern recognition algorithm for reconstructing the majority of the tracks. In this procedure, track candidates, built from the Pixel and SCT detector hits, are extended outwards to find compatible measurements in the TRT. The Outside-in track reconstruction procedure starts with the segments built from the hits in the TRT detector and extends inward to find compatible measurements in the Silicon de-

tector. The outside-in approach is really useful in reconstructing tracks coming from secondary vertices (e.g. K_s decays) and photon conversions, which may not have any hits in the Silicon detector.

Each track is fully characterized by five *perigee* parameters: $(d_0, z_0, \phi, \theta, q/p)$.
Here, d_0 (z_0) = The transverse (longitudinal) impact parameter,
ϕ and θ = The azimuthal and polar angles of the track respectively,
q/p = ratio of electric charge to the momentum of the track.

The perigee parameters of the track are estimated by assuming a perfect helical trajectory inside the solenoidal magnetic field.

3.2 Primary Vertices

Primary vertices are defined as the coordinates in space where pp interactions have occurred. The primary vertex reconstruction algorithm [50, 51] uses the collection of reconstructed ID tracks as the input. Two main stages are involved in this procedure: vertex finding and vertex fitting. In the vertex finding stage, seed positions for the primary vertices are obtained by associating reconstructed tracks to them. The actual primary vertex position and its error are determined in the vertex fitting stage by iteratively fitting the tracks with the vertex seed. Only vertices associated with at least two reconstructed tracks with $p_T > 400$ MeV are considered.

Due to pile-up, each event is generally associated with many primary vertices. The vertex corresponding to the hard-scatter interactions, referred in to as the *hard-scatter primary vertex*, is chosen as the primary vertex with the highest sum of squared transverse momenta of tracks originating from that vertex. All other primary vertices are considered as *pile-up vertices*. Only objects originating from the hard-scatter primary vertex are considered in the subsequent steps of the reconstruction.

3.3 Photons

Reconstruction of photon candidates begins with the formation of topo-clusters in the EM calorimeter. If there are one or two ID tracks matching to the electromagnetic cluster, it is reconstructed as converted photon else as unconverted photon. Based on the number of tracks matching to the cluster and hits in the Silicon detector, photon is categorized into 6 different conversion types. These are listed in Table 3.1. Candidates in the calorimeter transition region $1.37 < |\eta| < 1.52$ are excluded. An *identification* criteria [52], based on a set of rectangular cuts on the EM shower shape variables, is applied to separate photons produced in the hard-scatter process (prompt-photons) from fake photons, i.e., photons due to radiation from hadrons, mis-identified electrons, etc,. Further more, all photon candidates are required to be *isolated*, i.e., the amount of energy around the photon must be below a threshold. The methods used for calibrating the photon energy measurements are described in Ref. [53].

Conversion Type	# tracks matched to cluster
Unconverted = 0	Zero
SingleSi = 1	One track only, with Si hits
SingleTRT = 2	One track only, no Si hits (TRT only)
DoubleSi = 3	Two tracks, both with Si hits
DoubleTRT = 4	Two tracks, none with Si hits (TRT only)
DoubleSiTRT = 5	Two tracks, only one with Si hits

Table 3.1: Based on the number of ID tracks matching to the EM cluster, photons are classified into six different conversion types.

3.4 Electron Reconstruction

Electron candidates are reconstructed from electromagnetic clusters matched with the reconstructed charged particle tracks in the inner detector. Prompt electrons, i.e., electrons produced in the hard-scatter process, are identified using a likelihood discriminant [54] constructed from quantities measured in the inner detector and the calorimeter. Electron candidates in the calorimeter transition region $1.37 < |\eta| < 1.52$

are excluded. They are required to pass further selections on the transverse and longitudinal impact parameters: $|z_0 \sin\theta| < 0.5$ mm and $|d_0/\sigma(d_0)| < 5$. Electrons are calibrated with the method described in Ref. [53].

3.5 Jet Reconstruction

Jet candidates are reconstructed from 3-dimensional topological clusters [55] in the calorimeter using the anti-k_t algorithm [56] with a radius parameter of R=0.4. Each topological cluster is calibrated to electromagnetic scale response prior to jet reconstruction. The reconstructed jets are then calibrated to the particle level by the application of a jet energy scale derived from simulation and *in situ* corrections based on $\sqrt{s}$=13 TeV data [57]. After energy calibration, jets are required to have $p_T > 25$ GeV and $|\eta| < 4.5$. Quality criteria are imposed to identify jets arising from non-collision sources or detector noise and any event containing at least one such jet is removed. To reduce the contamination due to jets originating from pile-up interactions, jets with $p_T < 60$ GeV and $|\eta| < 2.4$ are required to pass a selection based on the *Jet Vertex Tagger (JVT)* tool [58].

3.6 b-jets

Jets containing b-hadrons are identified (b-tagged) using the DL1r algorithm [59, 60]. This algorithm is basically a neural network trained with information from the impact parameters of displaced tracks as well as topological properties of secondary and tertiary decay vertices reconstructed within the jet. The working point used in this analysis corresponds to an average efficiency of 70% for b-jets with $p_T > 20$ GeV and $|\eta| < 2.5$ in $t\bar{t}$ events. The expected rejection factors against light and c-jets are 280 and 13, respectively [61].

3.7 Muon Reconstruction

Muons are reconstructed and identified primarily using information provided by the ID and the MS, supplemented with information from the calorimeter energy deposits. The first step in the muon reconstruction is the independent reconstruction of tracks in the ID and the MS. The independently reconstructed tracks are then combined to form a complete track representing the traversal of the muon through the full detector.

In the ID, muon tracks are reconstructed like any other charged particles as described in Section 3.1. In the MS, muon tracks are built by constructing track segments from hit patterns in different muon sub-systems. Muon track candidates are then obtained by fitting together hits from all track segments. To build a muon track candidate, at least two matching segments are required, except in the transition region between the barrel and endcap where a single track segment can be used. Once a muon track candidate is formed, a global χ^2 fit is between the track candidate and associated hits. If the χ^2 of the fit is small enough, then the track candidate is accepted as a MS track.

The muon tracks from the ID and MS are combined using several algorithms using the information provided by the ID, MS and calorimeters. Based on the subdetectors used in the reconstruction, four types of muons are defined:

- **Combined (CB) Muon:** This type of muon is formed when a track in the ID is found to be consistent with the trajectory of the MS track. A combined muon track is formed with a global refit of hits from the tracks in the ID and MS. During the global refit, hits from the MS may be added or removed to improve the fit quality. Most of the muons are reconstructed using an outside-in pattern recognition algorithm, in which a muon is first reconstructed in the MS and then extrapolated inwards to find a matching ID track. An inside-out algorithm, in which an ID track is extrapolated outwards to find a matching MS track, is used as a complementary approach.

- **Segment-tagged (ST) Muon:** A segment-tagged muon is formed when an ID track, once extrapolated to the MS, is associated with at least one local

track segment in the MDT or CSC chambers. ST muons are used when a muon crosses only one layer of the MDT chambers, either because of its low p_T or because it falls into regions with reduced MS coverage.

- **Calorimeter-tagged (CT) Muon:** This type of muon is formed when an ID track is matched to an energy deposit in the calorimeter that is consistent with a minimum ionizing particle. As the CT muons have lowest purity, they are used only in the $|\eta| < 0.1$ region where the MS is only partially instrumented to allow for cabling and services to the calorimeters and the ID.

- **Extrapolated (ME) Muon:** Exatrapolated muon is formed based only on the MS track and a loose requirement on the track be compatible with originating from the primary vertex. ME muons are mainly used in the region $2.5 < |\eta| < 2.7$, which is not covered by the ID.

Overlaps between different types of muons sharing the same ID track are resolved by giving preference to CB muons, then to ST muons, and finally to CT muons. The methods used for the reconstruction, identification, calibrations of muons are detailed in Ref. [62].

3.8 Missing Transverse Momentum

The colliding proton beams in each pp interaction are assumed to colliding *head-on*, with momentum only along the z-axis. Thus, conservation of momentum in the $x-y$ plane implies that the vector sum of transverse momenta of all objects originating from the hard-scatter primary vertex should be exactly zero. The missing transverse momenta E_T^{miss} in an event represents the imbalance in the sum of visible transverse momenta. Nonzero values of E_T^{miss} may indicate the presence of weakly interacting particles that do not leave any signatures in the detector. Within the SM, these particles are neutrinos. In theories beyond the SM, there are many prospects for such particles. Consequently, E_T^{miss} is an important variable in various searches for physics

beyond the SM.

The components of missing transverse momentum along $x-$ and $y-$ directions are calculated [63] using,

$$E_{x(y)}^{\text{miss}} = E_{x(y)}^{\text{miss},e} + E_{x(y)}^{\text{miss},\gamma} + E_{x(y)}^{\text{miss},\tau} + E_{x(y)}^{\text{miss},\mu} + E_{x(y)}^{\text{miss, jets}} + E_{x(y)}^{\text{miss, soft}}. \tag{3.1}$$

The terms for charged leptons, photons, jets represent the negative sum of the momenta of all objects of the respective type in the event. The *soft term* $E_{x(y)}^{\text{miss, soft}}$, represents the negative sum of the momenta of all reconstructed tracks originating from the hard-scatter primary vertex and not associated with any reconstructed hard object.

The magnitude (E_T^{miss}) and the azimuthal angle (ϕ^{miss}) are then given by,

$$E_T^{\text{miss}} = \sqrt{(E_x^{\text{miss}})^2 + (E_y^{\text{miss}})^2} \tag{3.2}$$

$$\phi^{\text{miss}} = \arctan\left(E_y^{\text{miss}}/E_x^{\text{miss}}\right) \tag{3.3}$$

The measurement of E_T^{miss} is affected by the detector mismodelling, limited acceptance of the detector and the miscalibration of the reconstructed objects. It is also susceptible to pile-up effects. Generally, high pile-up degrades the resolution of the E_T^{miss}.

3.9 Overlap Removal between Reconstructed Objects

To avoid, double counting of objects and to remove leptons likely originating from hadron decays, following overlap removal procedure is applied.

Firstly, electron candidates sharing a track with muon candidates are removed to suppress contributions from muon bremsstrahlung.

Next, overlaps between electrons and jet candidates are resolved. Any jet candidate whose axis is within $\Delta R < 0.2$ of electron candidate is discarded. This is to

remove jets are formed primarily from the showering of prompt electrons. After this removal, any electron that is within $\Delta R < 0.4$ of the axis of any jet is removed. This selection is applied to remove electrons that are produced in the decay chain of hadrons.

After that, muon candidates within $\Delta R < 0.4$ of the axis of any jet are removed. This selection is designed to remove those muons that are likely to have produced in the decay chain of hadrons.

Photons within $\Delta R < 0.4$ cone of electrons and muons are removed. Finally, jets within $\Delta R < 0.4$ cone of photons are removed.

Object overlap removal procedure applied in this analysis is summarized in Table 3.2.

Keep	**Remove**	**Cone size (ΔR)**
Muon	Electron	0.01
Electron	Jet	0.2
Jet	Electron	0.4
Jet	Muon	0.4
Electron	Photon	0.4
Muon	Photon	0.4
Photon	Jet	0.4

Table 3.2: Summary of the overlap removal procedure between electrons, muons, photons and jets

Part I

Seeing a single top quark: Search for the associated production of a single top quark and a photon

Chapter Four: Associated production of a single top quark and a photon

Electroweak production of a single top quark in association with a photon, $pp \to tq\gamma$, is one of the rare processes predicted by the SM. Observation and precise measurement of the cross-section of this process provides an important test for the SM.

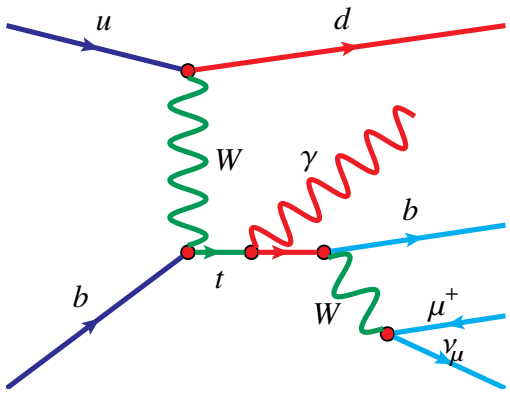

Figure 4.1: Leading-order Feynman diagram for $tq\gamma$ production in 5-flavor scheme

The cross-section of $tq\gamma$ process ($\sigma_{tq\gamma}$) is sensitive to the top quark coupling to photons, a key parameter in the SM which quantifies the strength of the interaction between the top quark and the photon. Measurement of $\sigma_{tq\gamma}$ can also identify or disambiguate anomalous electric and magnetic dipole moments of the top quark [64][65].

The most general Lorentz-invariant expression for $t\gamma$-vertex can be represented in the form,

$$\Gamma_\mu(q^2) = -ie\{\gamma_\mu[F_{1V}(q^2) + F_{1A}(q^2)\gamma_5] + \frac{\sigma_{\mu\nu}}{2m_t}q^\nu[iF_{2V}(q^2) + F_2A(q^2)\gamma_5]\}, \qquad (4.1)$$

where q is the four-momentum of the photon, e is the proton charge, m_t is the top quark mass, and $\sigma_{\mu\nu} = (i/2)[\gamma_\mu, \gamma_\nu]$. The terms F_{iV} and F_{iA} represent the form factors for vector and axial-vector couplings, respectively. In the low energy limit $q^2 \to 0$,

the form factors are related to the physics quantities via,

$$F_{1V}(0) = Q_t; \quad F_{2V}(0) = a_t Q_t; \quad F_{2A} = \frac{2m_t d_t}{e}, \tag{4.2}$$

where Q_t is the electric charge of the top quark, a_t and d_t are the anomalous magnetic and electric dipole moments of the top quark, respectively. In the SM, at tree level, all form factors except F_{1V} are equal to zero. When higher-order loop corrections are considered, F_{2V} and F_{2A} receive non-zero contributions. The corresponding prediction for the anomalous magnetic dipole moment is $a_t \sim 0.02$ while the anomalous electric dipole moment is $d_t \ < 10^{-30}$ e cm. Any observation of deviations from these predictions, for example enhanced dipole moments, would indicate the physics beyond the SM. The expected bounds on the top quark anomalous dipole moments with pp collision data from the LHC at $\sqrt{s} = 14$ TeV are shown in Figure 4.2.

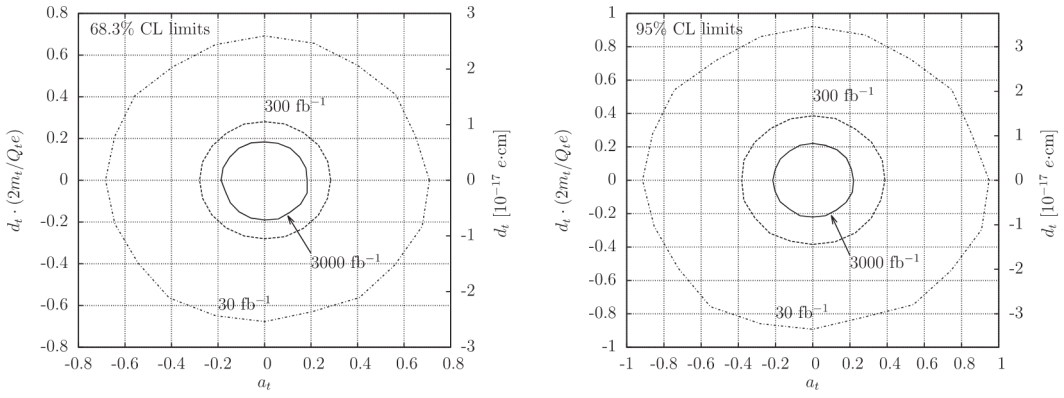

Figure 4.2: Expected 68% CL (left) and 95% CL (right) limits on the top quark anomalous dipole moments with LHC pp collision data at $\sqrt{s} = 14$ TeV. Figure taken from Ref. [64]

This process has not been observed by any experiment yet. However, the CMS collaboration published an evidence for this process with partial Run-2 dataset, corresponding to an integrated luminosity of 35.9 fb^{-1} [66]. Only events with a single muon in the final state are considered in this analysis. The measured value of fiducial cross-section time branching fraction is $\sigma(pp \to tq\gamma) \times \mathcal{B}(t \to \mu\nu b) = 115 \pm 17$ (stat) $\pm$ 30 (syst) fb. This result is in agreement with the expected SM value: 81 $\pm$ 4

fb. The median expected significance is 3.0 standard deviations, while the observed events correspond to a significance of 4.4 standard deviations above the background-only hypothesis.

This dissertation reports the first-ever ATLAS search for $pp \to tq\gamma$ process. The goal of this analysis is the observation and the measurement of fiducial cross-section of the $tq\gamma$ process. It uses the full run-2 dataset collected by the ATLAS experiment during the 2015-18 period, which corresponds to an integrated luminosity of 139 fb^{-1}. After establishing the $tq\gamma$ production process, a subsequent analysis will be performed which will feature differential cross-section measurements to set constraints on the anomalous top quark dipole moments with the Effective Field Theory (EFT) approach.

The organization of this analysis is as follows: Chapter 5 describes the data and Monte Carlo (MC) samples. Chapter 6 describes the event pre-selection. Estimation methods for $e \to \gamma$ and $j \to \gamma$ fake photon backgrounds are detailed in Chapter 7. Data/MC comparison plots for signal region, $t\bar{t}\gamma$ CR and $W\gamma$ CR are shown in Chapter 9. Neural network training and optimization studies are detailed in Chapter 10. Theoretical and experimental systematic uncertainties are described in Chapter 11. Chapter 12 describes the results from signal region fit to Asimov data and background only fit to data. Finally, conclusions are summarized in Chapter 13.

Chapter Five: Data and Monte Carlo samples

Dataset and Monte Carlo samples used in the SM $tq\gamma$ analysis are described in this chapter.

5.1 Dataset

This analysis uses pp collision data collected by the ATLAS experiment during 2015-18 at $\sqrt{s} = 13$ TeV. The luminosity corresponding to this data is determined using multiple redundant luminosity sensitive detectors [67] in the forward region. The absolute calibration of the luminosity scale of each detector is performed using dedicated beam-separation scans in X-Y plane with a method known as van der Meer (vdM) method [68].

Figure 5.1 shows time versus the cumulative luminosity delivered by the LHC (green), recorded by the ATLAS experiment (yellow), and marked to be good quality data by applying standard data-quality selections (blue). Luminosity recorded by the ATLAS experiment is lower than the luminosity delivered by the LHC due to trigger dead-time and the warm-start procedure of the ATLAS Inner Detector. Total integrated luminosity corresponding to the good quality data collected during Run-2 is 139 $\text{fb}^{-1} \pm 1.7\%$. Summary of integrated luminosity and it's uncertainty for each year are presented in Table 5.1.

Year	Luminosity (fb^{-1})	Uncertainity (fb^{-1})
2015+2016	36.2	0.8
2017	44.3	1.0
2018	58.5	1.2
Total	139.0	2.4

Table 5.1: The integrated luminosity and it's uncertainty for each year's data after applying standard data-quality selections

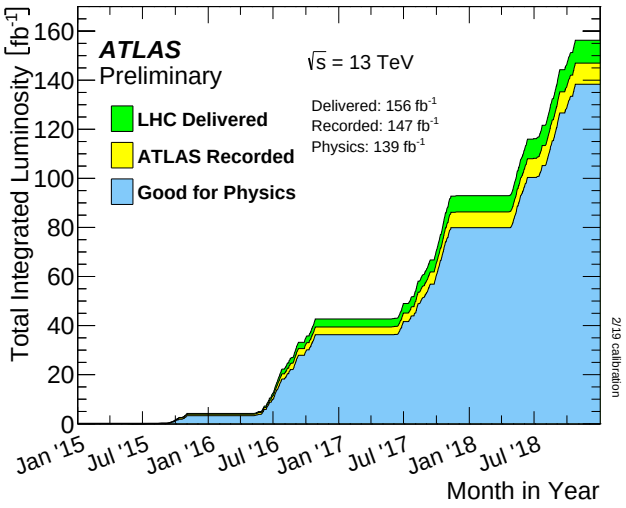

Figure 5.1: Time versus the cumulative luminosity delivered by the LHC (green), recorded by the ATLAS experiment (yellow), and marked to be good quality data by applying standard data-quality selections (blue). Luminosity recorded by the ATLAS experiment is lower than the luminosity delivered by the LHC due to trigger dead-time and the warm-start procedure of the ATLAS Inner Detector.

5.2 Monte Carlo samples

5.2.1 Signal Modelling

The SM $tq\gamma$ process is simulated [69] at next-to-leading order (NLO) in four flavor scheme and at the t-channel of single top production using MadGraph5_aMC@NLO v2.6.2 event generator [70] interfaced to the Pythia8 [71] parton showering. The top quark is decayed using MadSpin. Only final states with at least one lepton are generated. The decays of bottom and charm hadrons are simulated using EvtGen v1.2.0 [72]. The photon transverse momentum (p_T) is required to be at least 10 GeV. The photon and the lepton are required to have $|\eta| < 5.0$. The angular separation between photon and other final state particles is required be $\Delta R > 0.2$. Where, $\Delta R = \sqrt{\Delta\eta^2 + \Delta\phi^2}$ and ϕ is the azimuthal angle in radians. The renormalization and factorisation scales are set to $H_T/2$, where

$$H_T = \sum_i \sqrt{m_i^2 + p_{T,i}^2} \tag{5.1}$$

Where, i runs over all outgoing particles from the matrix element calculation. The cross-section obtained from the generator is $1.14^{+6.3\,\%+1.0\,\%}_{-6.0\,\%-1.0\,\%}$ pb, where the uncertainties are due to renormalization & factorization scales and PDF variations, respectively.

5.2.2 Background Modelling

The $t\bar{t}\gamma$ process is modelled at leading order in QCD using MadGraph5_aMC@NLO v2.3.3 event generator interfaced to Pythia 8.212 parton showering algorithm tuned with the A14 parameter set [73]. Events in which the photons originate from the top quark decay products are also included in this sample. The matrix-element calculation uses the NNPDF2.3LO PDF set [74, 75]. An inclusive k-factor of 1.16, derived from NLO QCD calculations [76], is applied to the generator cross-section.

Simulated events of $W\gamma$ + jets and $Z\gamma$+jets are produced at NLO using Sherpa 2.2.2 and Sherpa 2.2.4 generators [77, 78] respectively.

MC samples for $t\bar{t}$ process, t-, s- and tW-channels of single-top quark production processes are generated at NLO in QCD using Powheg-Box [79–81] interfaced to Pythia 8.230 parton showering program. Inclusive k-factors are used for each sample to extrapolate to NNLO in QCD [82–85]. Furthermore, spin correlations are preserved for the top quarks. The decays of hadrons containing b or c quarks is modeled with the EvtGen 1.6.0 package.

Events with W and Z bosons in association with additional jets are simulated with Sherpa 2.2.1 at next-to-leading order in QCD. The samples are normalised to the next-to-next-to-leading-order cross-section in QCD [86].

5.2.3 Detector response & Pileup simulation

All Monte Carlo samples are processed through a simulation of the ATLAS detector response based on the Geant4 tool [87]. In-time and out-of-time pileup simulations are overlaid on all hard-scatter events before digitization. They modelled using minimum-bias events generated using Pythia8. The number of pileup events overlaid

for each hard-scattering interaction is a random number sampled from the Poission distribution with a mean $< \mu >$, where $< \mu >$ is the average number of interactions per bunch crossing. Simulated events are reweighted to ensure that the pileup distribution in simulation matches that observed in data.

Chapter Six: Event selection

6.1 Event categorization

As this analysis targets a signal topology that contains a well-reconstructed photon, other objects that are mis-identified as photons represent a major background source in this analysis. The most dominant contributions of this type of background arise from electrons that are mis-identified as photons and jets that are mis-identified as photons, which are referred to as $e \to \gamma$ fakes and $j \to \gamma$ fakes, respectively, in the following. In order to estimate these two different fake contributions, events are classified in MC into three different categories, prompt, $e \to \gamma$ fake and $j \to \gamma$ fake. This classification relies on information of the truth particle that is associated with the leading photon, where the association is performed by the *Truth to cluster* matching algorithm by the *MCTruthClassifier* package. Events are classified by the following scheme:

- $\mathbf{e} \to \gamma$ fake:
  - the truth particle is an electron
  - the truth particle is a photon and there is a truth electron within a distance of $\Delta R = 0.05$
- $\mathbf{j} \to \gamma$ fake: the truth particle is a hadron or the photon originates from a truth particle classified as hadron

Events, where the leading photon does not fulfill any of the aforementioned criteria, is referred to as prompt.

6.2 Pre-selection region

Signal events are characterized by exactly one lepton, at least a photon, one b-tagged jet in the final state. A pre-selection region enriched with signal events is defined by applying following selection requirements:

- At least one γ with $p_T > 20$ GeV
- Exactly one lepton with $p_T > 27$ GeV
- $E_T^{\text{miss}} > 30$ GeV
- Exactly 1 b-tagged jet passing 70 % working point (WP) of the DL1r algorithm

Table 6.1 shows the yields in this pre-selection region for converted and for unconverted photons.

Table 6.1: Yields of the different background contributions in the pre-selection region. Only statistical uncertainties are given here.

process	converted photons	unconverted photons	combined
VV	149.0 ± 3.0	103.0 ± 3.0	252.0 ± 4.0
$Z\gamma$+jets	1312.0 ± 23.0	2867.0 ± 33.0	4179.0 ± 40.0
$W\gamma$+jets	3733.0 ± 67.0	8919.0 ± 106.0	12652.0 ± 125.0
$t\bar{t}\gamma$	9074.0 ± 19.0	21810.0 ± 30.0	30883.0 ± 35.0
$t\bar{t}$	16564.0 ± 52.0	9897.0 ± 40.0	26461.0 ± 66.0
W+jets	648.0 ± 115.0	874.0 ± 202.0	1522.0 ± 233.0
Z+jets	5438.0 ± 136.0	2784.0 ± 102.0	8222.0 ± 170.0
tq	675.0 ± 6.0	1435.0 ± 9.0	2110.0 ± 11.0
tW+tb	2496.0 ± 19.0	3021.0 ± 20.0	5517.0 ± 28.0
lepton fake	1388.0 ± 41.0	2641.0 ± 58.0	4029.0 ± 71.0
$tq\gamma$	1382.0 ± 26.0	2947.0 ± 37.0	4329.0 ± 45.0
$e \to \gamma$	20972.0 ± 144.0	9561.0 ± 103.0	30532.0 ± 177.0
$j \to \gamma$	2977.0 ± 88.0	3788.0 ± 143.0	6765.0 ± 168.0
prompt	18911.0 ± 119.0	43947.0 ± 200.0	62858.0 ± 233.0
total SM	42859.0 ± 206.0	57296.0 ± 267.0	100155.0 ± 338.0
data	42450.0 ± 206.0	59268.0 ± 243.0	101718.0 ± 319.0

Figure 6.1 shows the composition of the pre-selection region with respect to the photon origin and to the different processes. Events containing prompt photons provide $\approx$ 63% of the total expected yield, where $\approx$ 30 % and $\approx$ 8 % of all events contain a $e \to \gamma$ fake and $j \to \gamma$ fake, respectively. Therefore, the estimation of the $e \to \gamma$ fake contribution is a crucial step in this analysis. Although $j \to \gamma$ fakes are the smaller fake contribution, a sophisticated estimation is mandatory as normalization and shape of kinematic distributions may not be well-modeled in MC.

Moreover, the dominant background processes are $t\bar{t}\gamma$, $t\bar{t}$, $W\gamma$+jets and Z+jets. Figure 6.2 shows the composition of the pre-selection region with respect to the different processes for the different photon types. The prompt photon contribution is mainly arising from $t\bar{t}\gamma$ and $W\gamma$+jets events. The semi-leptonic channel of $t\bar{t}$ provides more than 75 % of the $j \to \gamma$ fakes. The $e \to \gamma$ fake contribution is dominated by $t\bar{t}$ where an electron and another lepton is produced by the leptonic decays of the top quarks and Z+jets with $Z \to ee$.

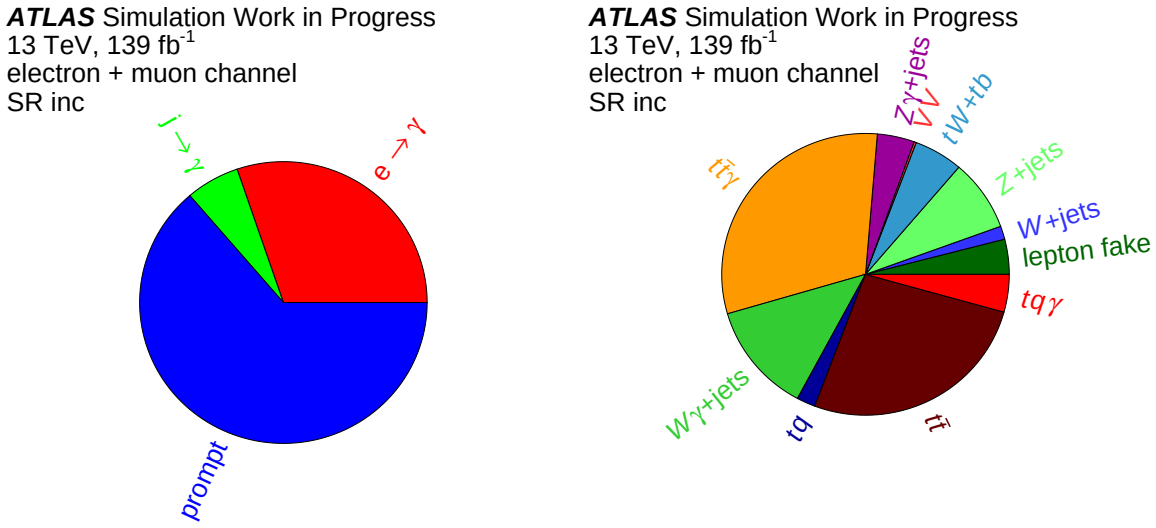

Figure 6.1: Composition of the pre-selection region with respect to the photon origin (left) and to the different processes (right).

Figure 6.3 shows the composition with respect to the photon category for converted and unconverted photons. Almost 50% of all events arise from $e \to \gamma$ fakes for converted photons. In the case of unconverted photons the contribution of $e \to \gamma$ fakes is significantly smaller. As the composition for converted and unconverted photons is fairly different, the separate estimation of the fake contributions for converted photons and unconverted photons represents a key element to this analysis.

6.2.1 Reducing Z+jets background

The large contribution from $Z \to ee(\to \gamma)$ is reduced by vetoing events that fulfill 80 GeV $< m_{e\gamma} <$ 100 GeV, where $m_{e\gamma}$ represents the invariant mass of the leading

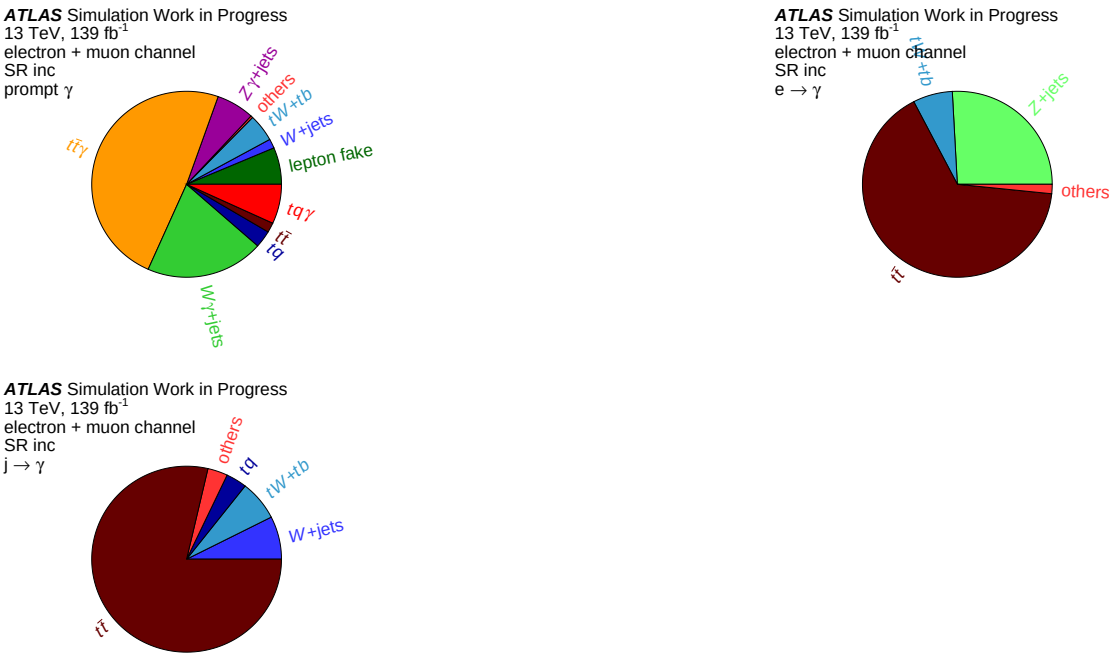

Figure 6.2: Composition of the pre-selection region with respect to the different processes for prompt photons (left), $e \to \gamma$ (middle) and $j \to \gamma$ (right).

photon and an electron candidate. The distributions of $m_{l\gamma}$ before and after applying theis Z mass window cut are depicted in Figure 6.4.

The yields of the different processes after applying this criterion are shown in Table 6.2. The contributions from Z+jets and consequently from $e \to \gamma$ are significantly reduced.

6.2.2 Choosing the DL1r working point

In order to provide the highest sensitivity to the $tq\gamma$ signal process, it is checked whether choosing a different DL1r working point enhances the $\frac{S}{\sqrt{B}}$ ratio. The results of this checked are listed in Table 6.3, where it can be seen that the largest sensitivity is provided by the 70% working point.

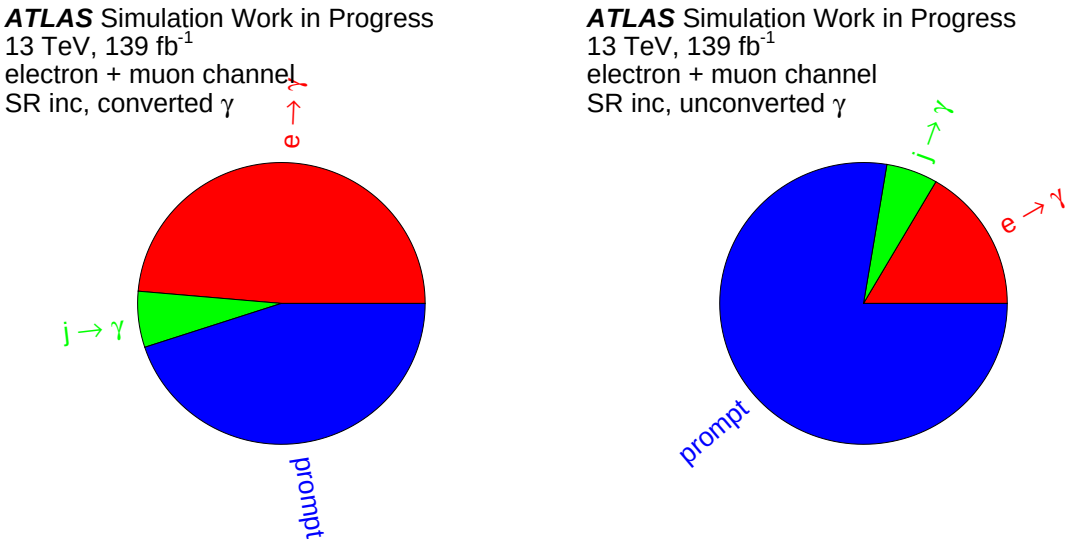

Figure 6.3: Composition of the pre-selection region with respect to the photon origin for converted photons (left) and unconverted photons (right).

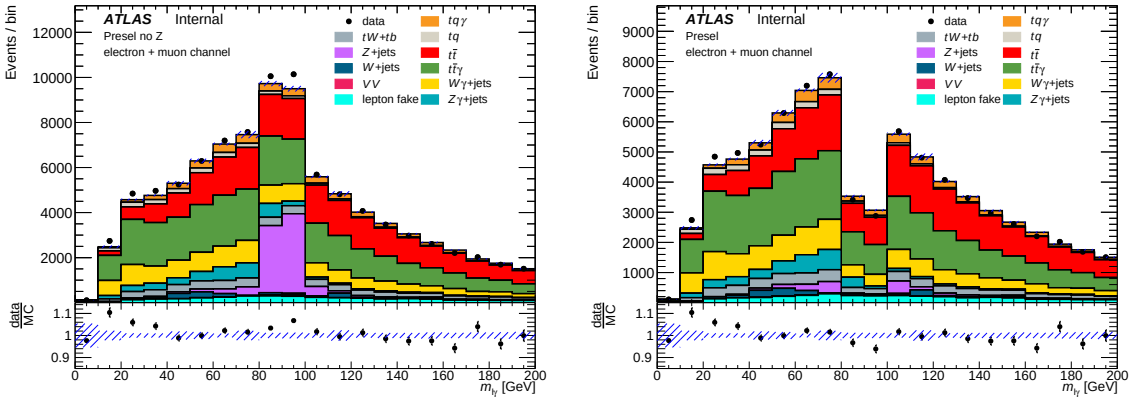

Figure 6.4: Distribution of the invariant mass of the lepton and the leading photon $m_{l\gamma}$ before (left) and after (right) applying the Z mass window cut.

6.2.3 Final definition of the pre-selection region

The final definition of the pre-selection region is given in Table 6.4.

Table 6.2: Yields of the different background contributions in the pre-selection region after applying the Z mass window cut. Only statistical uncertainties are given here.

process	converted photons	unconverted photons	combined
VV	84.0 ± 3.0	70.0 ± 3.0	154.0 ± 4.0
$Z\gamma$+jets	1192.0 ± 22.0	2600.0 ± 31.0	3791.0 ± 38.0
$W\gamma$+jets	3490.0 ± 65.0	8369.0 ± 102.0	11859.0 ± 121.0
$t\bar{t}\gamma$	8480.0 ± 19.0	20332.0 ± 29.0	28811.0 ± 34.0
$t\bar{t}$	15487.0 ± 50.0	9175.0 ± 39.0	24662.0 ± 63.0
W+jets	630.0 ± 115.0	821.0 ± 202.0	1452.0 ± 232.0
Z+jets	1182.0 ± 61.0	566.0 ± 43.0	1748.0 ± 74.0
tq	630.0 ± 6.0	1341.0 ± 9.0	1971.0 ± 11.0
tW+tb	2352.0 ± 18.0	2803.0 ± 19.0	5155.0 ± 27.0
lepton fake	1327.0 ± 41.0	2580.0 ± 58.0	3907.0 ± 71.0
$tq\gamma$	1285.0 ± 25.0	2733.0 ± 35.0	4018.0 ± 43.0
$e \to \gamma$	15697.0 ± 75.0	6852.0 ± 45.0	22549.0 ± 88.0
$j \to \gamma$	2748.0 ± 88.0	3468.0 ± 143.0	6217.0 ± 168.0
prompt	17694.0 ± 117.0	41069.0 ± 197.0	58763.0 ± 229.0
total SM	36139.0 ± 165.0	51390.0 ± 248.0	87529.0 ± 297.0
data	34986.0 ± 187.0	52834.0 ± 230.0	87820.0 ± 296.0

Table 6.3: Signal and background yields for the different DL1r working points and the resulting values of $\frac{S}{\sqrt{B}}$.

	60% WP	70% WP	77% WP	85% WP
signal	3715 ± 41	4018 ± 43	4175 ± 44	4238 ± 44
background	74876 ± 224	83511 ± 294	94463 ± 386	120275 ± 612
$\frac{S}{\sqrt{B}}$	13.58	13.90	13.58	12.22

Table 6.4: Definition of the pre-selection region.

Object/Variable	Requirement
Photons	≥ 1 w/ $p_T > 20$ GeV
Leptons	$= 1$ w/ $p_T > 27$ GeV
Jets	¿1 w/ $p_T > 25$ GeV
being b-tagged	$= 1$ DL1r 70%
E_T^{miss}	> 30 GeV
$m_{e\gamma}$	$\notin$ [80, 100] GeV

Chapter Seven: Estimation of fake photon backgrounds due to mis-reconstructed electrons

In the ATLAS experiment, electrons and photons are reconstructed using very similar algorithms. Thus, electrons can be mis-reconstructed as photons due to either tracking inefficiency or failure to find a match between the Inner Detector track and the electromagnetic cluster. These mis-reconstructed electrons are referred to in the following as $e \to \gamma$ fakes.

Events with $e \to \gamma$ fakes are one of the leading background in the $tq\gamma$ analysis. However, simulation does not model these fakes well. Thus, scale factors are derived from data, in bins of η_γ and photon conversion type, to correct the simulation for this mis-modelling.

7.1 Definition of electron-to-photon fake rate scale factor

The electron-to-photon fake rate ($F_{e\to\gamma}$) is defined as the ratio of probability that an electron is mis-reconstructed as a photon to the probability that an electron is correctly reconstructed. This can be estimated from Z+jets events that are reconstructed as e^+e^- and $e\gamma$ pairs:

$$F_{e\to\gamma} = \frac{N(Z \to e\gamma)}{2 \times N(Z \to e^+e^-)} \tag{7.1}$$

A factor of 2 is included in the denominator as either of the two electrons can be mis-reconstructed as photon.

Electron-to-photon fake rates are calculated both in MC ($F^{\mathrm{MC}}_{e\to\gamma}$) and data ($F^{\mathrm{Data}}_{e\to\gamma}$) in bins of η_γ and photon conversion type. Scale factor to be applied to MC in each bin for the mis-modelling of electron-to-photon fakes is given by:

$$\text{Scale factor (SF)} = \frac{F^{\text{Data}}_{e\to\gamma}}{F^{\text{MC}}_{e\to\gamma}} \tag{7.2}$$

Substituting equation (7.1) in equation (7.3),

$$\text{SF} = \frac{N^{\text{Data}}(Z \to e\gamma) \;/\; N^{\text{MC}}(Z \to e\gamma)}{N^{\text{Data}}(Z \to e^+e^-) \;/\; N^{\text{MC}}(Z \to e^+e^-)} = \frac{\mu_{Ze\gamma}}{\mu_{Zee}} \tag{7.3}$$

Where, $\mu_{Ze\gamma} = \dfrac{N^{\text{Data}}(Z \to e\gamma)}{N^{\text{MC}}(Z \to e\gamma)}$ and $\mu_{Zee} = \dfrac{N^{\text{Data}}(Z \to e^+e^-)}{N^{\text{MC}}(Z \to e^+e^-)}$

7.2 Control & Validation regions

Two control regions (CR) and one validation region (VR) enriched with Z+jets events are defined to measure and validate $e \to \gamma$ fake rate scale factors

- $Z \to e^+e^-$ CR: Events with exactly two reconstructed electrons with opposite electric charge (OS).
- $Z \to e\gamma$ CR: Events with exactly one reconstructed electron, exactly one reconstructed photon and zero b-tagged jets.
- $Z \to e\gamma$ VR: Events with exactly one reconstructed electron, exactly one reconstructed photon and at least one b-tagged jet.

The reconstructed photon in the $Z \to e\gamma$ CR/VR events is assumed to be an misreconstructed electron. Region selection cuts are provided in Table 7.1. All three regions are orthogonal to SR as the requirement on the missing p_T is inverted.

Object	$Z \to e^+e^-$ CR	$Z \to e\gamma$ CR	$Z \to e\gamma$ VR
Photons	=0 w/ $p_T > 20$ GeV	=1 w/ $p_T > 20$ GeV	=1 w/ $p_T > 20$ GeV
Electrons	=2 (OS) w/ $p_T > 27$ GeV	=1 w/ $p_T > 27$ GeV	=1 w/ $p_T > 27$ GeV
b-jets	-	=0 w/ $p_T > 25$ GeV	$\geq$1 w/ $p_T > 25$ GeV
Missing p_T	< 30 GeV	< 30 GeV	< 30 GeV
$M(e^+e^-)$	[70, 110] GeV	-	-
$M(e\gamma)$	-	[70, 110] GeV	[70, 110] GeV

Table 7.1: Definitions of control and validation regions used for electron-to-photon fake estimation.

7.3 Overview of scale factor calculation

7.3.1 Measurement of μ_{Zee}

The normalization factor μ_{Zee} is measured by fitting templates of $M(e^+e^-)$ distribution, obtained from MC, to data in $Z \to e^+e^-$ CR. Normalization factor for the template of $Z \to e^+e^-$ process, $N^{\text{Data}}(Z \to e^+e^-)$, is determined from the profile-likelihood fit to data. Normalization factors for all other processes are fixed to their MC expected values during the fit. Pre-fit and Post-fit distributions of $M(e^+e^-)$ are shown in Figure 7.1.

Observed value of $\mu_{Zee} \;=\; 1.03 \pm 0.00026$

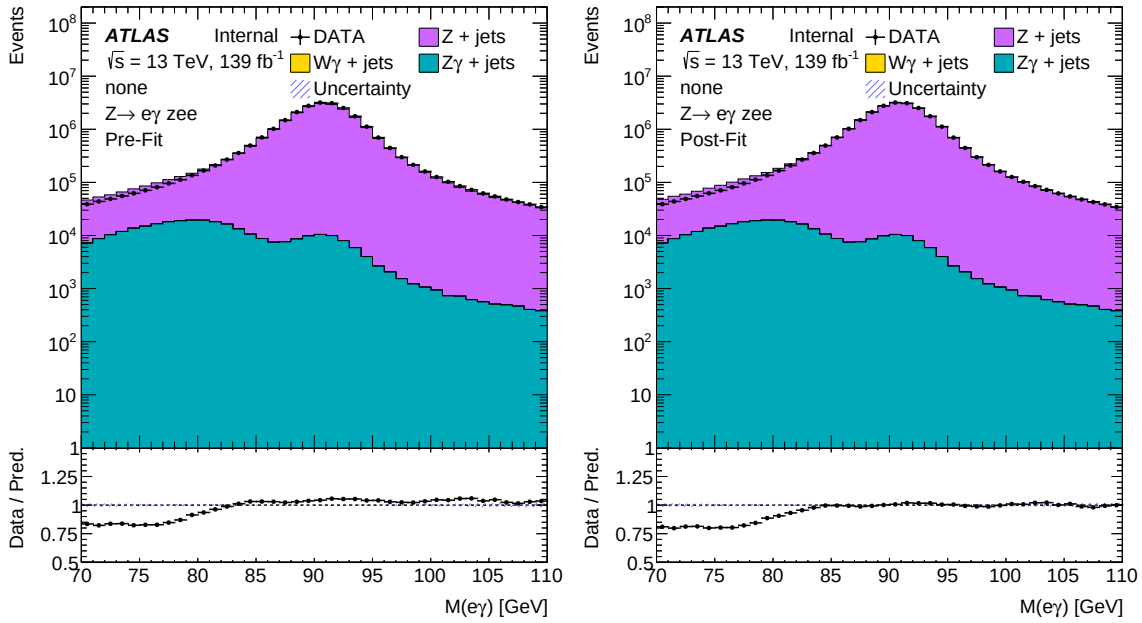

Figure 7.1: Pre-fit (left) and Post-fit (right) distributions of $M(e^+e^-)$ [GeV] for $Z \to e^+e^-$ CR

7.3.2 Measurement of $\mu_{Ze\gamma}$

The normalization factor $\mu_{Ze\gamma}$ is measured by fitting templates of $M(e\gamma)$ distribution to data in the $Z \to e\gamma$ CR.

- Template shape of $M(e\gamma)$ distribution for $Z \to e\gamma$ process is obtained from MC. It's normalization factor, $N^{\text{Data}}(Z \to e\gamma)$, is determined from the profile-likelihood fit to data.

- For other major processes in the region, i.e., $W\gamma$ and $Z\gamma$, both normalization and shape of $M(e\gamma)$ distribution are obtained from MC.

- Third order Bernstein polynomials are used as $M(e\gamma)$ templates for missing rare backgrounds like VV, W+jets and γ+jets, etc. Coefficients for these polynomials (a0, a1, a2, a3) are allowed to float during the fit to data.

Pre-fit and Post-fit distributions of $M(e\gamma)$ for different bins of $Z \to e\gamma$ CR are shown in Figure 7.2.

7.3.3 Parameterisation of scale factors

Scale factors have been calculated, in bins of η_γ and photon conversion type, by substituting μ_{Zee} and $\mu_{Ze\gamma}$ in Equation (7.3). These are shown in Figure 7.3 and Table 7.2. In general, the scale factors are larger for central regions, which is expected as the amount of the detector material traversed by photons is smaller compared to the forward regions.

Conversion type/η_γ	(0.0, 0.3)	(0.3, 0.6)	(0.6, 1.0)	(1.0, 1.37)	(1.52, 1.81)	(1.81, 2.37)
Unconverted	1.12 ± 0.0181	0.98 ± 0.0175	1.00 ± 0.0132	1.03 ± 0.0147	1.06 ± 0.0136	1.07 ± 0.0111
SingleSi	2.62 ± 0.0865	1.88 ± 0.0606	1.77 ± 0.0602	1.38 ± 0.0441	1.04 ± 0.0356	1.13 ± 0.0241
SingleTRT	1.81 ± 0.0528	1.52 ± 0.0581	1.08 ± 0.0352	0.92 ± 0.0242	0.93 ± 0.0235	0.96 ± 0.0296
DoubleSi	1.05 ± 0.0178	1.00 ± 0.0157	0.98 ± 0.0115	0.92 ± 0.0114	0.90 ± 0.0109	0.98 ± 0.0065
DoubleTRT	1.29 ± 0.0948	1.12 ± 0.0832	0.86 ± 0.0614	0.98 ± 0.0348	0.92 ± 0.0340	0.83 ± 0.0652
DoubleSiTRT	1.70 ± 0.2426	1.73 ± 0.1781	1.17 ± 0.0674	1.17 ± 0.0442	0.88 ± 0.0240	0.79 ± 0.0357

Table 7.2: Electron-to-photon scale factors in bins of η_γ and photon conversion type

7.4 Closure test in $Z \to e\gamma$ CR

Electron-to-photon scale factors have been tested for closure in $Z \to e\gamma$ CR, the same region from which they are derived. Comparison of Data/MC plots with and without

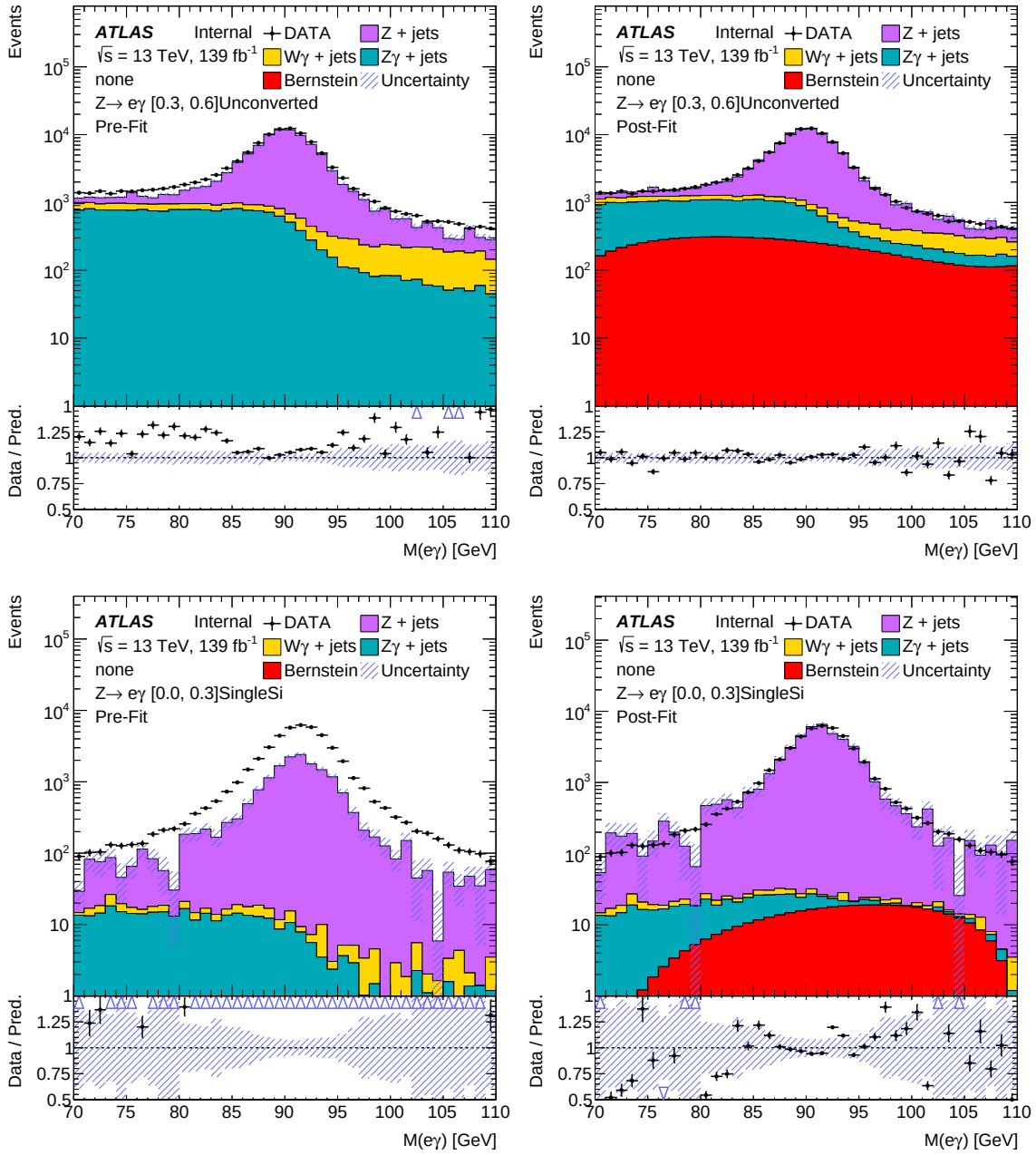

Figure 7.2: Pre-fit (left) and Post-fit (right) distributions of $M(e\gamma)$ [GeV] for $Z \to e\gamma$ CR in different bins: [Unconverted Photon, $\eta_\gamma \in (0.3,\ 0.6)$] (top row), [Converted Photon matched with a single track with hits in Silicon detector, $\eta_\gamma \in (0.0,\ 0.3)$] (bottom row)

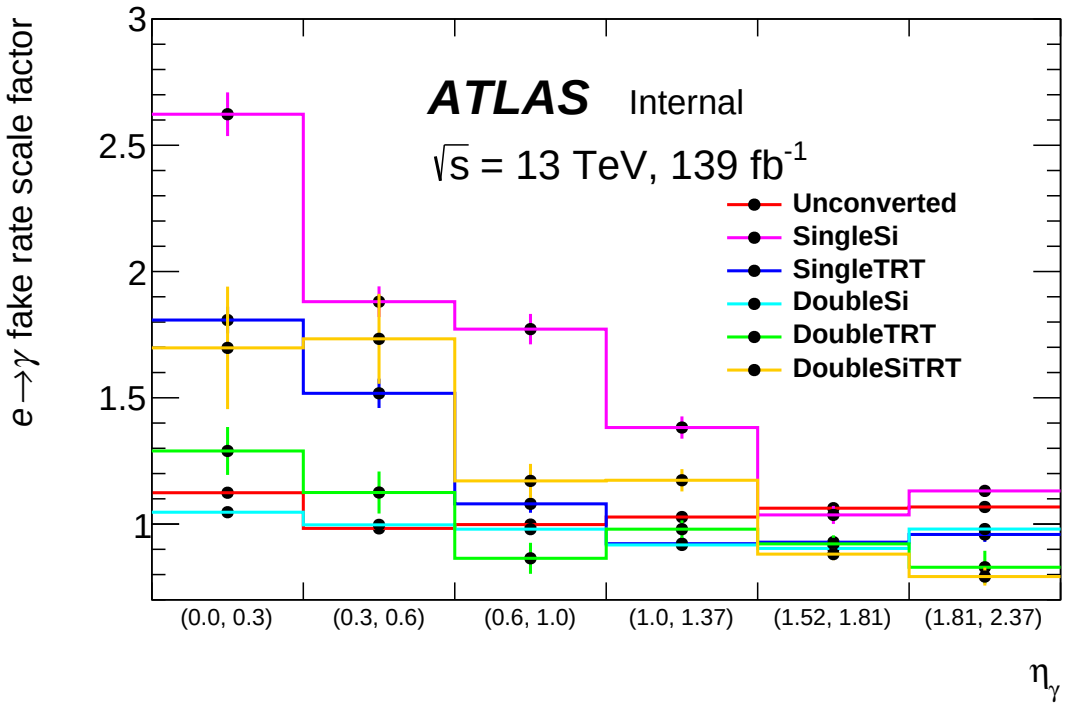

Figure 7.3: Electron-to-photon scale factors in bins of η_γ and photon conversion type

scale factor corrections is presented in Figure 7.4. Scale factor corrections to MC, clearly, improves the agreement with data.

7.5 Validation of scale factors in $Z \to e\gamma$ VR

Scale factor corrections to MC have been tested in $Z \to e\gamma$ validation region. Comparison of data and MC plots before and after applying scale factors, as shown in Figure 7.5, indicates that applying scale factors to MC improves the agreement with data.

7.6 Additional studies: parameterisation in photon p_T

To check if additional parameterisation of scale factors is needed, scale factors have been derived in bins of photon p_T after applying scale factor corrections to MC in bins of η_γ and conversion type. As shown in Figure 7.6, scale factors do not depend on the transverse momentum of photon.

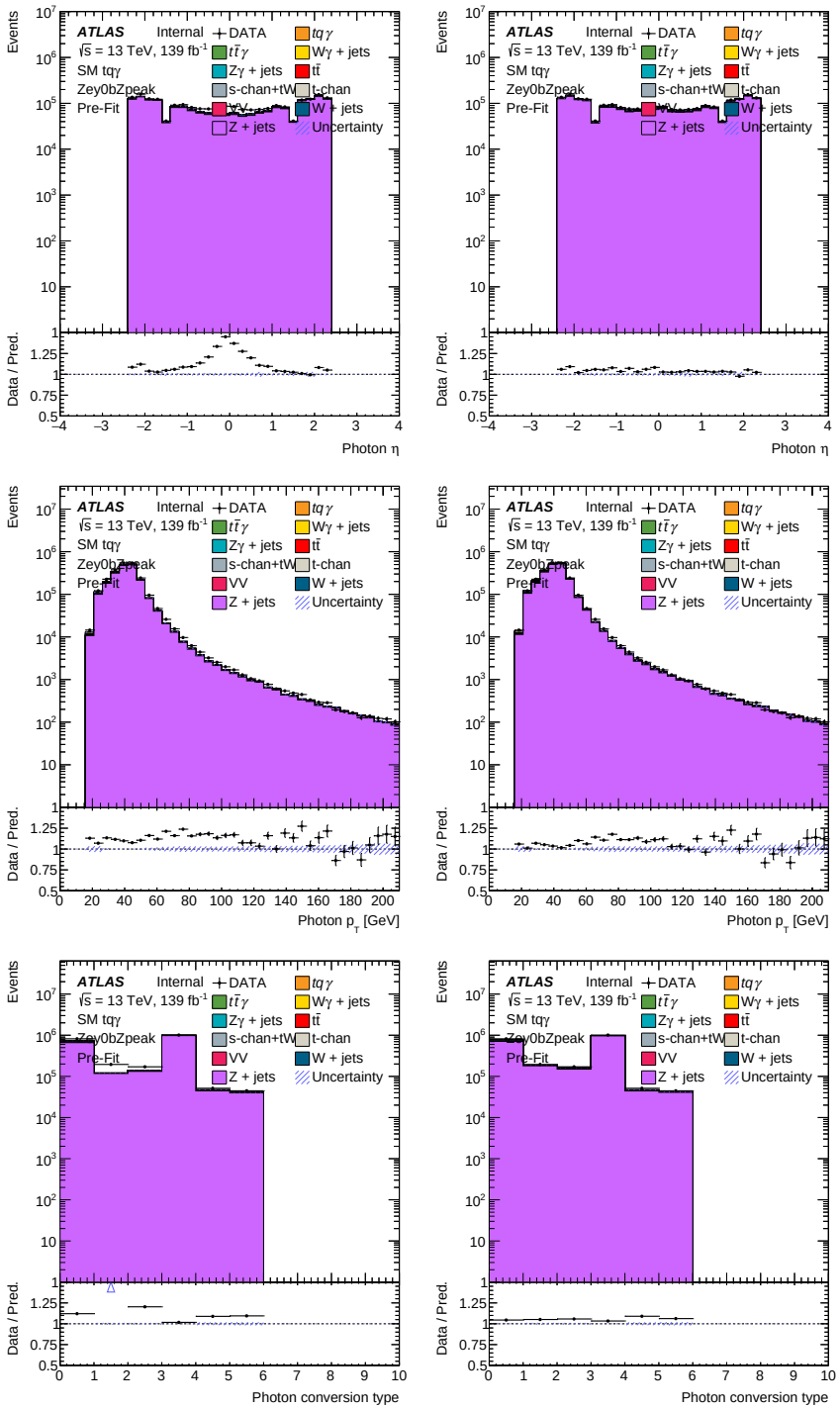

Figure 7.4: Comparison of data and MC plots before (left) and after (right) applying electron-to-photon scale factors for $Z \to e\gamma$ control region

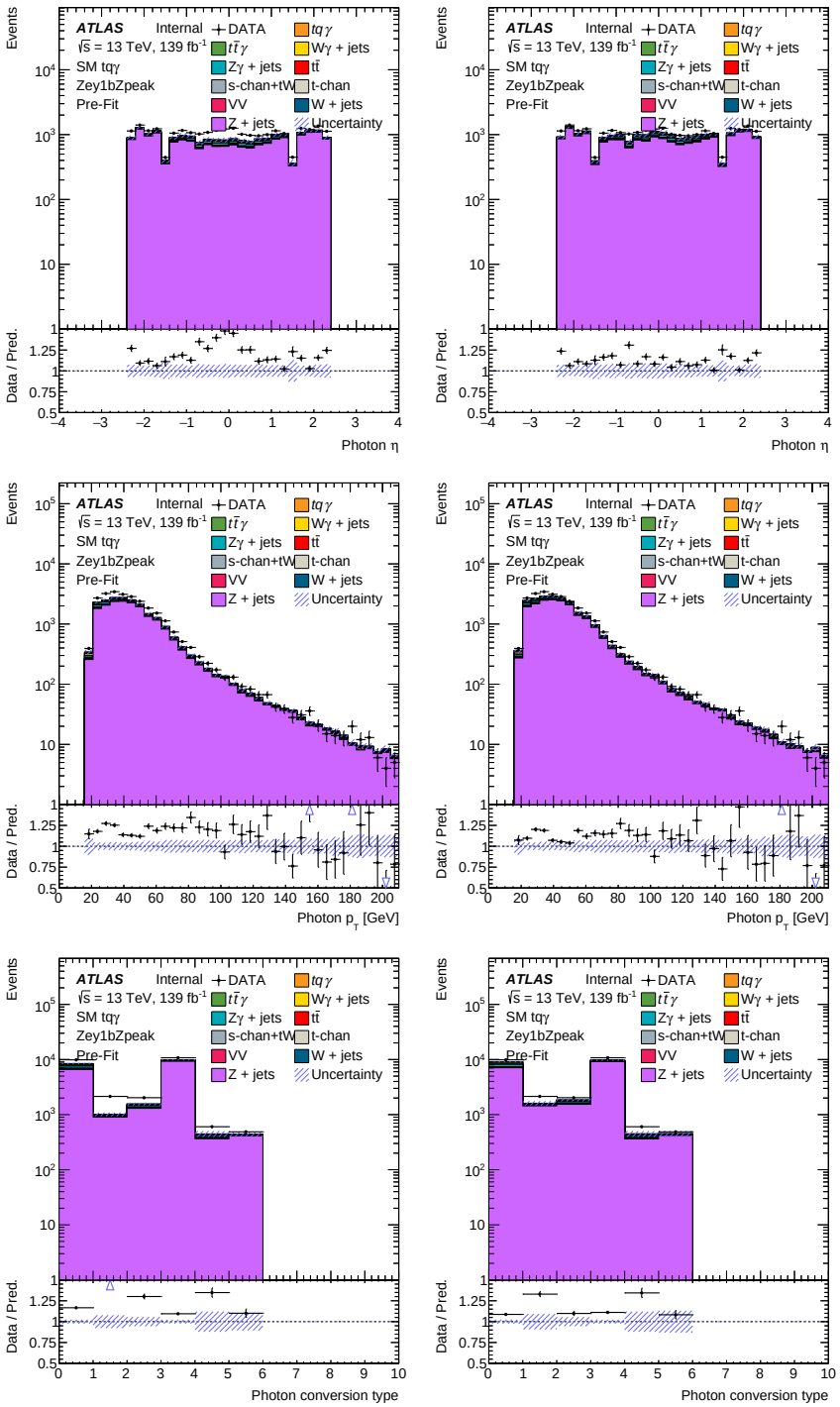

Figure 7.5: Comparison of data and MC plots before (left) and after (right) applying electron-to-photon scale factors for $Z \to e\gamma$ validation region

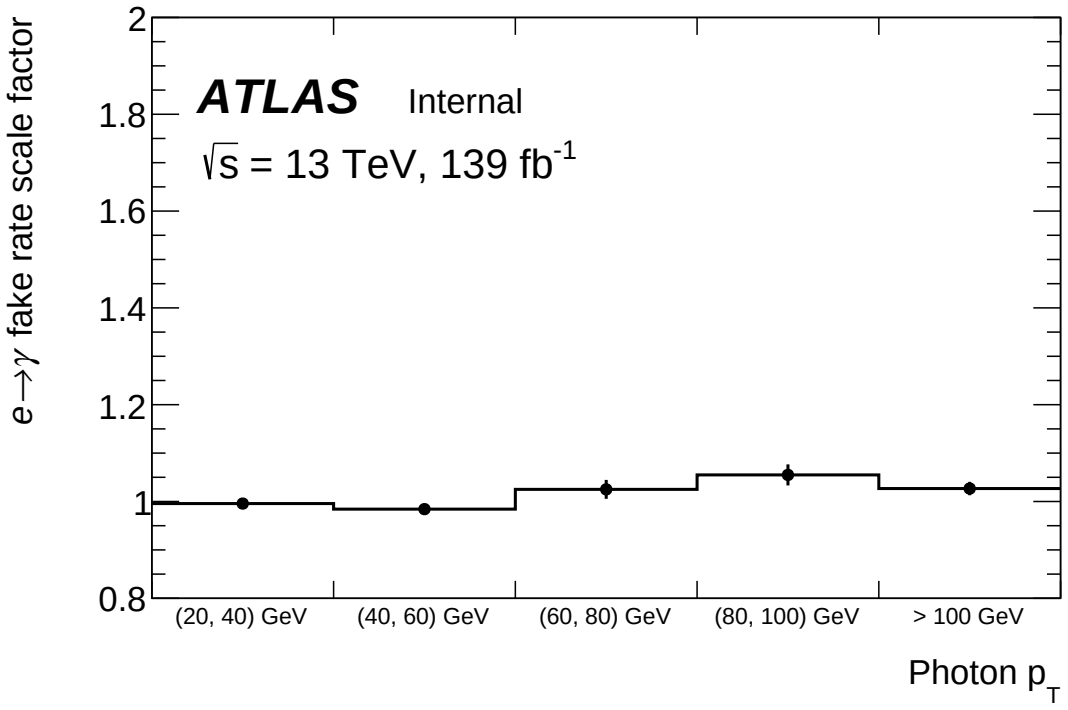

Figure 7.6: Electron-to-photon scale factors in bins of photon p_T after applying scale factors corrections to MC in bins of η_γ and photon conversion type

Chapter Eight: Estimation of fake photon backgrounds due to mis-reconstructed jets

In each proton-proton collision, many jets and hadrons are produced. Hence, it may happen that a jet is mis-identified as a photon or a photon is radiated in a hadron decay, e.g. $\pi^0 \to \gamma\gamma$ decays. These mis-reconstructed hadrons are referred to in the following as $j \to \gamma$ fakes. As the modelling of $j \to \gamma$ fakes is not accurate in the simulation, data driven scale factors are derived using the ABCD method to correct the simulation for any deviation from data.

8.1 ABCD method and control region definitions

The ABCD method exploits the weak correlation between the isolation and the photon ID variables measured in the first layer of the ECAL. The photon isolation variables are constructed using the information retrieved from the outer core of the photon candidate, while the photon ID variables are constructed based on the shape information of the shower induced by the photon candidate in the ECAL. As shown in Table 8.1, different categories of photons are defined based on the ID and isolation variables. More information about these variables can be found in Ref. [53].

category	variables
relaxed-tight narrow-strip	R_{had}, R_ϕ, R_η, $\omega_{\eta 2}$, $\omega_{s,\text{tot}}$ F_{side}, $\omega_{s,3}$, ΔE, E_{ratio}
Loose'2	relaxed-tight+ΔE+E_{ratio}
Loose'3	relaxed-tight+E_{ratio}
Loose'4	relaxed-tight

Table 8.1: Different categories of photons that are used for the tight working point of the photon identification algorithm.

A photon candidate is considered as a `Tight` photon if it passes the criteria defined by the narrow-strip and the relaxed-tight selection.

Different sets of looser photon ID criteria are defined, where a photon candidate is required to fulfill the relaxed-tight criteria, which is referred to as Loose′4. When Loose′3 or Loose′2 criteria are applied, the photon candidate is required to fulfill the tight-ID criterion for E_{ratio} and criteria for E_{ratio} and ΔE. The correlation between the photon isolation and photon ID increases with increasing from Loose′2 to Loose′4. In the nominal ABCD method, the Loose'4 variables are used in order to construct the ABCD regions, where the Loose'2 and Loose'3 definitions are used to derive systematic uncertainties for the $j \to \gamma$ estimation. This weak correlation is exploited for the definition of the ABCD regions which are defined as follows:

- Hadron fake region (HFR) A: the photon candidate passes the isolation criteria but fails at least one of the tight-ID criteria and passes the Loose'4 criteria
- HFR B: the photon candidate fails the isolation criteria and at least one of the tight-ID criteria and passes the Loose'4 criteria
- HFR C: the photon candidate fails the isolation criteria and passes the tight-ID
- HFR D: the photon candidate passes the photon isolation and passes the tight-ID

The photon candidate is considered as failing the isolation criteria only when it fails both, the track and calorimeter isolation criteria. Imposing this requirement reduces the amount of prompt photons in the non-isolated regions and therefore, increases the fraction of the $j \to \gamma$ contribution in these regions.

The definitions of the HFRs are shown in Figure 8.1 and in Table 8.2. Here, the definition of the HFR D is given by the definition of the pre-selection region.

The measurement of the $j \to \gamma$ is performed for converted and unconverted photons, separately, in the following six $|\eta^{\gamma}|$ and to p_{T}^{γ} bins of the leading photon:

$$
\begin{aligned}
|\eta^{\gamma}| : &\quad [0, 0.3),\ [0.3, 0.6),\ [0.6, 1.0),\ [1.0, 1.37),\ [1.52, 1.81),\ [1.81, 2.37] \\
p_{\text{T}}^{\gamma} : &\quad [20, 40)\ ,\ [40, \text{inf}]
\end{aligned}
$$

Due to this weak correlation that the validity of Equation (8.1) can be assumed and can be used in order to estimate the contribution of $j \to \gamma$ in the SR.

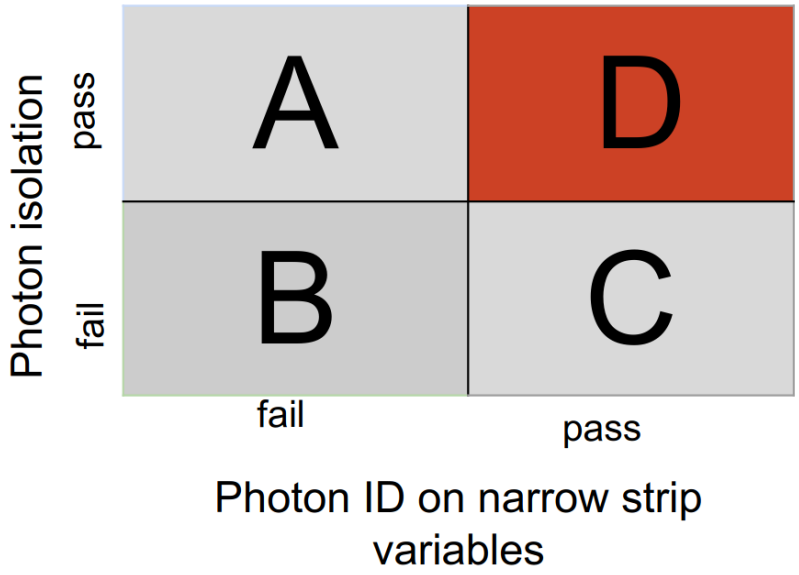

Figure 8.1: Regions used in the ABCD method for the estimation of $j \to \gamma$ scale factors

Object/Variable	HFR A	HFR B	HFR C
Photons	≥ 1 w/ $p_T > 20$ isolated fail Loose'4	≥ 1 w/ $p_T > 20$ not isolated fail Loose'4	≥ 1 w/ $p_T > 20$ not isolated pass Loose'4
Lepton	$= 1$ w/ $p_T > 27$	$= 1$ w/ $p_T > 27$	$= 1$ w/ $p_T > 27$
Jets	>1 w/ $p_T > 25$	>1 w/ $p_T > 25$	>1 w/ $p_T > 25$
being b-tagged	$= 1$ DL1r 70%	$= 1$ DL1r 70%	$= 1$ DL1r 70%
E_T^{miss}	> 30	> 30	> 30
$m_{e\gamma}$	not in [80, 100]	not in [80, 100]	not in [80, 100]

Table 8.2: Definitions of the HFRs used for the ABCD method to estimate the $j \to \gamma$ contribution in the pre-selection region.

$$\frac{N^{j\to\gamma}(A)}{N^{j\to\gamma}(B)} \approx \frac{N^{j\to\gamma}(D)}{N^{j\to\gamma}(C)} \tag{8.1}$$

As in data the classification of photons in the three different types cannot be made, the yields observed in each region have to be corrected for the prompt and

$e \to \gamma$ fake contribution. This is done by subtracting the prompt photon and $e \to \gamma$ fake contributions estimated from MC from the observed data yields. Therefore, the number of hadron-fakes in data in region i is given by the following equation:

$$N_{\text{data}}^{j\to\gamma}(i) = N_{\text{data}}(i) - N_{\text{MC}}^{\text{prompt}}(i) - \text{SF}(e \to \gamma) \times N_{\text{MC}}^{e\to\gamma}(i) \tag{8.2}$$

Consequently, the contribution of hadron fakes in the SR can be estimated by

$$N_{\text{data}}^{j\to\gamma}(D) = \frac{N_{\text{data}}^{j\to\gamma}(A) \cdot N_{\text{data}}^{j\to\gamma}(C)}{N_{\text{data}}^{j\to\gamma}(B)} \tag{8.3}$$

Finally, the data/MC SF for hadron fakes is given by

$$SF(j \to \gamma) = \frac{N_{\text{data}}^{j\to\gamma}(D)}{N_{\text{MC}}^{j\to\gamma}(D)} \tag{8.4}$$

8.2 Results for $j \to \gamma$ SFs

The resulting $j \to \gamma$ SFs are shown in Figures 8.2 and 8.3 for the different $|\eta^{\gamma}|$ and p_{T}^{γ} for converted and unconverted photons, respectively. The uncertainty bars show the total uncertainties as well as the statistical and systematic components of it. The systematic uncertainties on the SFs are estimated by including the following sources of uncertainties:

- Limited data and MC statistics
- Variation of SF($e \to \gamma$)
- Switching to different Loose'i
- Variation of $\sigma_{t\bar{t}}$ and $\sigma_{t\bar{t}\gamma}$

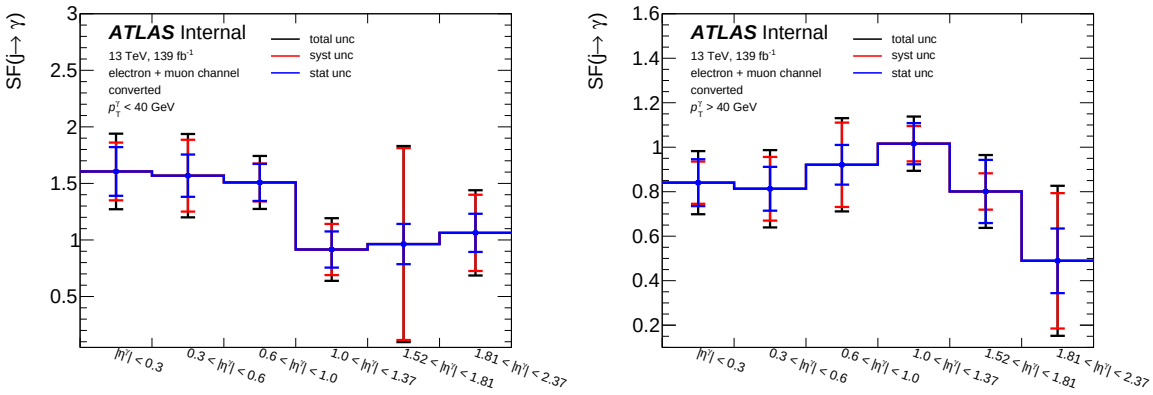

Figure 8.2: Resulting $j \to \gamma$ SFs for converted photons.

The numerical values of the SFs are shown in Table 8.3. These SFs are applied to the $j \to \gamma$ contributions in all considered regions in this analysis.

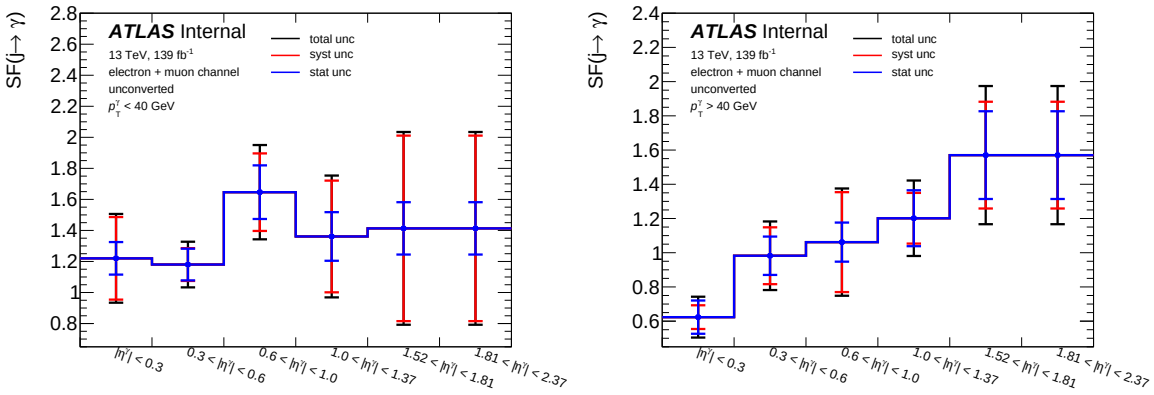

Figure 8.3: Resulting $j \to \gamma$ SFs for unconverted photons.

$\lvert\eta^{\gamma}\rvert$	converted		unconverted	
	$p_{\mathrm{T}}^{\gamma} < 40$	$p_{\mathrm{T}}^{\gamma} > 40$	$p_{\mathrm{T}}^{\gamma} < 40$	$p_{\mathrm{T}}^{\gamma} > 40$
[0, 0.3)	$1.60 \pm 0.22 \pm 0.26$	$0.84 \pm 0.11 \pm 0.09$	$1.22 \pm 0.10 \pm 0.27$	$0.62 \pm 0.10 \pm 0.07$
[0.3, 0.6)	$1.57 \pm 0.19 \pm 0.32$	$0.81 \pm 0.10 \pm 0.14$	$1.18 \pm 0.10 \pm 0.11$	$0.98 \pm 0.11 \pm 0.17$
[0.3, 1.0]	$1.51 \pm 0.16 \pm 0.17$	$0.92 \pm 0.09 \pm 0.19$	$1.65 \pm 0.17 \pm 0.25$	$1.06 \pm 0.11 \pm 0.29$
[1.0, 1.37)	$0.92 \pm 0.16 \pm 0.23$	$1.02 \pm 0.09 \pm 0.08$	$1.36 \pm 0.16 \pm 0.36$	$1.20 \pm 0.16 \pm 0.15$
[1.52, 1.81)	$0.96 \pm 0.18 \pm 0.85$	$0.80 \pm 0.14 \pm 0.08$	$1.41 \pm 0.17 \pm 0.60$	$1.57 \pm 0.26 \pm 0.31$
[1.81, 2.37)	$1.06 \pm 0.17 \pm 0.34$	$0.49 \pm 0.15 \pm 0.30$	$1.41 \pm 0.17 \pm 0.60$	$1.57 \pm 0.26 \pm 0.31$

Table 8.3: Resulting $j \to \gamma$ SFs. The first value in each row and column correspond to the nominal value, where the second and third value correspond to the statistical and systematic uncertainty of the SFs, respectively.

Chapter Nine: Background validation & Pre-selection region plots

In this chapter, leading backgrounds of the $tq\gamma$ analysis are validated in dedicated control regions. $t\bar{t}\gamma$ background is validated in Section 9.1. Section 9.2 presents the validation plots of $W\gamma$ background process. Data/MC comparison plots for the pre-selection region are illustrated in Section 9.3.

9.1 $t\bar{t}\gamma$ control region

$t\bar{t}\gamma$ control region is defined by the following selection criteria.

- Exactly one lepton
- At least one photon
- Exactly 1 b-tagged jet at 70% WP and at least two b-tagged jets at 85% WP of the DL1r algorithm
- Missing p_T > 30 GeV
- $M(e\gamma) \notin (80, 100)$ GeV

The only difference with respect to the pre-selection region is the number of b-jets is required to be at least 2 at DL1r-85% working point. Overall purity of $t\bar{t}\gamma$ yield in this region is 48%. The observed and expected number of events for different processes are presented in Table 9.1. The composition of this region with respect to the different photon origins and to the different background processes is illustrated in 9.1. Data/MC comparison plots for $t\bar{t}\gamma$ control region are illustrated in Figures 9.2 and 9.3.

Process	Yield
$tq\gamma$	548.366 ± 16.0655
$t\bar{t}\gamma$	8854.52 ± 17.697
$W\gamma$ + jets	885.014 ± 29.3585
$Z\gamma$ + jets	359.127 ± 13.7014
$t\bar{t}$	6306.99 ± 32.6307
s-chan	23.8228 ± 0.886865
tW	801.467 ± 10.7679
t-chan	283.752 ± 4.22656
VV	14.7281 ± 0.940961
W + jets	87.9167 ± 16.4917
Z + jets	98.9954 ± 11.1118
Total	18264.7 ± 56.157
DATA	19119

Table 9.1: Yields of signal and background processes in the $t\bar{t}\gamma$ control regions. Only statistical uncertainties are included in the calculation.

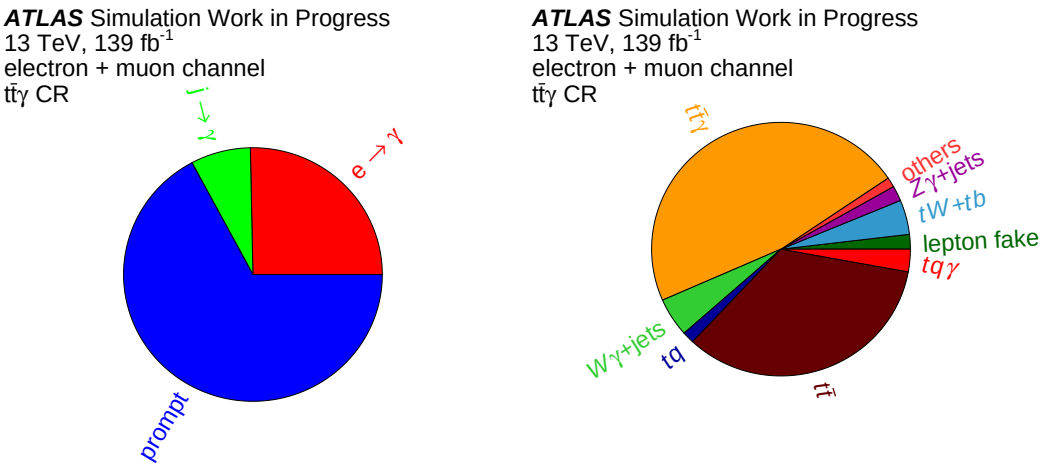

Figure 9.1: Composition of the $t\bar{t}\gamma$ control region region with respect to the photon origin (left) and to the different processes (right).

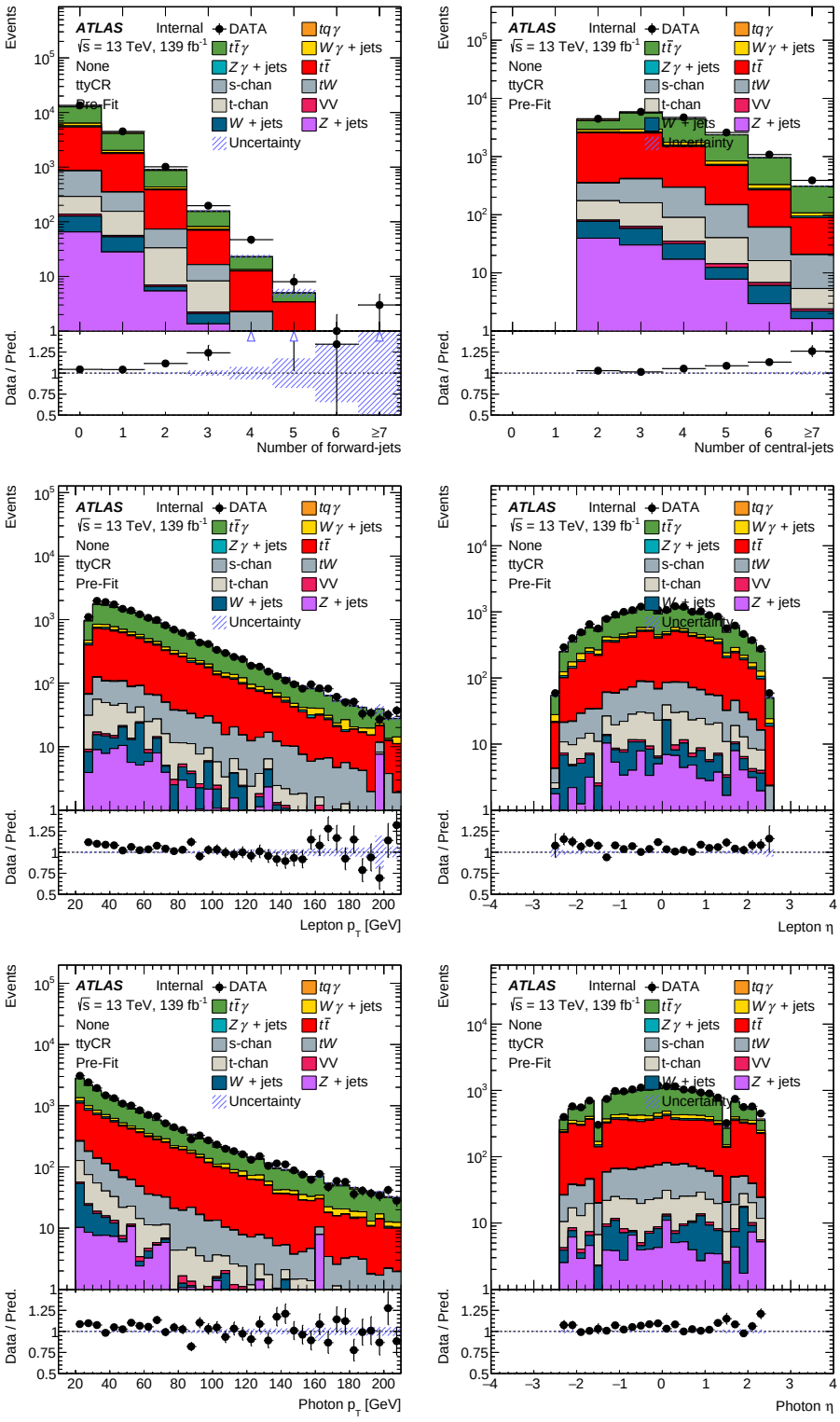

Figure 9.2: $t\bar{t}\gamma$ control region plots

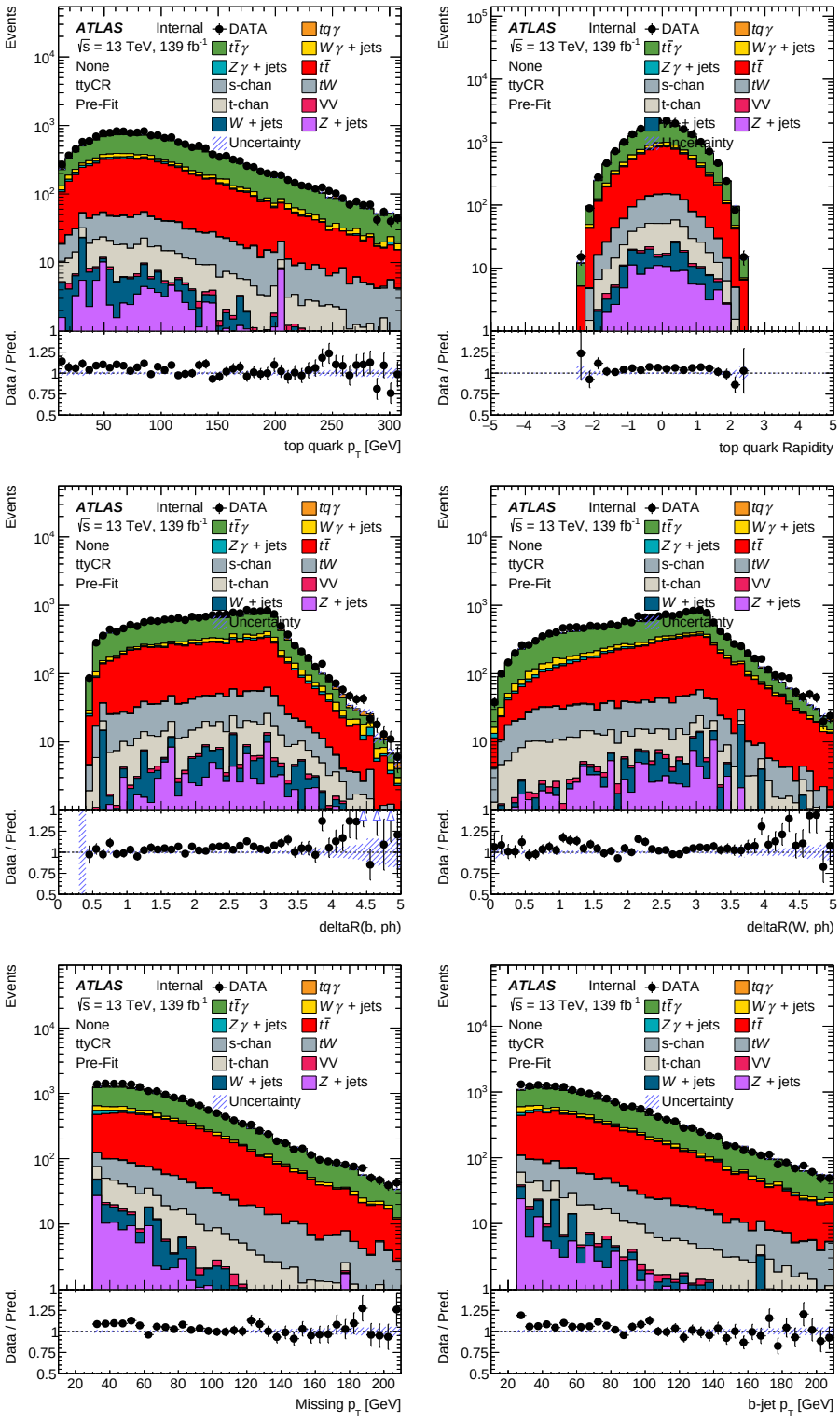

Figure 9.3: $tt\bar{}\gamma$ control region plots

9.2 $W\gamma$ control region

$W\gamma$ control region definition:

- Exactly one lepton
- At least one photon
- No b-tagged jets at 70% WP of the DL1r algorithm
- Missing p_T > 30 GeV
- $M(e\gamma) \notin (80, 100)$ GeV

It is orthogonal to the pre-selection region as the number of b-jets is required to be zero at DL1r-70% working point. Purity of $W\gamma$ events in this region is 51 %. The observed and expected number of events for different processes are presented in Table 9.2. The composition of this region with respect to the different photon origins and to the different background processes is illustrated in 9.4. Data/MC comparison plots for $W\gamma$ control region are illustrated in Figure 9.5.

Process	Yield
$tq\gamma$	857.031 ± 20.3278
$t\bar{t}\gamma$	6446.47 ± 14.9794
$W\gamma$ + jets	27791.6 ± 187.28
$Z\gamma$ + jets	6798.11 ± 56.4213
$t\bar{t}$	4779.01 ± 28.3664
s-chan	22.5721 ± 0.871548
tW	1218.81 ± 13.2457
t-chan	442.85 ± 5.13729
VV	402.668 ± 6.36916
W + jets	3309.72 ± 345.308
Z + jets	2039.67 ± 143.221
Total	54108.5 ± 420.612
DATA	61670

Table 9.2: Yields of signal and background processes in the $W\gamma$ control regions. Only statistical uncertainties are included in the calculation.

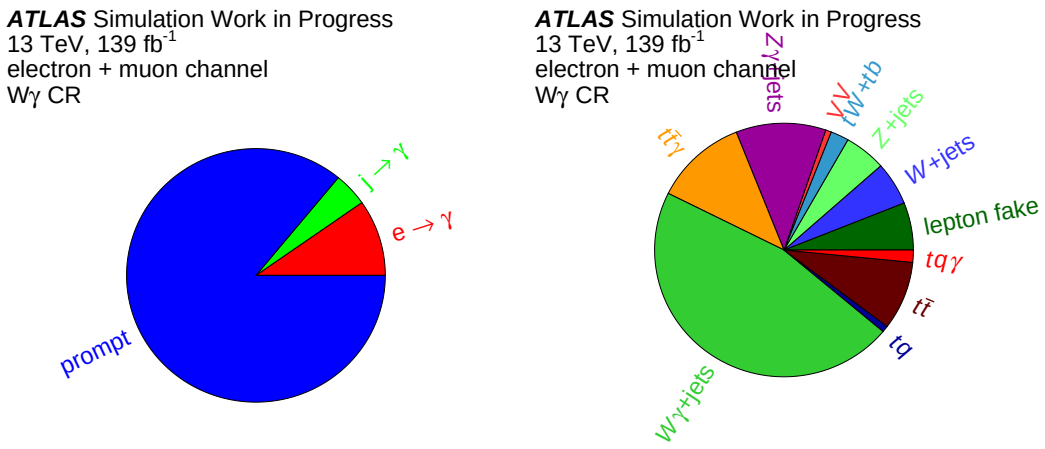

Figure 9.4: Composition of the $W\gamma$ control region region with respect to the photon origin (left) and to the different processes (right).

9.3 Pre-selection region plots

Pre-selection region is defined by the following selection criteria:

- Exactly one lepton
- At least one photon
- Exactly 1 b-tagged jet at 70% and 85% WPs of the DL1r algorithm
- Missing p_T > 30 GeV
- $M(e\gamma) \notin (80, 100)$ GeV

S/B in the pre-selection region is 5.4%. The observed and expected number of events for different processes are presented in Table 9.3. The composition of this region with respect to the different photon origins and to the different background processes is illustrated in 9.6 Data/MC comparison plots for the pre-selection region are illustrated in Figures 9.7 and 9.8.

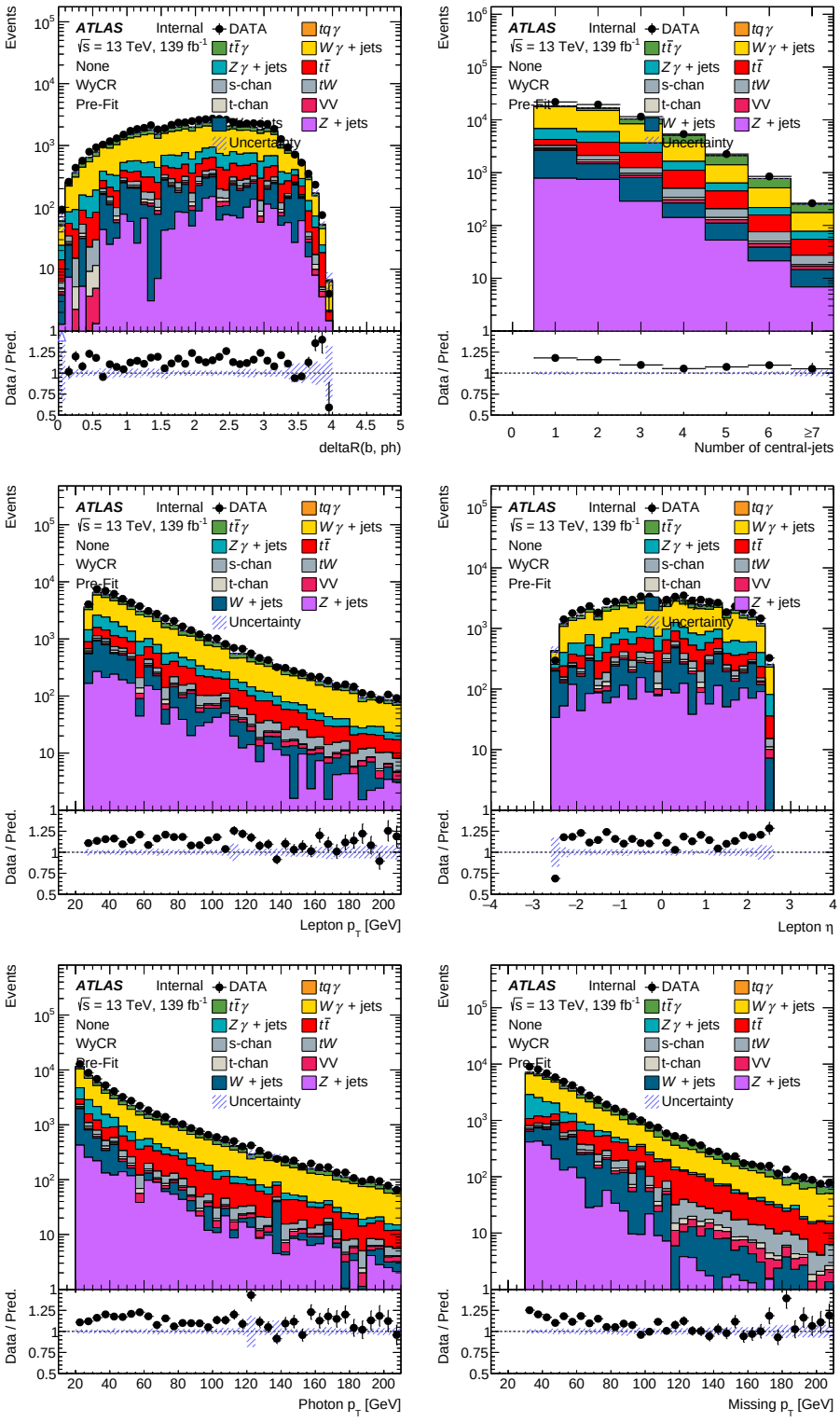

Figure 9.5: $W\gamma$ control region plots

Process	Yield
$tq\gamma$	3428.41 ± 39.6025
$t\bar{t}\gamma$	19814.9 ± 25.8841
$W\gamma$ + jets	10468.5 ± 110.564
$Z\gamma$ + jets	3350.23 ± 39.3838
$t\bar{t}$	17917.3 ± 53.8612
s-chan	76.6172 ± 1.57179
tW	4145.94 ± 24.1357
t-chan	1651.71 ± 9.83593
VV	124.105 ± 3.65797
W + jets	1027.24 ± 137.636
Z + jets	1037.05 ± 70.6005
Total	63042 ± 208.536
DATA	66078

Table 9.3: Yields of signal and background processes in the pre-selection region. Only statistical uncertainties are included in the calculation.

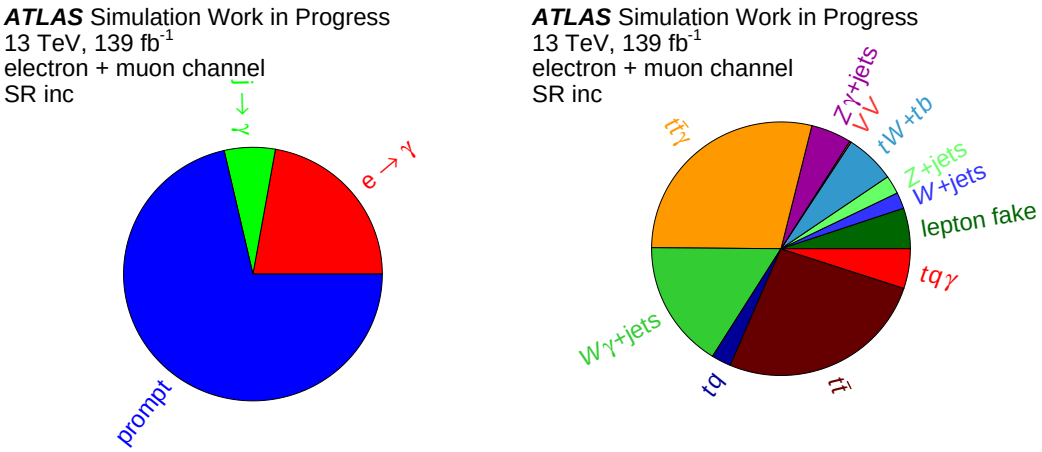

Figure 9.6: Composition of the pre-selection region with respect to the photon origin (left) and to the different processes (right).

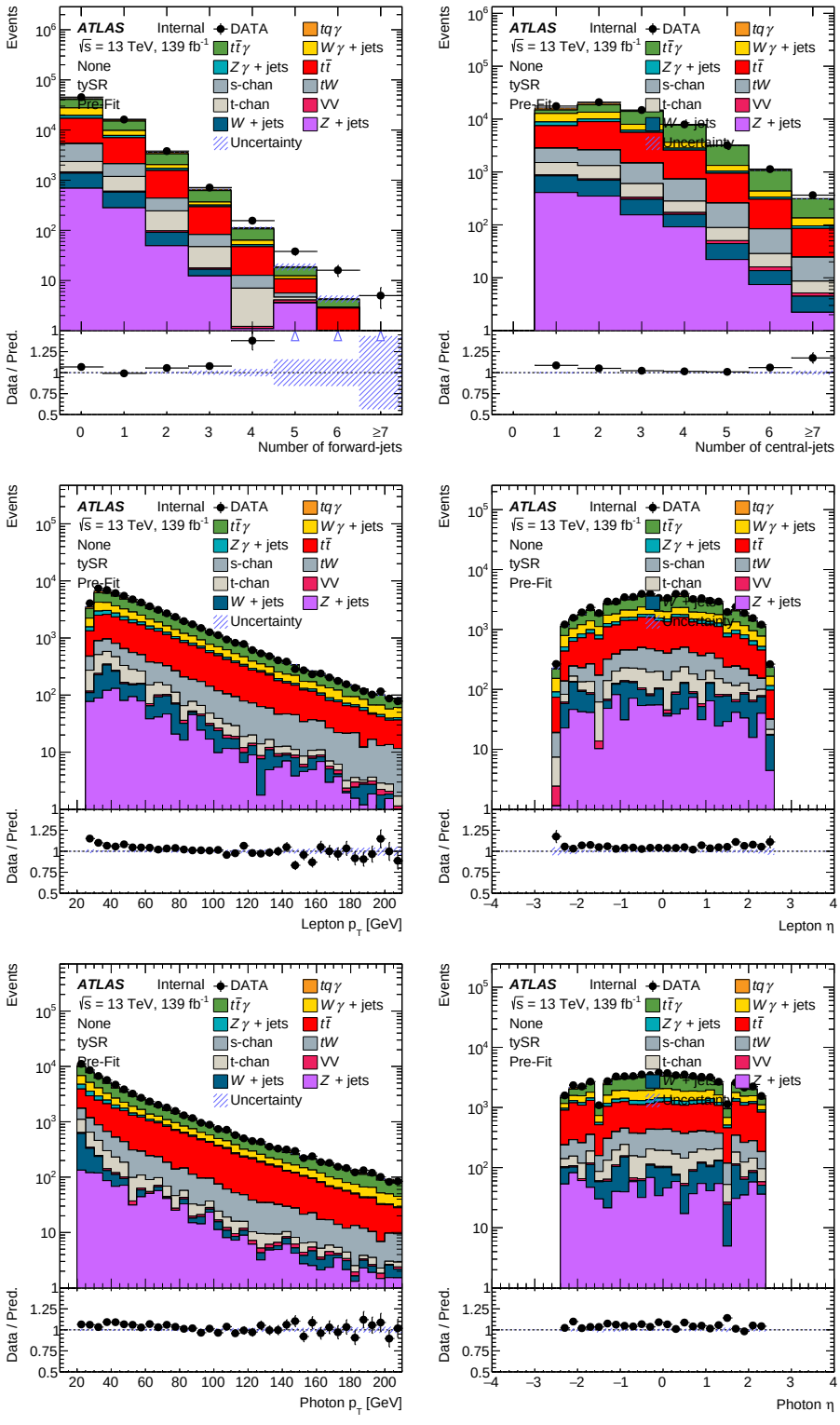

Figure 9.7: Pre-selection region plots

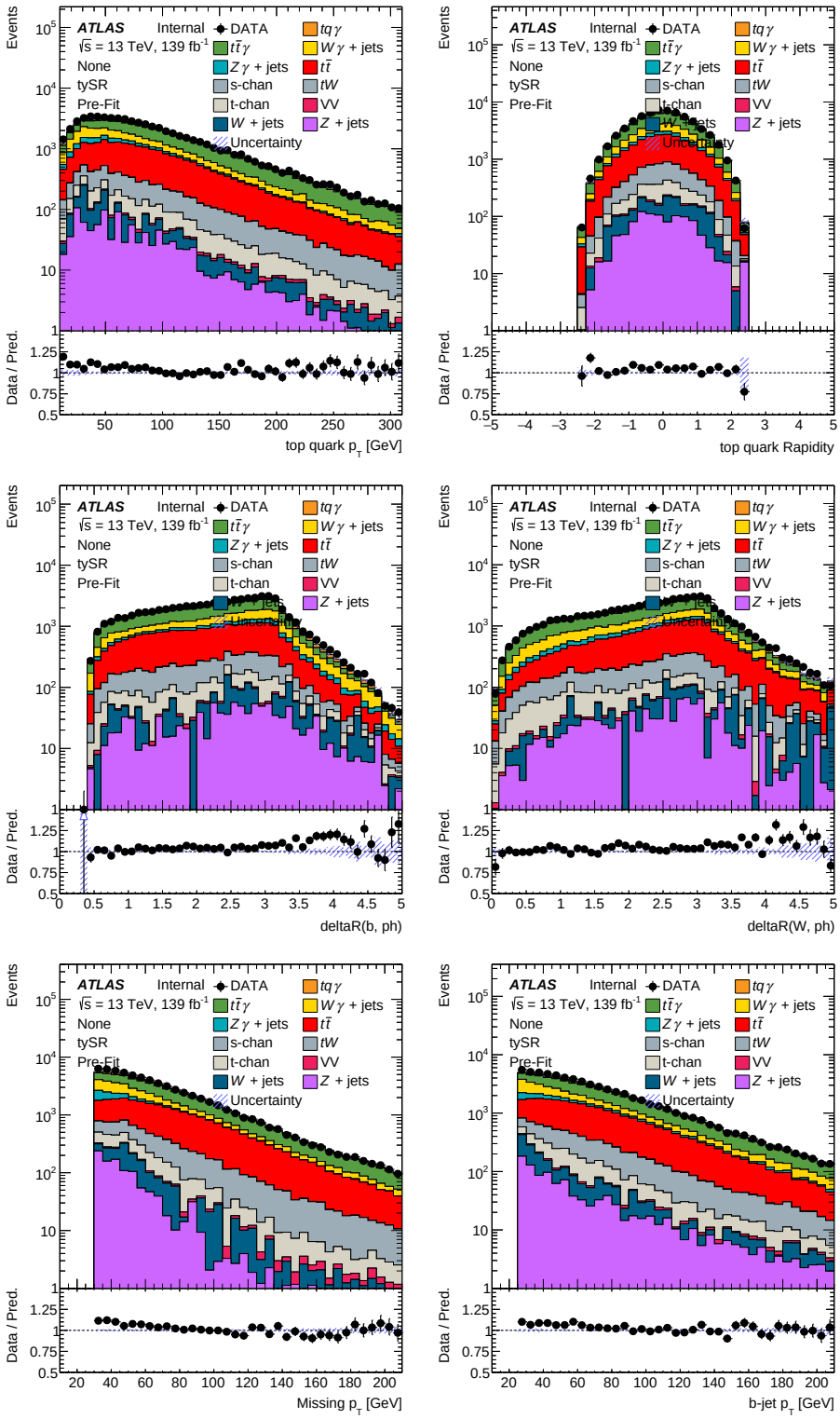

Figure 9.8: Pre-selection region plots

Chapter Ten: Separation of signal events from background events

As described in the previous section, major backgrounds for $tq\gamma$ process arise from $t\bar{t}$, $t\bar{t}\gamma$ and $W\gamma$+jets events. To distinguish between signal and background events, a deep-learning, neural network based approach is used.

10.1 Signal region categorization

In order to optimize the sensitivity of the analysis, the signal region is classified into two categories based on number of forward jets: Zero-forward jet region ("**0-fj**") or At least one forward jet region ("≥**1-fj**"). This is motivated by the fact that S/B is high for bins corresponding to nfjets>0 compared to nfjets==0, as illustrated in Figure. Signal and background composition for these two regions are shown in Figure. Expected yields are presented in Table.

Two different neural networks, one for each region, are trained to separate signal from background.

10.2 Architecture of the neural networks

The neural networks are implemented using `Keras` library, with `TensorFlow` as the backend. Each network consists of one input layer, two hidden layers and one output layer. The input layer contains n nodes, where n = number of input features. Each hidden layer has n+1 nodes and the output layer has a single node. All layers are dense, i.e., each node in a layer is connected to all nodes present in the previous and next layer. For input and hidden layers, the Leaky Rectified Linear Unit (ReLU) function $f(x)$ is used as the activation function.

$$f(x) = \begin{cases} x, & \text{if } x \geq 0 \\ 0.05x, & \text{if } x < 0\,. \end{cases} \tag{10.1}$$

For the output layer, the sigmoid function $\sigma(x)$ is used as theactivation function:

$$\sigma(x) = \frac{1}{1 + e^{-x}} \tag{10.2}$$

Binary cross-entropy function is used as the loss function. `Adam` algorithm is used as the optimizer for the network for updating the weights of each node during training. Accuracy and Area Under the ROC Curve (AUC) are used metrics during the neural network training.

$$loss = -\sum_{i}^{N_{\text{entries}}} \Big[p(i) \log q(i) + (1 - p(i)) \log (1 - q(i)) \Big]\,. \tag{10.3}$$

10.2.1 Input features for the neural networks

A total of 135 (94) kinematic and topological variables are considered as inputs for the neural network in $\geq$ 1-fj (0-fj) category. Using `XGBoost`, feature importance score is calculated for all of these variables. Ranking of all variables based on the feature importance score for $\geq$ 1-fj and 0-fj categories is presented in Figures 10.1 and 10.2, respectively.

In each category, variables that are ranked high in the feature importance plot are selected as the input features for the NN. Table 10.1 lists the input variables used for training the neural network in 0-fj and $\geq$ 1-fj cateogries. To reduce theoretical systematic uncertainties, maximum value for njets and nfjets is set at 4. Data/MC comparison plots for input variables are shown in Figures 10.3, 10.4, 10.5 for 0-fj category and Figures 10.6, 10.7, 10.8 for $\geq$ 1-fj category.

Variable	0-fj	$\geq$ 1-fj
b-jet η	X	
Number of jets	X	X
$\Delta\eta(b,\ \gamma)$	X	X
Transverse mass	X	X
Top quark mass	X	X
p_T of $(b+\gamma)$	X	
Invariant mass of $(b+\ell)$	X	X
b-jet pseudo-continuous tag weight bin	X	X
Invariant mass of $(b+\gamma)$	X	X
b-jet p_T	X	
p_T of (top-quark + γ)	X	
Lepton ID	X	X
$\Delta\eta(b,\ \ell)$	X	X
Missing transverse momentum	X	
$\Delta R(b,\ \ell)$	X	
Invariant mass of (b+forward-jet)		X
Invariant mass of $(\ell+\gamma)$		X
$cos(\theta)$ $(\gamma,$ leading forward-jet)		X
HT		X
p_T of leading forward-jet		X
$\Delta\eta$(leading forward-jet, γ)		X
Energy of $(\gamma,$ leading forward-jet)		X
Is leading non b-tagged jet $\eta\ > 2.5$?		X
Number of forward-jets		X
Energy of W-boson		X
Total variables	15	19

Table 10.1: List of variables used as input features of the NN for 0-fj and $\geq$1-fj regions

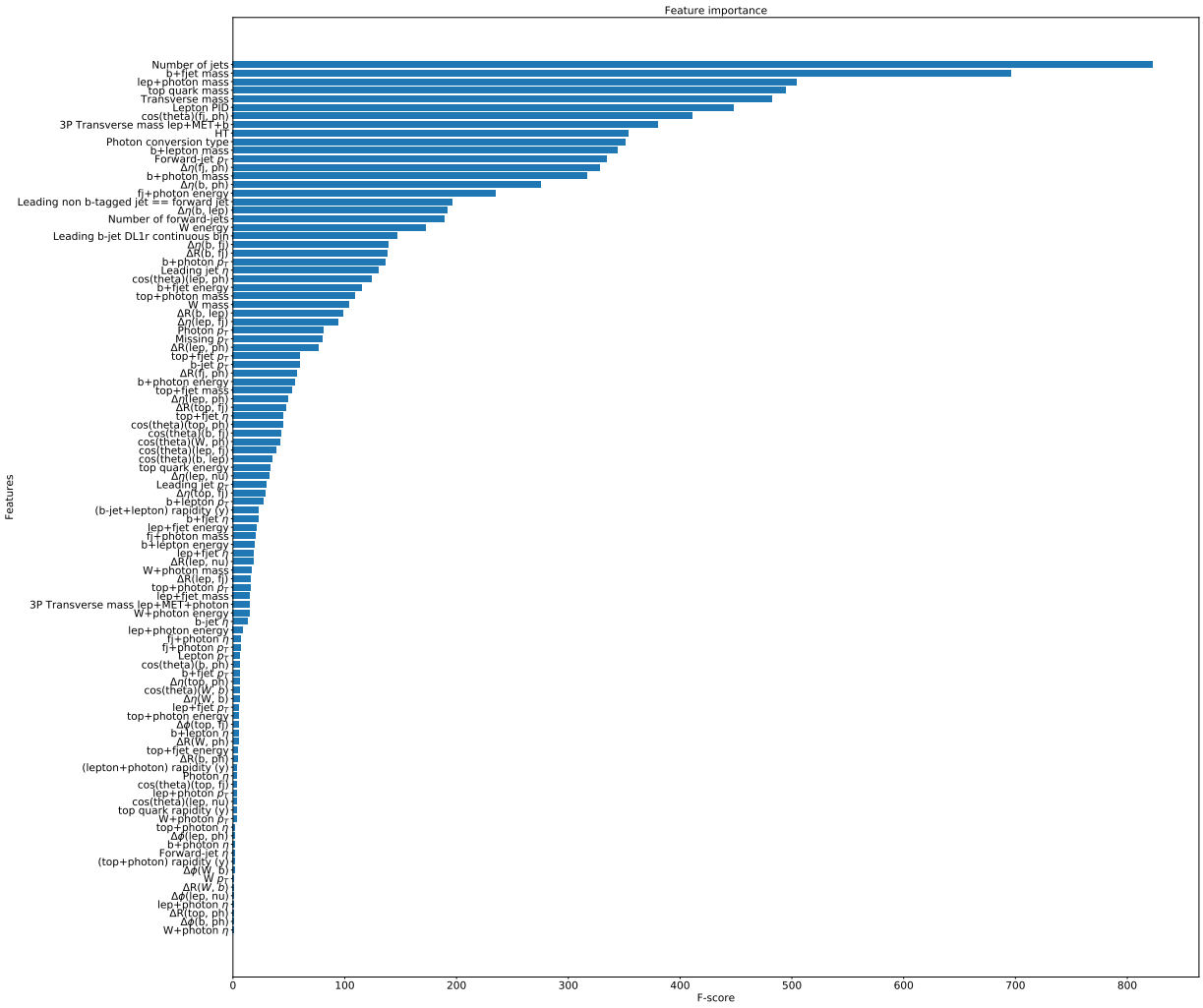

Figure 10.1: Feature importance plot for $\geq$ 1-fj category

10.3 Training of the neural networks

Before the input features are provided to the NN, they are transformed into a range [0, 1] using the following equation.

$$X_{\text{std}} = \frac{X - X.\min(\text{axis}=0)}{X.\max(\text{axis}=0) - X.\min(\text{axis}=0)} \tag{10.4}$$

The events are labeled as 0 (=background) and 1 (=signal) and the event weights are included in the training progress. The full sample is split into three subsamples

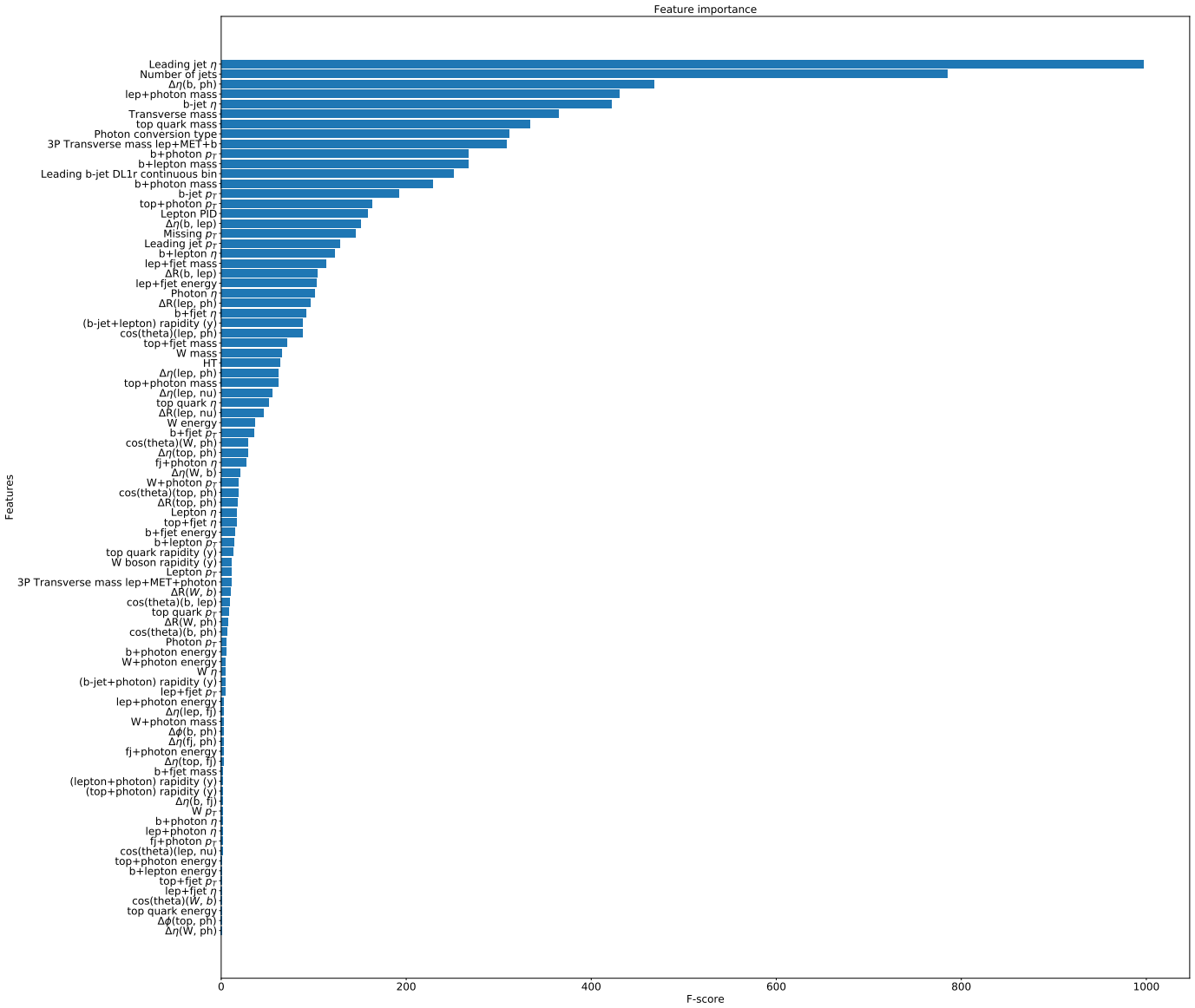

Figure 10.2: Feature importance plot for 0-fj category

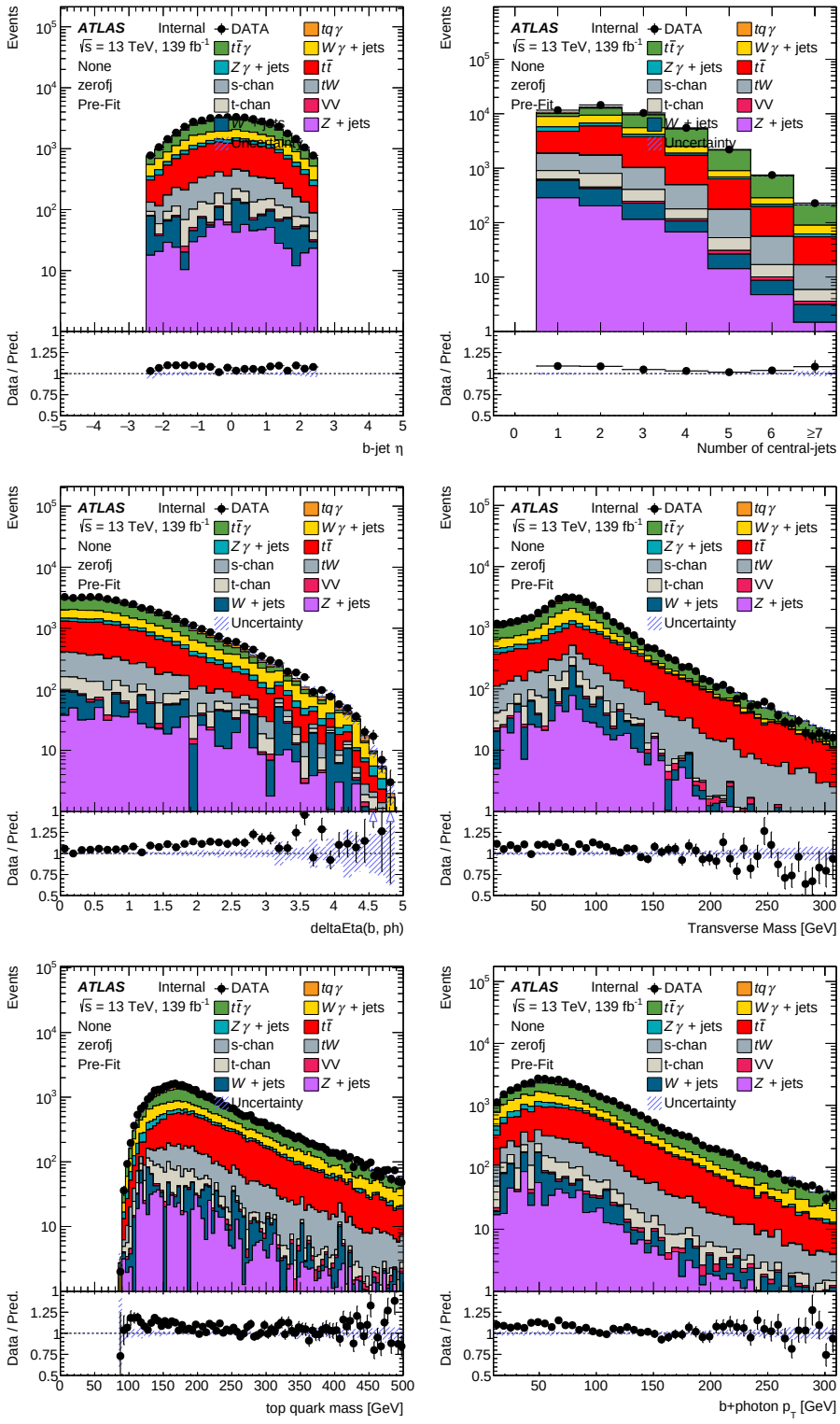

Figure 10.3: Input variable plots for 0-fj category

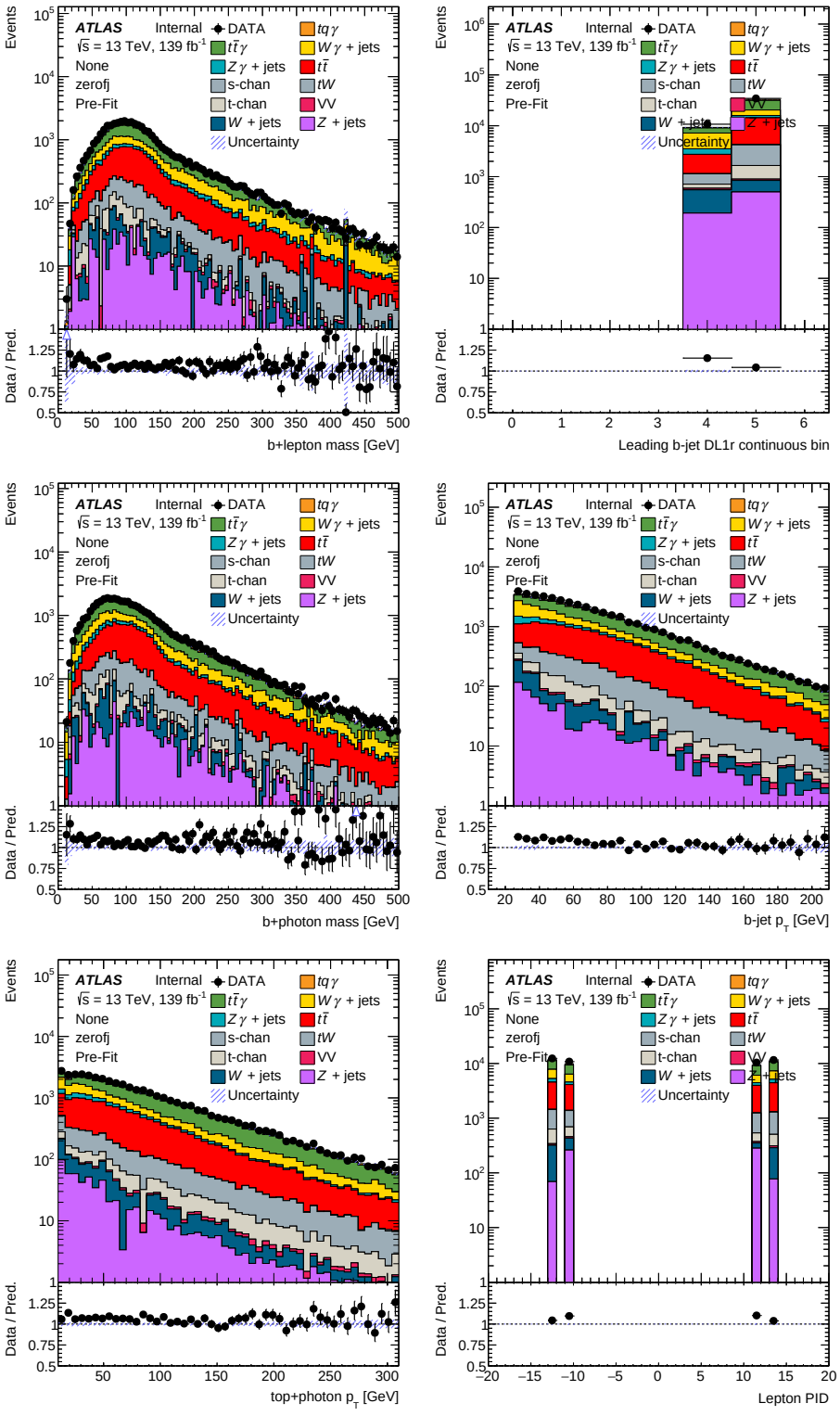

Figure 10.4: Input variable plots for 0-fj category

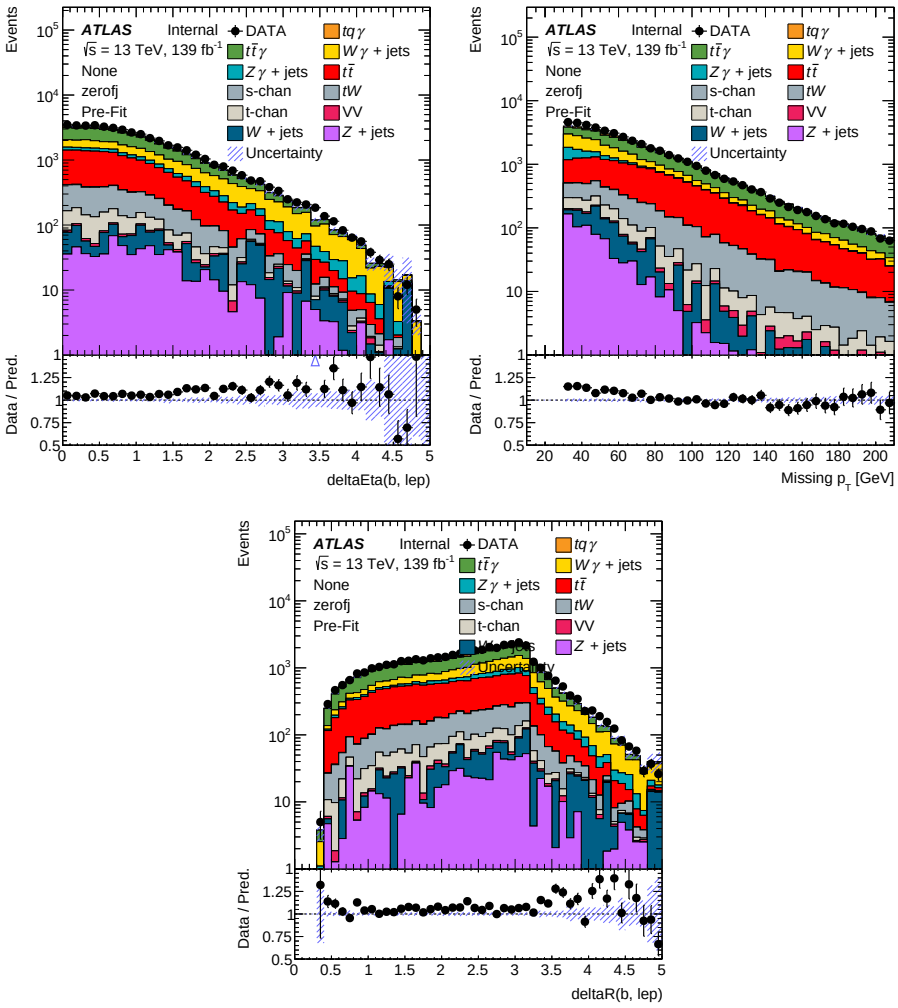

Figure 10.5: Input variable plots for 0-fj category

where it is ensured that all of these samples have nearly the same relative signal and background compostions and that the events are divided randomly into these three subsamples in order to avoid any bias due to the sample composition. One of the subsamples is used for the training of the NN where one validates the training progress. After the training, the third subsample is analyzed by processing the events through the NN and predicting if the events are "signal-like" or "background-like" events.

To ensure that the background is not favored in the training process as the sum of weights of the background processes is much larger compared to the sum of weights

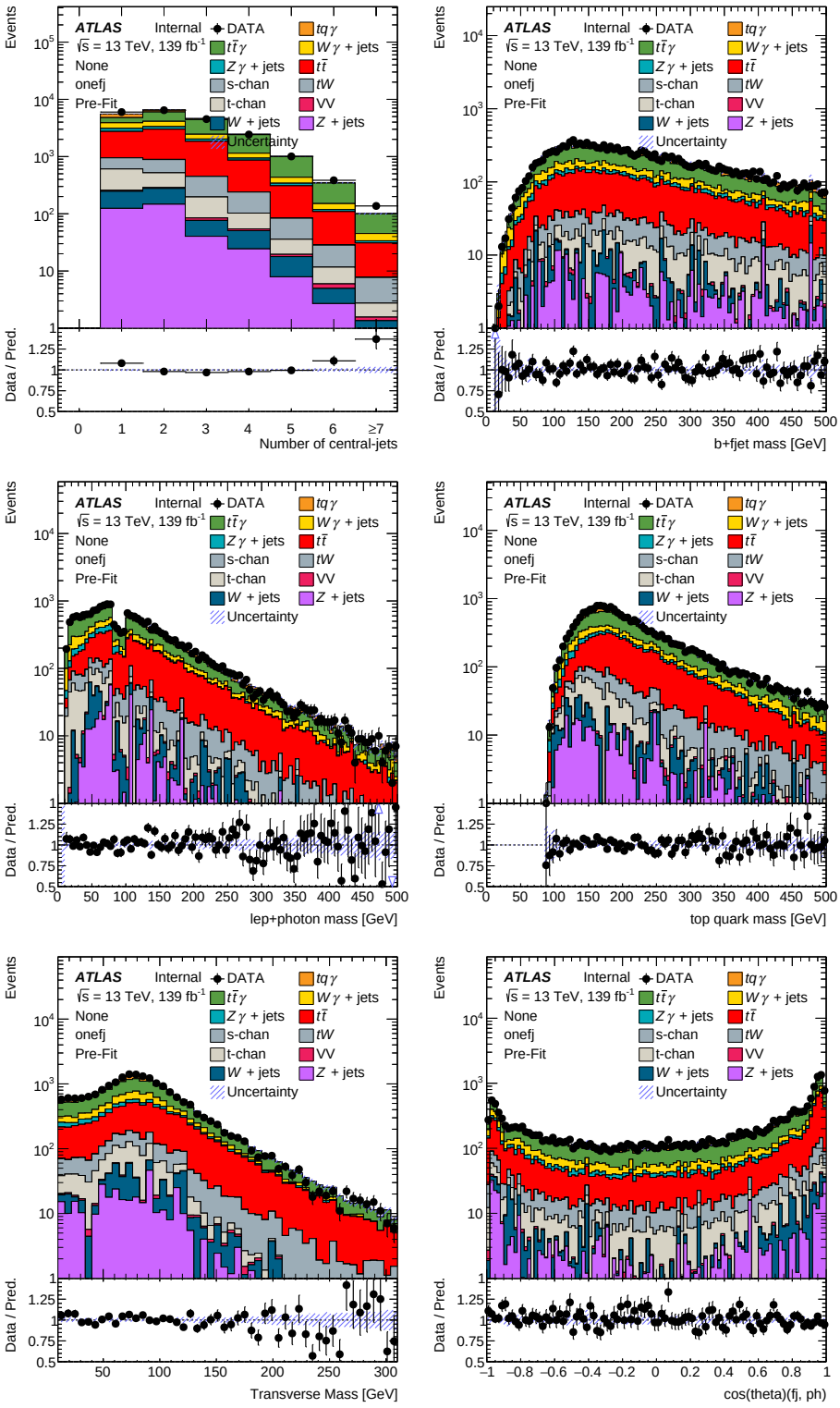

Figure 10.6: Input variable plots for 1-fj category

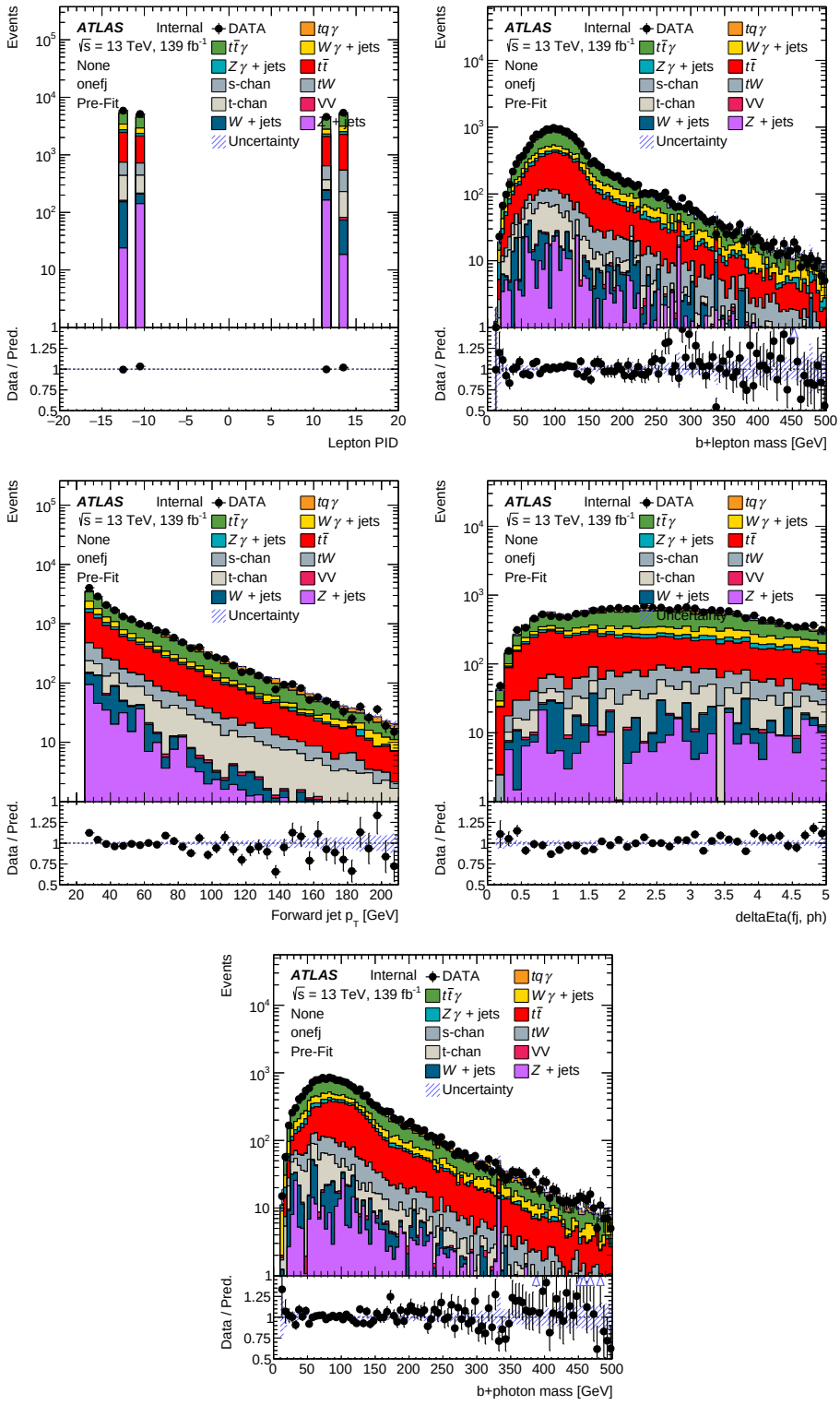

Figure 10.7: Input variable plots for 1-fj category

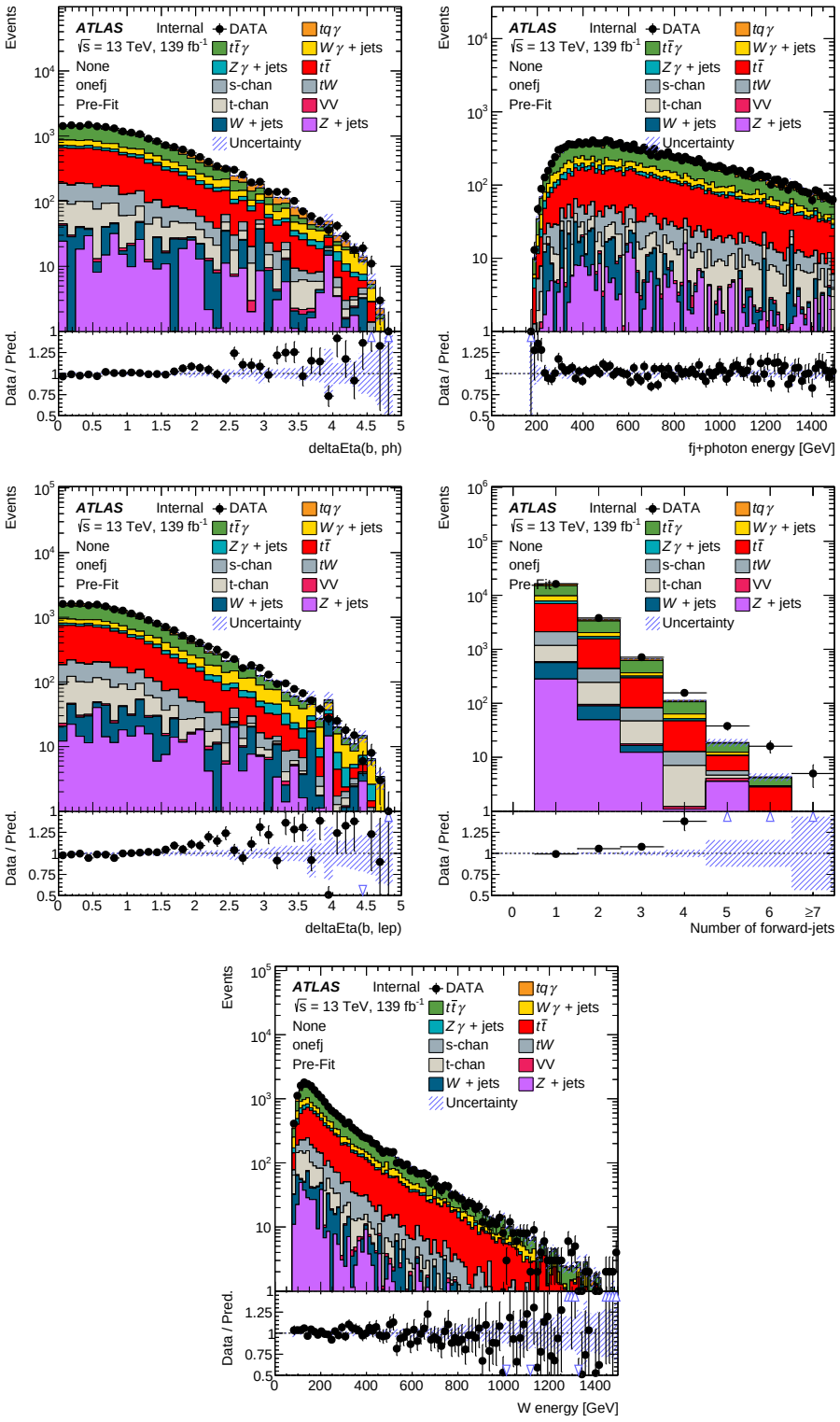

Figure 10.8: Input variable plots for 1-fj category

of the signal sample, the event weights for signal events in the training sample are scaled in order to equalize the sum of weights, so that the loss function considers signal and background events equally.

The NN is trained for 5000 epochs where 10,000 events are considered in each step of an epoch. The value of loss function and the accuracy as a function of number of epochs trained are shown in Figures 10.9 and 10.10 for 0-fj and $\geq$1-fj categories, respectively. After the training, an accuracy of 70 % is achieved in both categories.

10.3.1 Output of the neural networks

The output of the neural networks for 0-fj and $\geq$1-fj categories are shown in Figures 10.11 and 10.12. Signal and background events are normalized to their nominal event weight in these plots.

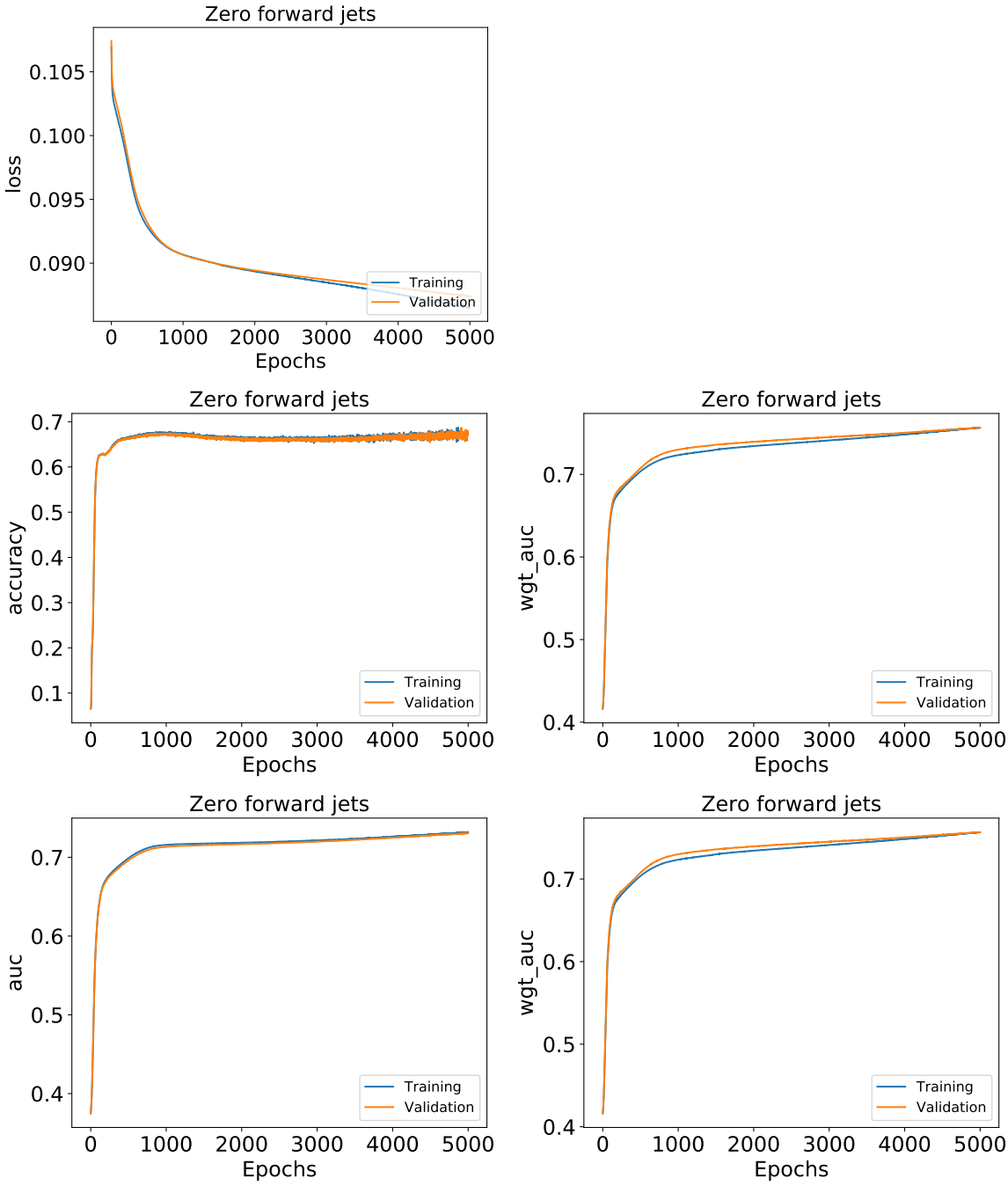

Figure 10.9: Loss function, Accuracy, Weighted Accuracy, AUC and weighted AUC as function of the number of epochs trained for the 0-fj category.

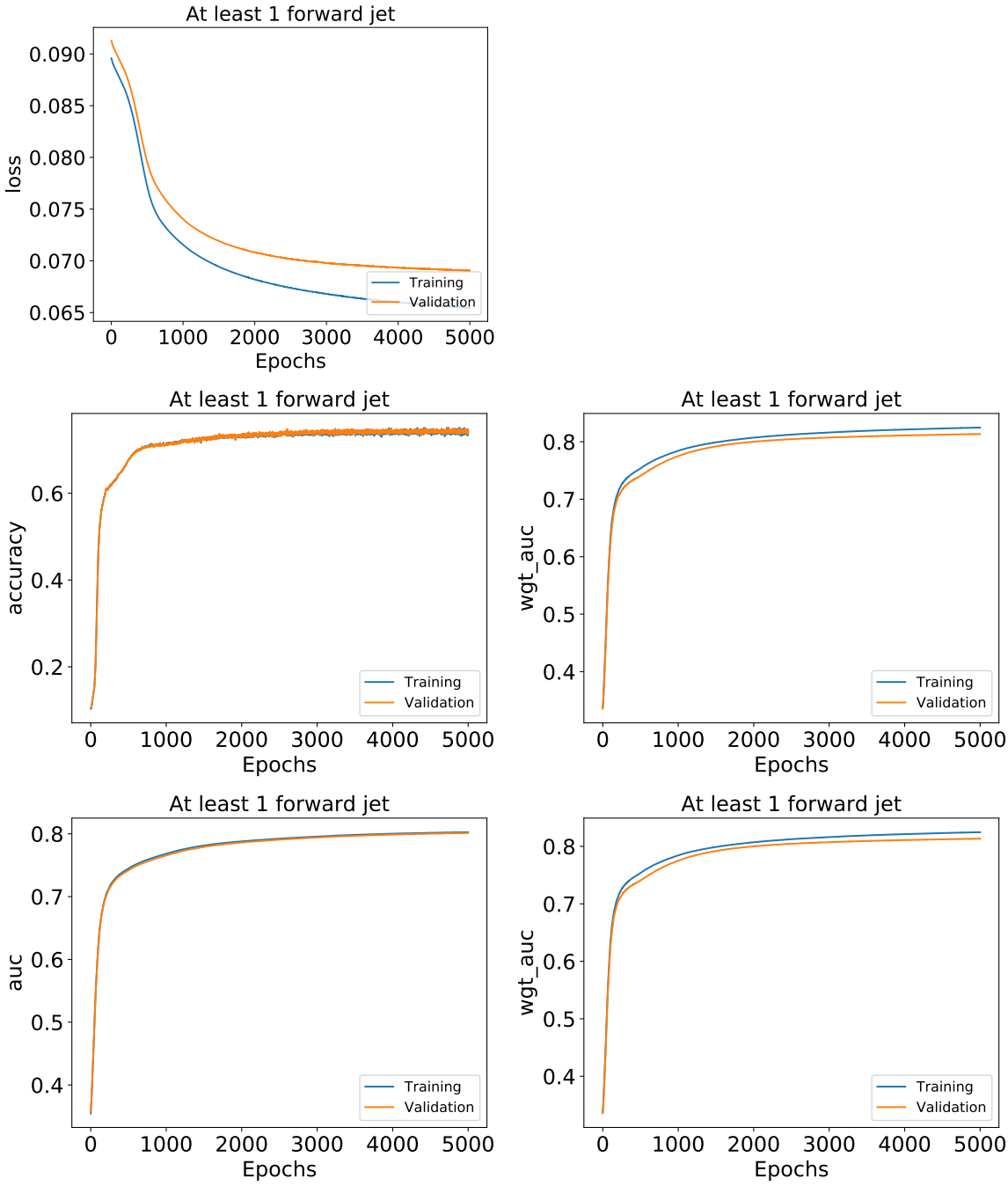

Figure 10.10: Loss function, Accuracy, Weighted Auccracy, AUC, and Weighted AUC as function of the number of epochs trained for the $\geq$1-fj category.

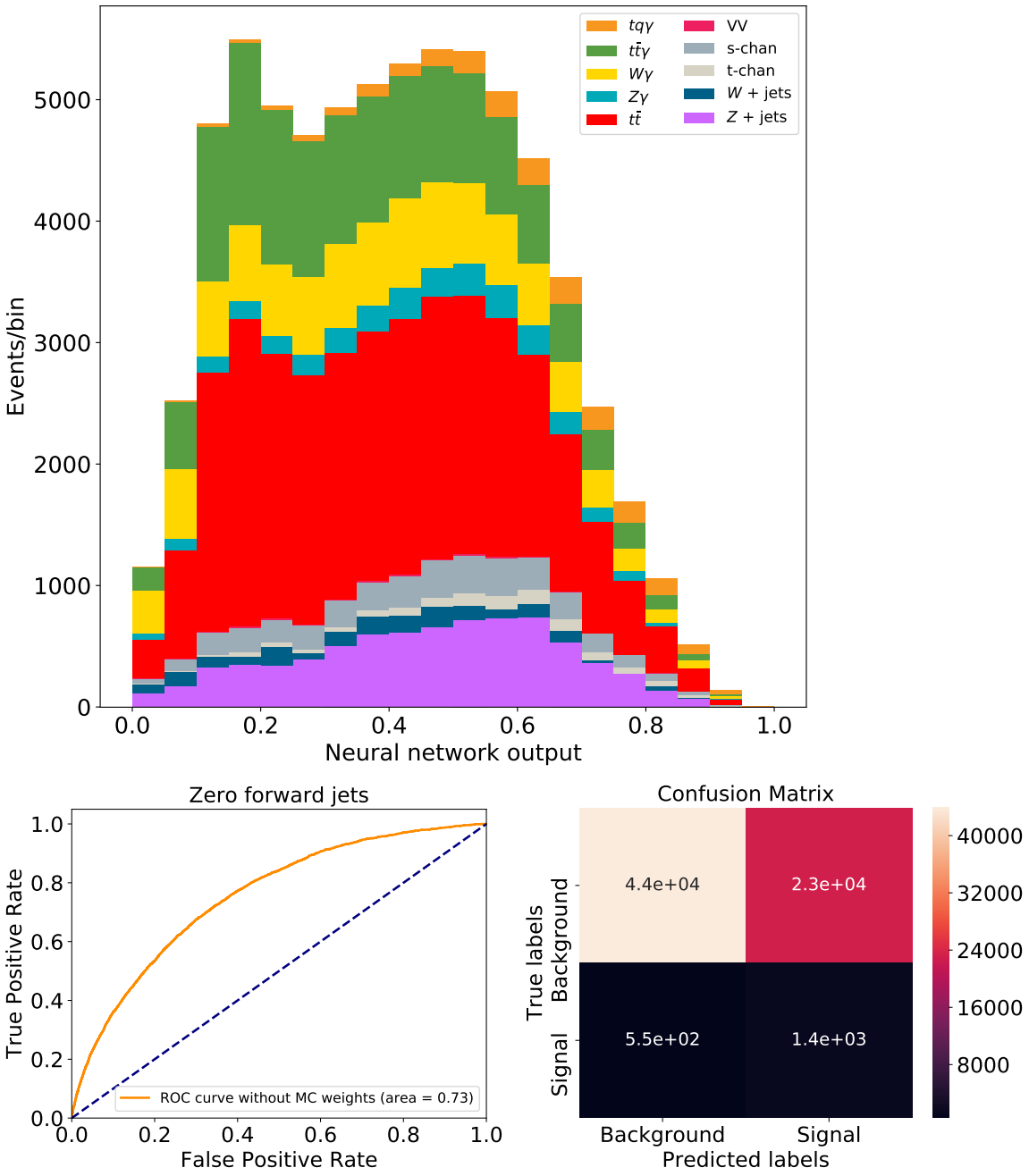

Figure 10.11: NN output, ROC curve and confusion matrix for the neural network of the 0-fj category.

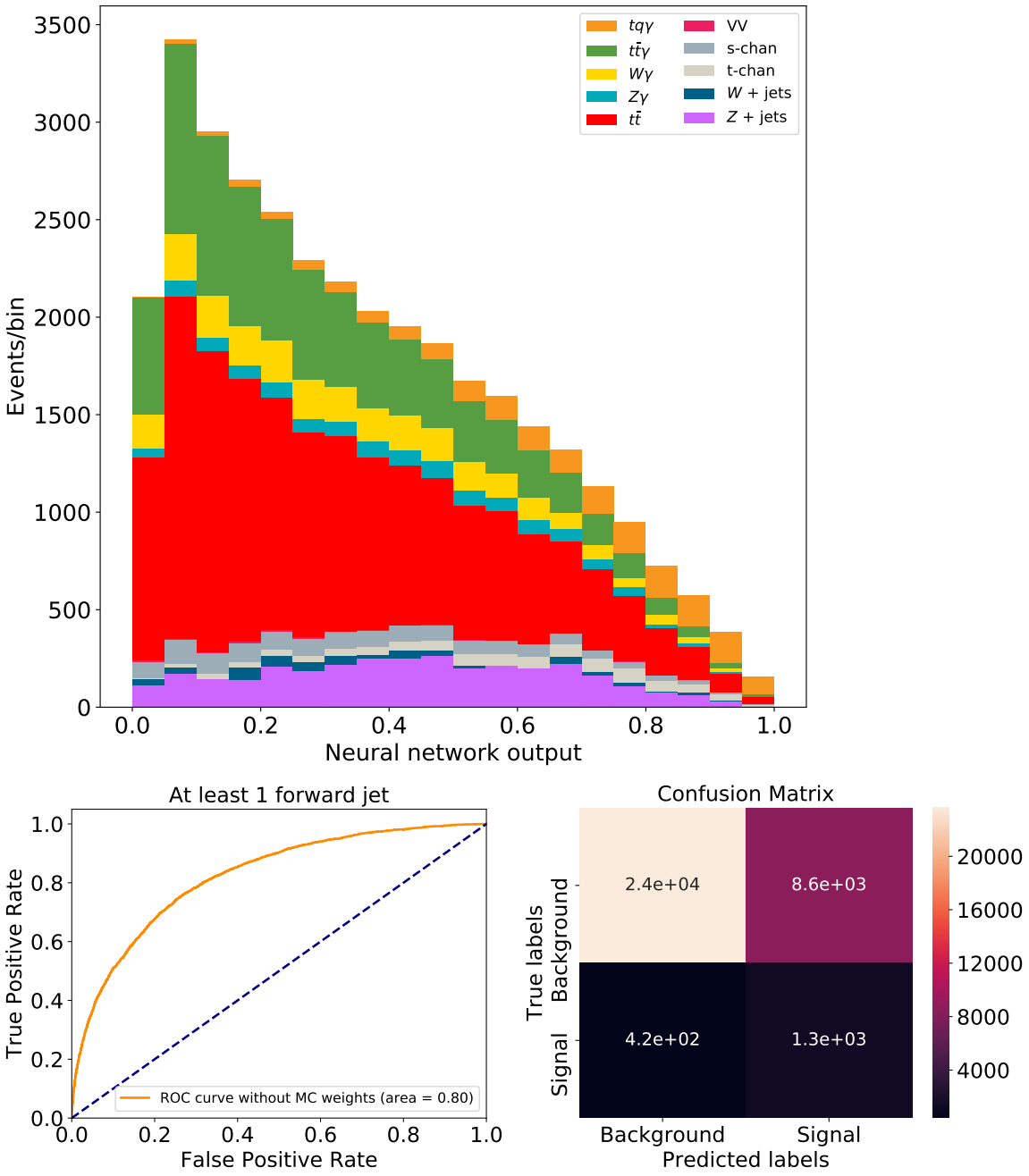

Figure 10.12: NN output, ROC curve and confusion matrix for the neural network of the $\geq$1-fj category.

Chapter Eleven: Systematic Uncertainties

Systematic uncertainties that affect the normalization of signal and background and/or the shape of the neural network discriminant distributions are documented in this chapter. Individual sources of systematic uncertainty are considered uncorrelated with respect to each other. Correlations of a given systematic uncertainty are maintained across all signal and control regions, unless specified otherwise.

These are classified into two categories: Experimental and Theoretical. Section 11.1 describes the experimental systematic uncertainties. Theoretical uncertainties related to the MC modelling are presented in Section 11.2. Tables 11.1 & 11.2 presents a list of all systematic uncertainties considered in this analysis and indicates whether they are taken to be normalization-only, or to affect both shape and normalization.

11.1 Experimental systematic uncertainties

11.1.1 Luminosity

The uncertainty in the combined 2015-18 luminosity is 1.7%. The luminosity uncertainty is applied to all MC samples. To account for the difference in pile-up distributions for data and MC simulations, an uncertainty related to the MC scale factors is applied.

The uncertainty on the integrated luminosity is 1.7%, affecting the overall normalization of all processes estimated from the simulation. It is derived, following a methodology similar to that detailed in Refs. from a preliminary calibration of the luminosity scale using x-y beam-separation scans performed in August 2015 and May 2016.

Systematic uncertainty	Type	Components
Luminosity	N	1
Pile-up reweighting	SN	1
Physics Objects		
Photon	SN	2
Electron	SN	4
EGamma	SN	2
Muon	SN	15
Jet energy scale (JES)	SN	29
Jet energy resolution (JER)	SN	8
Jet vertex tagger (JVT)	SN	1
b-tagging efficiency	SN	45
c-tagging efficiency	SN	20
Light-tagging efficiency	SN	20
Missing p_T	SN	3
Total (Experimental)		152
Data-driven background estimates		
$e \to \gamma$ fakes	N	1
$h \to \gamma$ fakes	N	1
Non-prompt leptons	N	1
Total (Data-driven reducible background)		3

Table 11.1: Sources of experimental systematic uncertainty considered in the analysis. "(N)" means that the uncertainty is taken as normalisation-only for all processes and regions affected. All other uncertainties affect also the shape of the fitted distributions and/or the acceptance in the fit regions. Some of the systematic uncertainties are split into several components, as indicated by the number in the rightmost column.

11.1.2 Leptons

Uncertainties associated with leptons arise from the trigger, reconstruction, identification, and isolation, as well as the lepton momentum scale and resolution. The reconstruction, identification and isolation efficiency of electrons and muons, as well as the efficiency of the trigger used to record the events, differ slightly between data and simulation. Scale factors are derived using tag-and-probe techniques on $Z \to \ell^+\ell^-$ ($\ell = e, \mu$) data simulated samples, and are applied to the simulation to correct for differences. The effect of these uncertainties is propagated as uncertainties to the event weight.

Systematic uncertainty	Type	Components
$tq\gamma$ **modelling**		
μ_R	SN	1
μ_F	SN	1
Parton shower and hadronisation model	SN	1
PDF uncertainty	SN	1
$t\bar{t}\gamma$ **modelling**		
μ_R	SN	1
μ_F	SN	1
Parton shower and hadronisation model	SN	1
PDF uncertainty	SN	1
PYTHIA8 var3c	SN	1
$W\gamma$ **modelling**		
μ_R	SN	1
μ_F	SN	1
PDF uncertainty	SN	1
$Z\gamma$ **modelling**		
μ_R	SN	1
μ_F	SN	1
PDF uncertainty	SN	1
$t\bar{t}$ **modelling**		
μ_R	SN	1
μ_F	SN	1
PDF uncertainty	SN	1
PYTHIA8 var3c	SN	1
Other background modelling		
Single-top Cross section	N	1
Z+jets Cross section	N	1
W+jets Cross section	N	1
Diboson Cross section	N	1
Total (Signal and background modelling)		23
Total (Exp.+Theory+Data-driven)		178

Table 11.2: Sources of theoretical systematic uncertainty considered in the analysis. "(N)" means that the uncertainty is taken as normalisation-only for all processes and regions affected. All other uncertainties affect also the shape of the fitted distributions and/or the acceptance in the fit regions. Some of the systematic uncertainties are split into several components, as indicated by the number in the rightmost column.

Additional sources of uncertainty originate from the corrections applied to adjust the lepton momentum scale and resolution in the simulation to match those in data, measured using reconstructed distributions of the $Z \to \ell^+\ell^-$ and $J\psi \to \ell^+\ell^-$ masses, as well as the measured E/p in $W \to e\nu$ events, where E and p are the electron energy and momentum, as measured by the calorimeter and the tracker respectively. To evaluate the effect of momentum scale uncertainties, the event selection is redone with the lepton momentum varied by $\pm 1\sigma$. For the momentum resolution uncertainties the event selection is redone with the lepton momentum smeared.

11.1.3 Photons

Uncertainties associated with photons arise from the identification and isolation procedures. The scale factor for the photon ID efficiency is derived from three measurements: he radiative Z boson method using a sample enriched in events with radiative Z boson decays, the electron extrapolation technique using a sample enriched in $Z \to ee$ events where the similarity between electrons and photons in the detector is exploited, and the matrix method using a sample enriched with isolated, high-p_T photons and exploiting that the narrow-strip variables are only weakly correlated to the isolation. The scale factor is computed as the ratio of the efficiency measured in data and that determined in simulation. The sets of scale factors of all measurements are combined into one single set that is applied to simulation to correct for deviations between efficiencies measured in data and found in simulation. The scale factors for photon isolation are measured as described in Ref. [88]. The scale factors are varied up and down by one standard deviation.

11.1.4 Jets and missing transverse momentum

Uncertainties associated with jets in principle arise from the efficiency of jet identification based on the JVT variable, as well as the jet energy scale (JES) and resolution. Differences between data and MC on the JVT efficiency for hard-scatter jets are corrected via dedicated scale factors measured in Z+jets events. Uncertainties on the JVT scale factors include the statistical uncertainty and 30% uncertainty on the estimation of the residual contamination from pile-up jets after pile-up suppression.

These two uncertainties are combined into a single uncertainty that is varied up and down.

The jet energy scale and its uncertainty were derived by combining information from test-beam data, LHC collision data and simulation.

The E_T^{miss} reconstruction is affected by uncertainties associated with leptons and jet energy scales and resolutions, which are propagated to E_T^{miss} and thus are included under the corresponding per-object uncertainty category. Additional small uncertainties associated with the modelling of the underlying event, in particular its impact on the p_T scale and resolution of unclustered energy, are also taken into account.

11.1.5 Flavour-tagging

Uncertainties on the efficiencies of b-tagging are evaluated from auxiliary measurements in data in separate control regions enriched in either b-,c- or light-flavoured jets. A set of 45 independent uncertainty sources are considered for b-jets and 20 sources are considered for c-jets, while 20 components for light-flavour jets are considered.

11.2 Theoretical systematic uncertainties

11.2.1 $tq\gamma$ modelling

All theoretical systematic variation samples for $tq\gamma$ simulation are normalized to the cross-section obtained from the nominal prediction to avoid dependencies on the MC-generated phase space. However, differences in rate and shape might still occur due to differences in reconstruction efficiency and migration effects.

Uncertainties due to 7-point QCD scale variations are obtained by varying renormalization scale (μ_R) and factorization scale (μ_F) separately and together up and down by a factor of 2 with respect to the nominal sample value. No smoothing and symmetrisation methods are applied to the variation. These variations are shown in

Figure.

The uncertainty due to the choice of parton shower and hadronisation model ($tq\gamma$ PS model) is estimated by comparing the $tq\gamma$ nominal sample, produced with MG5+Pythia8, with MG5+Herwig7 sample.

The uncertainty due to the choice of PDF set is evaluated by performing fits to an ensemble of 100 "replica" pdfsets (reduced set) provided by the NNPDF. Uncertainty is determined by the standard deviation of all the replicas.

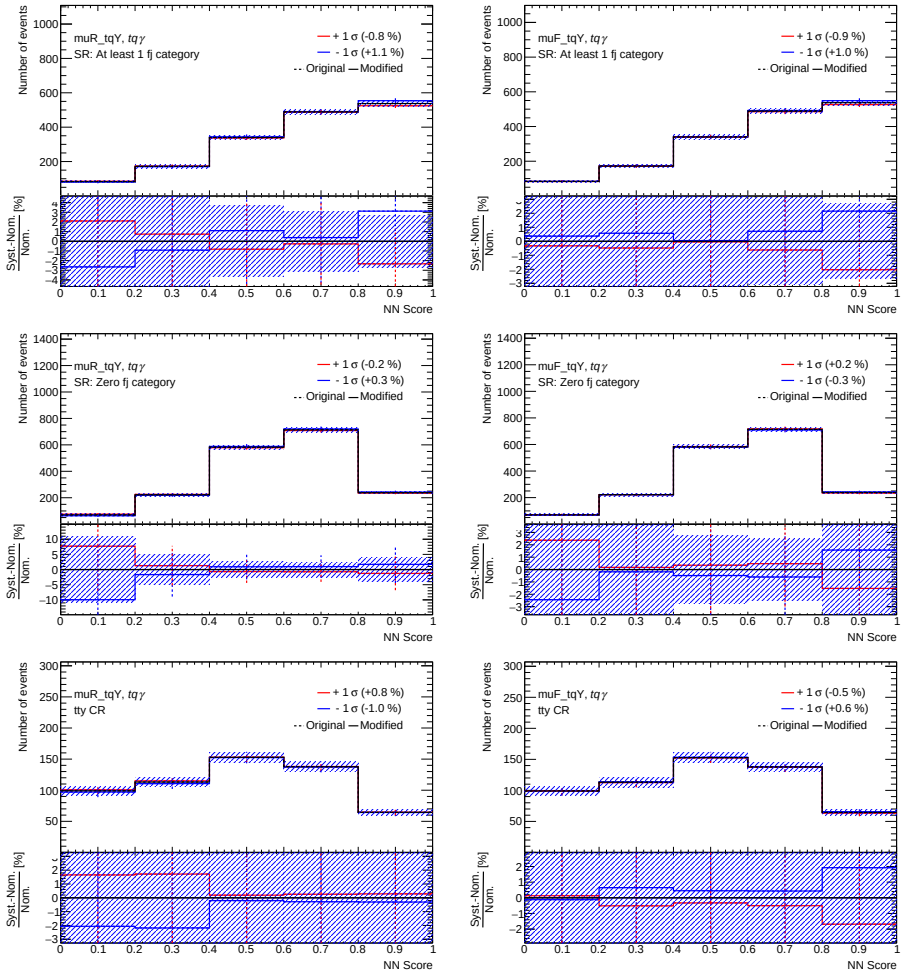

Figure 11.1: Impact of renormalization and factorization scale variations of $tq\gamma$ sample on the neural network discriminants for 0-fj, $\geq$ 1-fj and $t\bar{t}\gamma$ control regions.

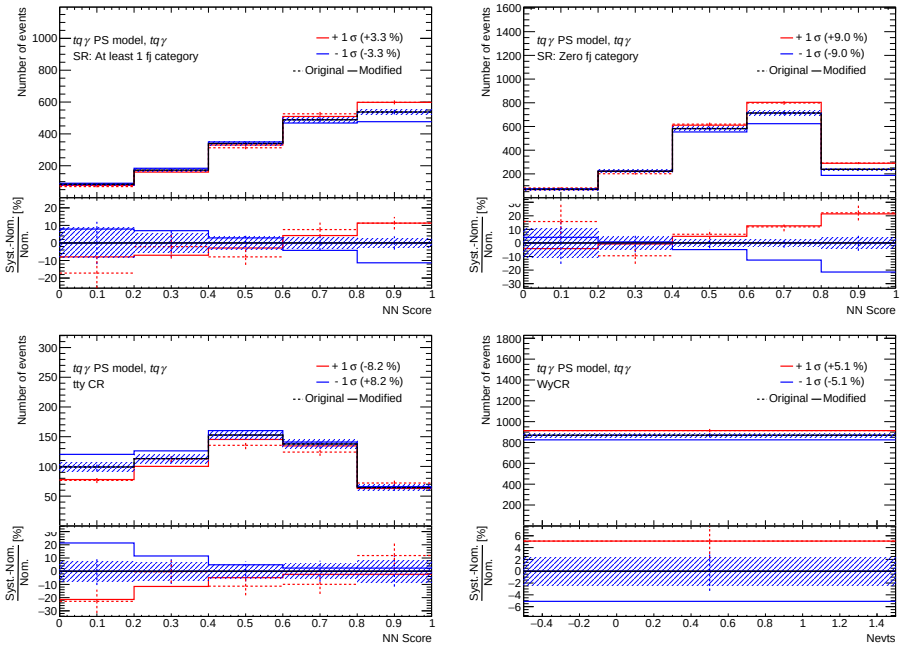

Figure 11.2: Impact of $tq\gamma$ parton shower model uncertainty on the neural network discriminants for 0-fj, $\geq$ 1-fj, $t\bar{t}\gamma$ and $W\gamma$ control regions.

11.2.2 $t\bar{t}\gamma$ modelling

All theoretical systematic variation samples for $tt\gamma$ simulation are normalized to the cross-section obtained from the nominal prediction to avoid dependencies on the MC-generated phase space. However, differences in rate and shape might still occur due to differences in reconstruction efficiency and migration effects.

Uncertainties due to 7-point QCD scale variations are obtained by varying renormalization scale (μ_R) and factorization scale (μ_F) separately and together up and down by a factor of 2 with respect to the nominal sample value. No smoothing and symmetrisation methods are applied to the variation. These variations are shown in Figure.

The uncertainty due to the choice of parton shower and hadronisation model ($tt\gamma$ PS model) is estimated by comparing the $t\bar{t}\gamma$ nominal sample, produced with MG5+Pythia8, with MG5+Herwig7 sample. Same LHE events are used for both

PYTHIA8 and HERWIG7 samples.

The uncertainty due to the choice of PDF set is evaluated by performing fits to an ensemble of 100 "replica" pdfsets (reduced set) provided by the NNPDF. Uncertainty is determined by the standard deviation of all the replicas.

The uncertainty due to ISR/FSR modelling is estimated by varying *var3c* parameter of A14 eigenset to low and high radiation scenarios. Dedicated $t\bar{t}\gamma$ AFII samples produced for this purpose are used.

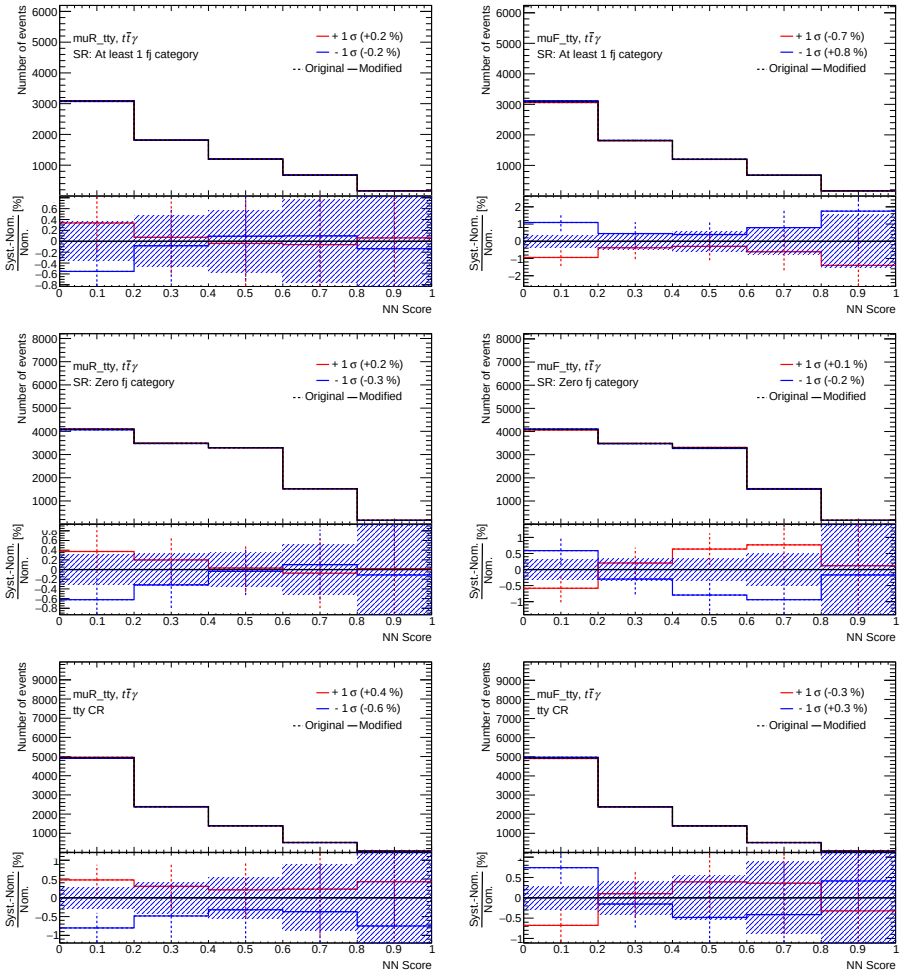

Figure 11.3: Impact of renormalization and factorization scale variations of $t\bar{t}\gamma$ sample on the neural network discriminants for 0-fj, $\geq$ 1-fj and $t\bar{t}\gamma$ control regions.

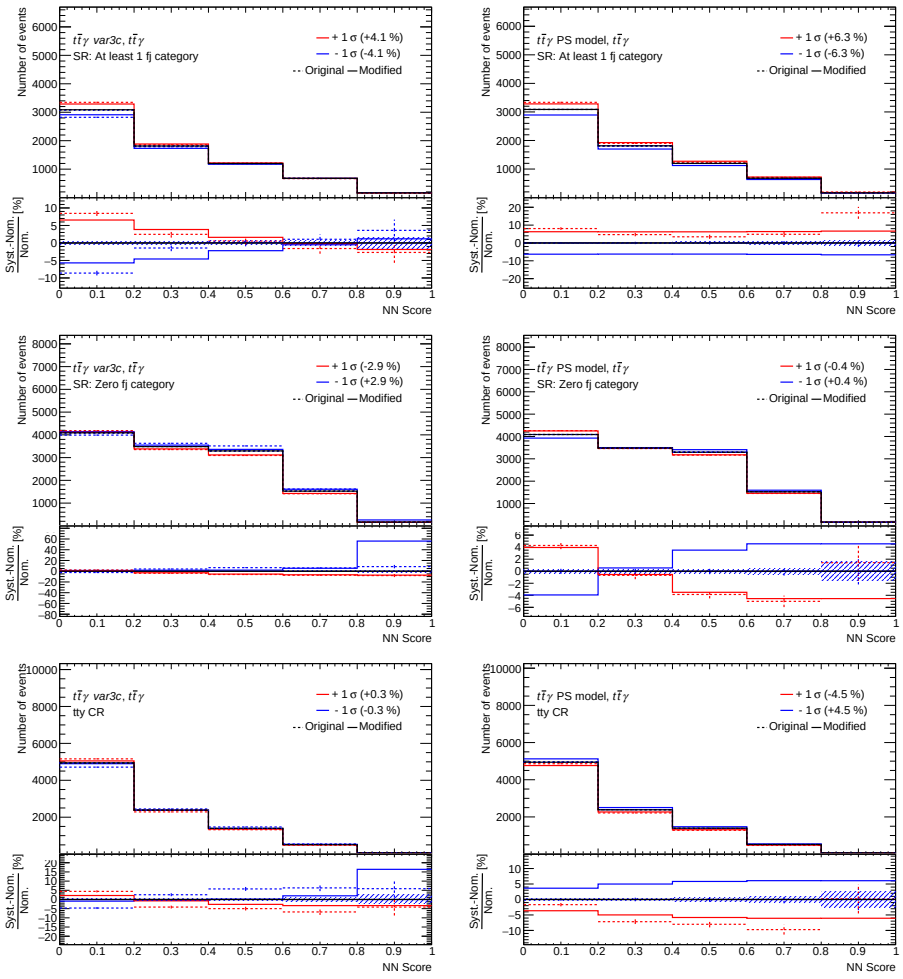

Figure 11.4: Impact of var3c and parton shower variations of $tq\gamma$ sample on the neural network discriminants for 0-fj, $\geq$ 1-fj and $t\bar{t}\gamma$ control regions.

11.2.3 $W\gamma$ and $Z\gamma$ modelling

For $W\gamma$ and $Z\gamma$ samples, 7-point QCD scale variations and PDF variation uncertainties are included.

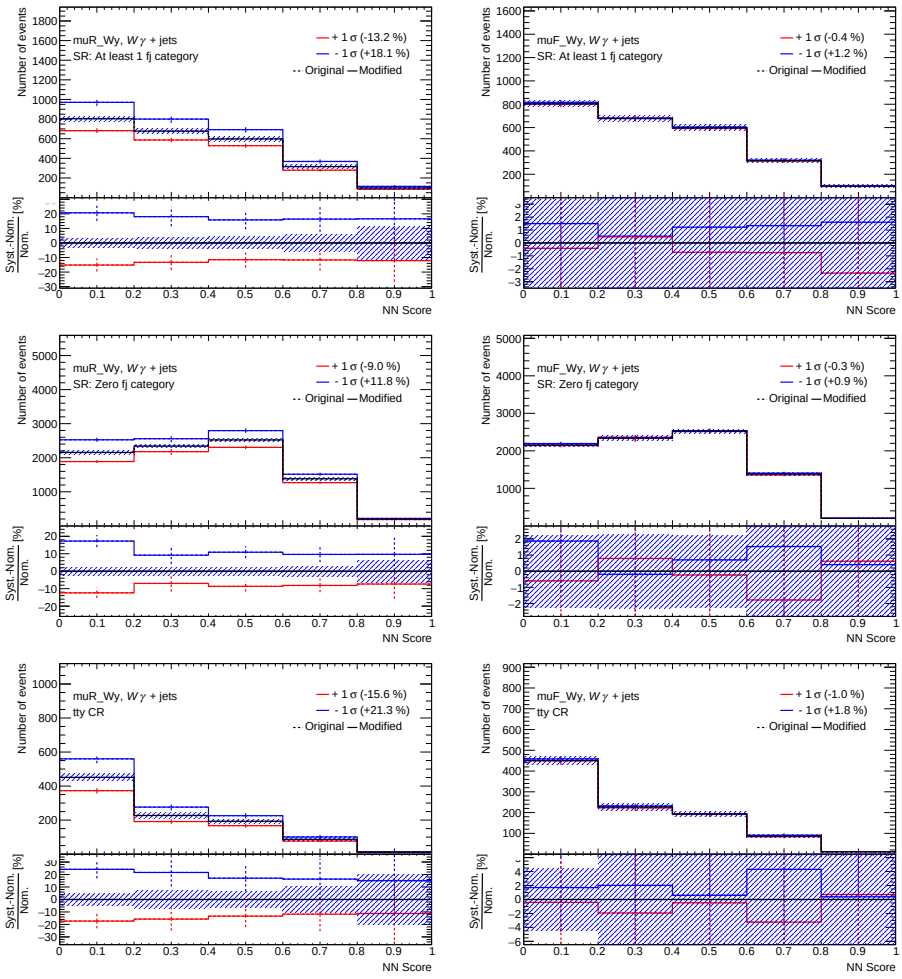

Figure 11.5: Impact of renormalization and factorization scale variations of $W\gamma$ sample on the neural network discriminants for 0-fj, $\geq$ 1-fj and $t\bar{t}\gamma$ control regions.

11.2.4 $t\bar{t}$ modelling

For $t\bar{t}$ sample, 7-point QCD scale variations, var3c variation and PDF variation uncertainties are included.

11.2.5 Modelling of other backgrounds

Uncertainties on the total cross-section are included for minor backgrounds: single-top production, Diboson, Z+jets and W+jets

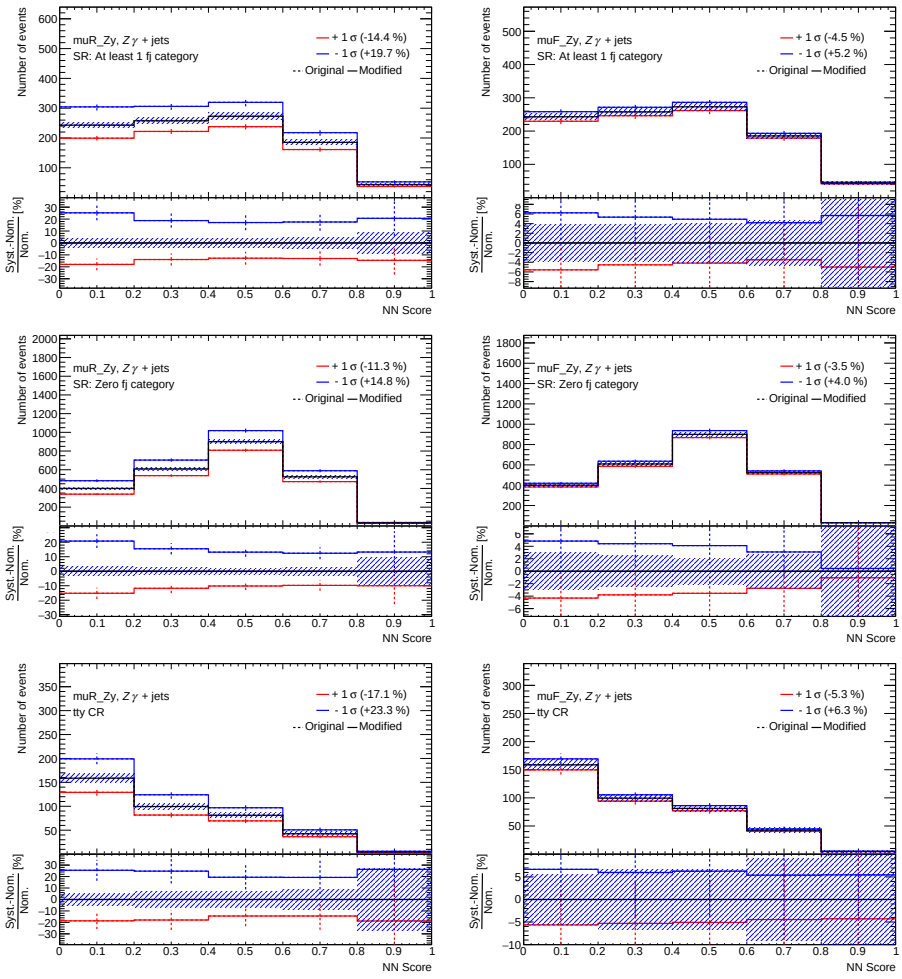

Figure 11.6: Impact of renormalization and factorization scale variations of $Z\gamma$ sample on the neural network discriminants for 0-fj, $\geq$ 1-fj and $t\bar{t}\gamma$ control regions.

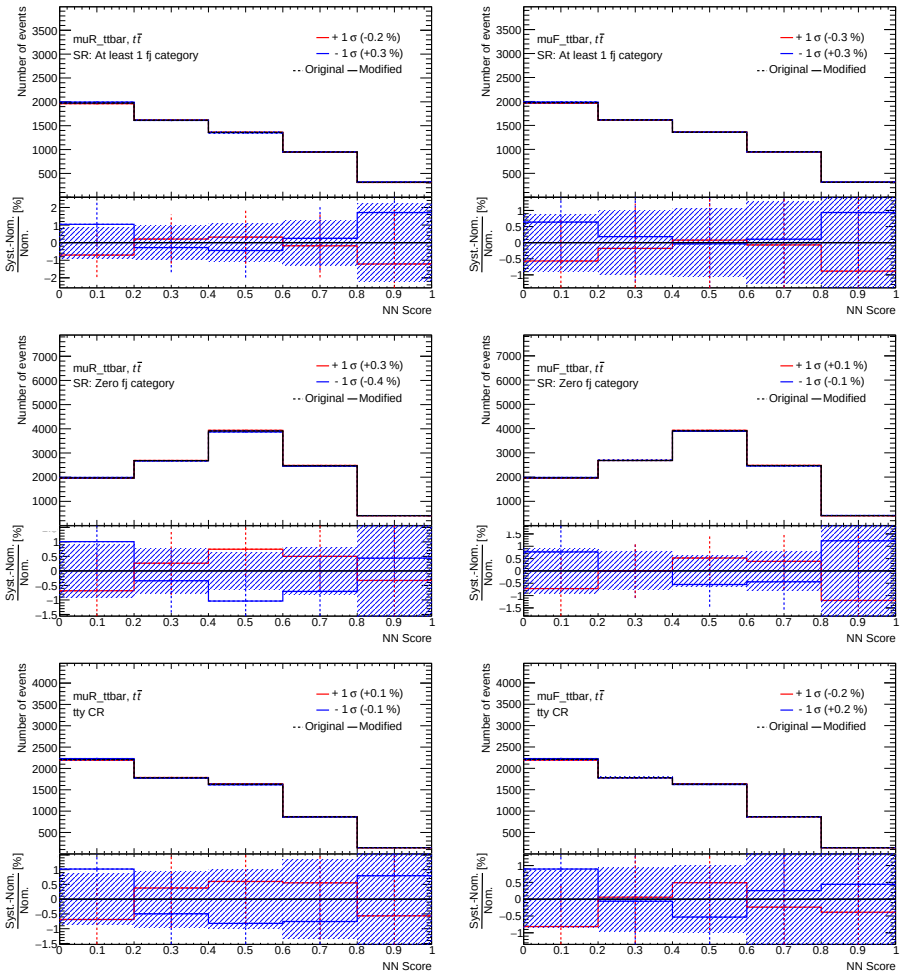

Figure 11.7: Impact of renormalization and factorization scale variations of $t\bar{t}$ sample on the neural network discriminants for 0-fj, $\geq$ 1-fj and $t\bar{t}\gamma$ control regions.

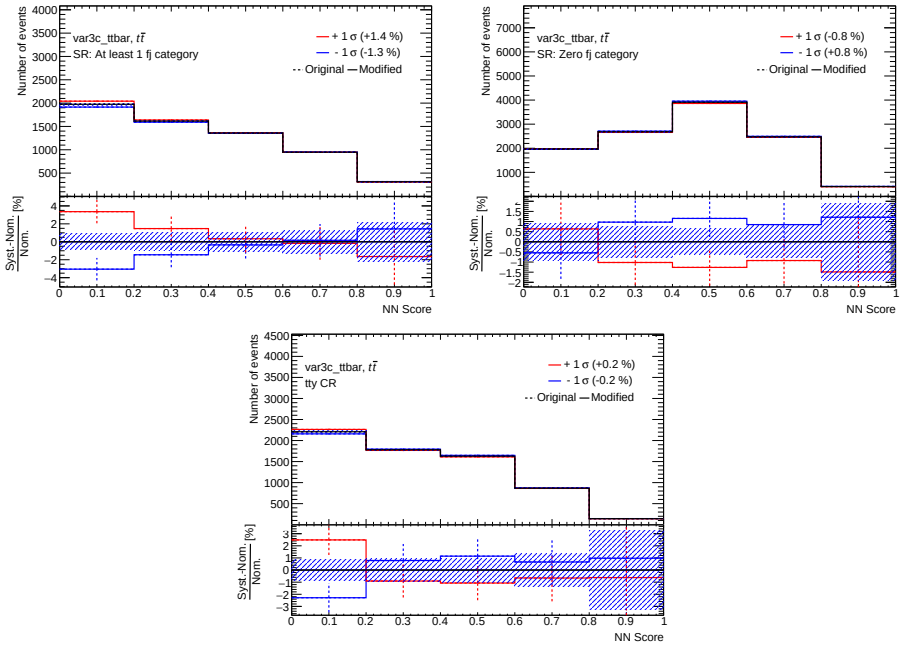

Figure 11.8: Impact of var3c variations of $t\bar{t}$ sample on the neural network discriminants for 0-fj, $\geq$ 1-fj and $t\bar{t}\gamma$ control regions.

Chapter Twelve: Statistical Analysis

12.1 Asimov fit results

A simultaneous profile-likelihood fit to Asimov dataset produced with $\mu_{tq\gamma} = \mu_{t\bar{t}\gamma} = \mu_{W\gamma} = 1.0$ is performed in the signal regions, $t\bar{t}\gamma$ CR and $W\gamma$ CR. In the signal regions and $t\bar{t}\gamma$ CR, the output of the neural network is used as the discriminant. In $W\gamma$ CR, a single bin fit, with number of events as the discrimination variable, is performed because some input variables for the neural network are not available in this region. Normalization factors for signal ($\mu_{tq\gamma}$), $t\bar{t}\gamma$ samples ($\mu_{t\bar{t}\gamma}$) and $W\gamma$ samples ($\mu_{W\gamma}$) are freely floated during the fit.

In order to speed up the fit, a pruning algorithm is applied before the fit to remove systematic uncertainties that have a very small effect. This algorithm is applied per sample and per region. The normalization of a systematic uncertainty is dropped if it has $\leq 1\%$ impact on the normalization. The shape of a systematic uncertainty is dropped if the impact in all bins of the discriminant is $\leq 1\%$.

Pre-fit and Post-fit distributions of the neural network output for all regions are shown in Figure 12.1 and 12.2. Pre-fit and post-fit values for all nuisance parameters are illustrated in Figure 12.4. As can be seen from this plot, a number of nuisance parameters related to $tq\gamma$, $t\bar{t}\gamma$ and $W\gamma$ modelling ($tq\gamma$ PS model, $t\bar{t}\gamma$ var3c, $t\bar{t}\gamma$ PS model, $W\gamma$ μ_R, $W\gamma$ μ_F), are overconstrained. This is expected as the fit has sufficient statistics for these processes in the signal and control regions that the fit is able to rule out the 1 sigma variations. The correlation matrix for the nuisance parameters having at least one correlation coefficient above 10% is shown in Figure 12.3. In general correlations are small, although there are several nuisance parameters correlated at the level of 40-70% which is not unexpected as several of them have large uncertainties that cause similar changes in the background prediction.

The norm factors and the γ-factors which describe the per-bin statistical uncertainties are shown in Figure 12.6. The expected best-fit value of $\mu_{tq\gamma}$ is $1.0\ ^{+0.14}_{-0.14} =$

$1.0\ ^{+0.05}_{-0.05}$ (stat.) $^{+0.13}_{-0.13}$ (syst.). The expected significance with respect to no-$tq\gamma$ hypothesis is 6.5 σ.

Ranking of nuisance parameters based on the impact on $\mu_{tq\gamma}$ is presented in Figure 12.5. The largest impact on the signal strength comes from the $tq\gamma$ parton shower model variation uncertainty. As can be observed from Figure 11.2, this is mainly because the NP corresponding to the $tq\gamma$ PS model changes the signal yield approximately by 10% in the highest S/B bin.

12.2 Background only fit to data

A simultaneous profile-likelihood fit to data is performed for bins with S/B $< 10\%$ in the signal regions, $t\bar{t}\gamma$ CR and $W\gamma$ CR. In the signal regions and $t\bar{t}\gamma$ CR, the output of the neural network is used as the discriminant. In $W\gamma$ CR, a single bin fit, with number of events as the discrimination variable, is performed because some input variables for the neural network are not available in this region. Normalization factors for signal ($\mu_{tq\gamma}$) is fixed at 1.0. Normalization for $t\bar{t}\gamma$ samples ($\mu_{t\bar{t}\gamma}$) and $W\gamma$ samples ($\mu_{W\gamma}$) are freely floated during the fit.

In order to speed up the fit, a pruning algorithm is applied before the fit to remove systematic uncertainties that have a very small effect. This algorithm is applied per sample and per region. The normalization of a systematic uncertainty is dropped if it has $\leq 1\%$ impact on the normalization. The shape of a systematic uncertainty is dropped if the impact in all bins of the discriminant is $\leq 1\%$.

Pre-fit and Post-fit distributions of the neural network output for all regions are shown in Figure 12.7 and 12.8. Pre-fit and post-fit values for all nuisance parameters are illustrated in Figure 12.10. As can be seen from the pull plot, a number of nuisance parameters related to $tq\gamma$, $t\bar{t}\gamma$ and $W\gamma$ modelling ($tq\gamma$ PS model, $t\bar{t}\gamma$ var3c, $t\bar{t}\gamma$ PS model, $W\gamma$ μ_R, $W\gamma$ μ_F), are overconstrained. This is expected as the fit has sufficient statistics for these processes in the signal and control regions that the fit is able to rule out the 1 sigma variations. The correlation matrix for

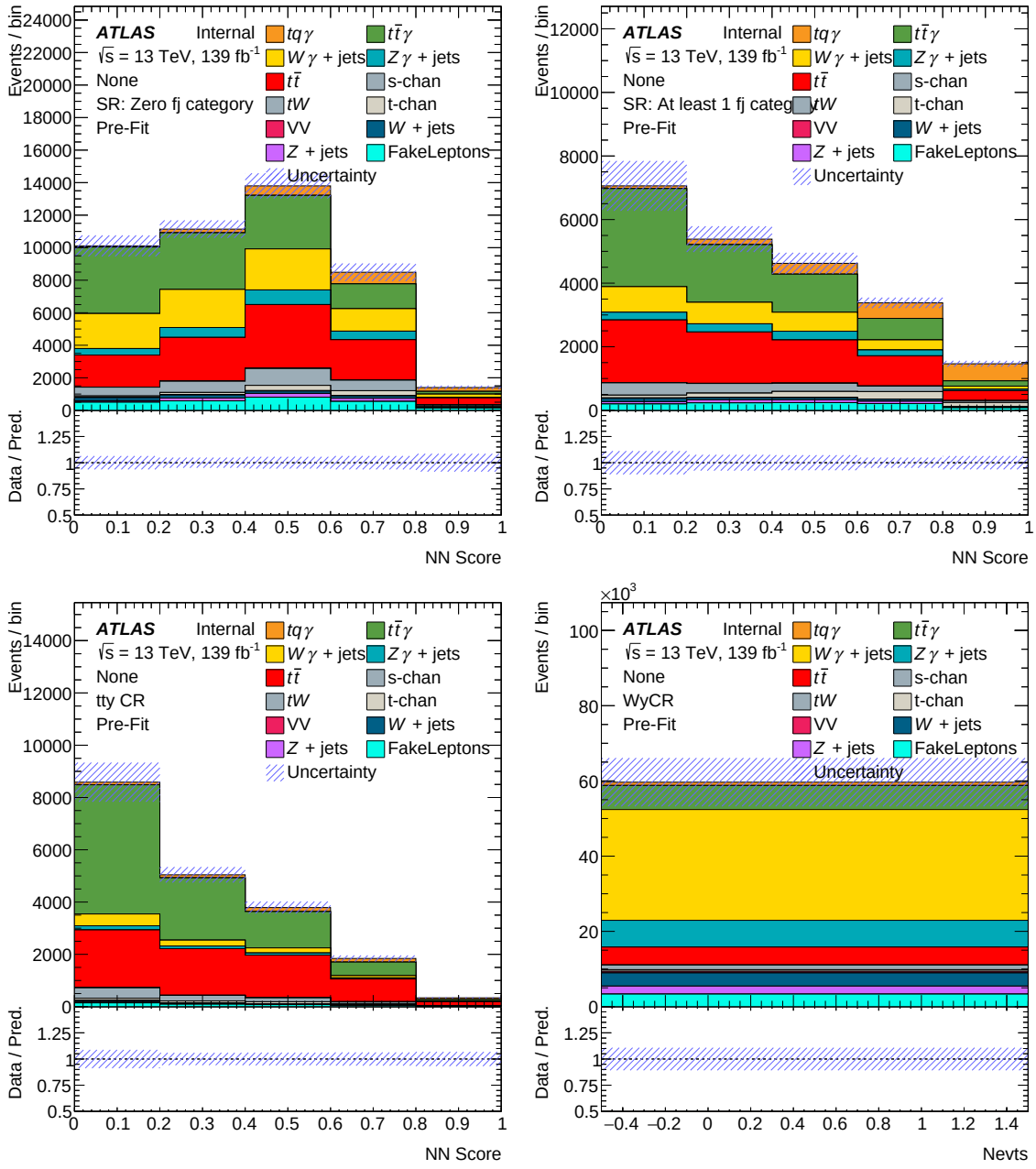

Figure 12.1: Pre-fit distributions of the neural network output with Asimov data for all regions used in the fit.

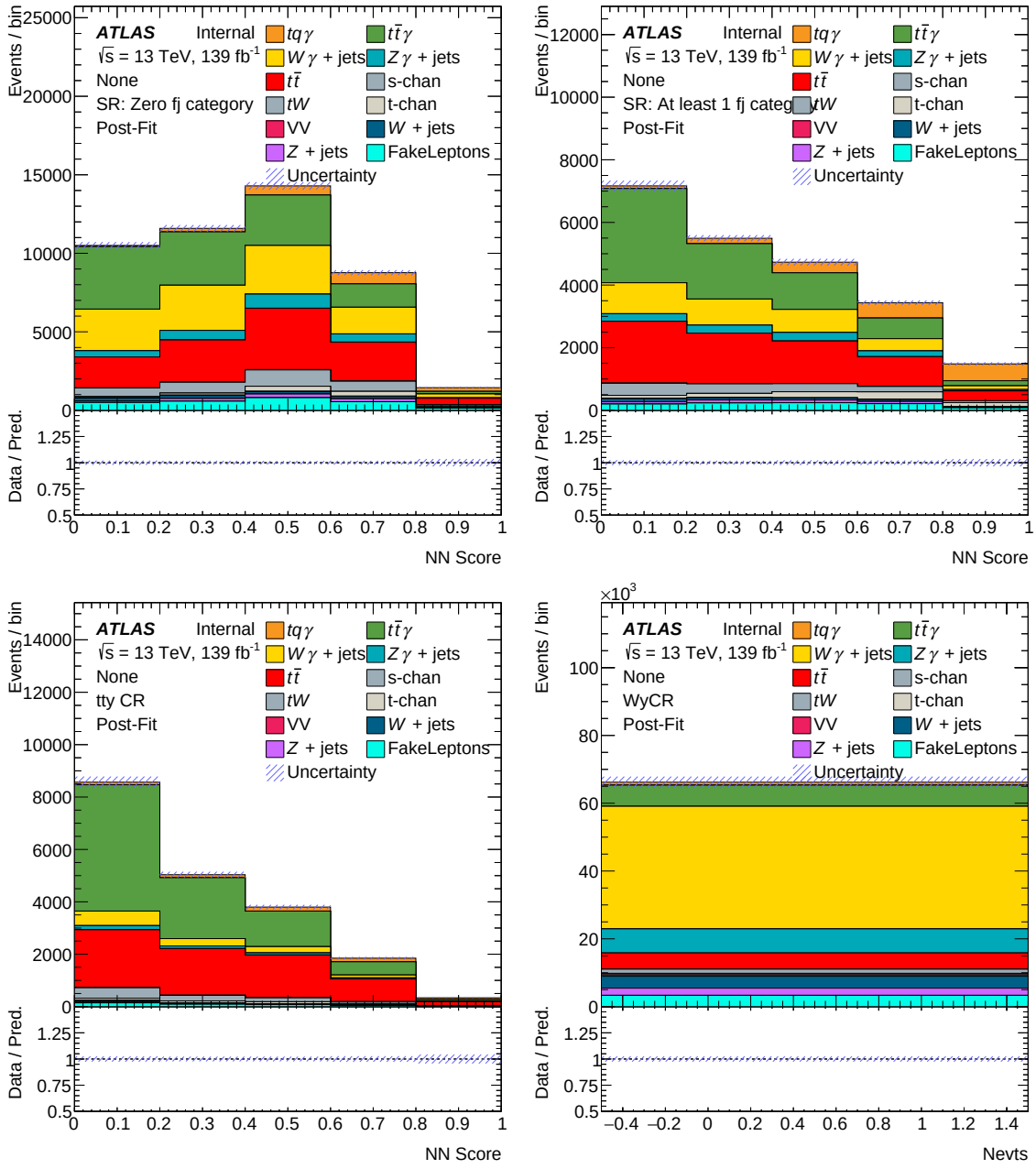

Figure 12.2: Post-fit distributions of the neural network output with Asimov data for all regions used in the fit.

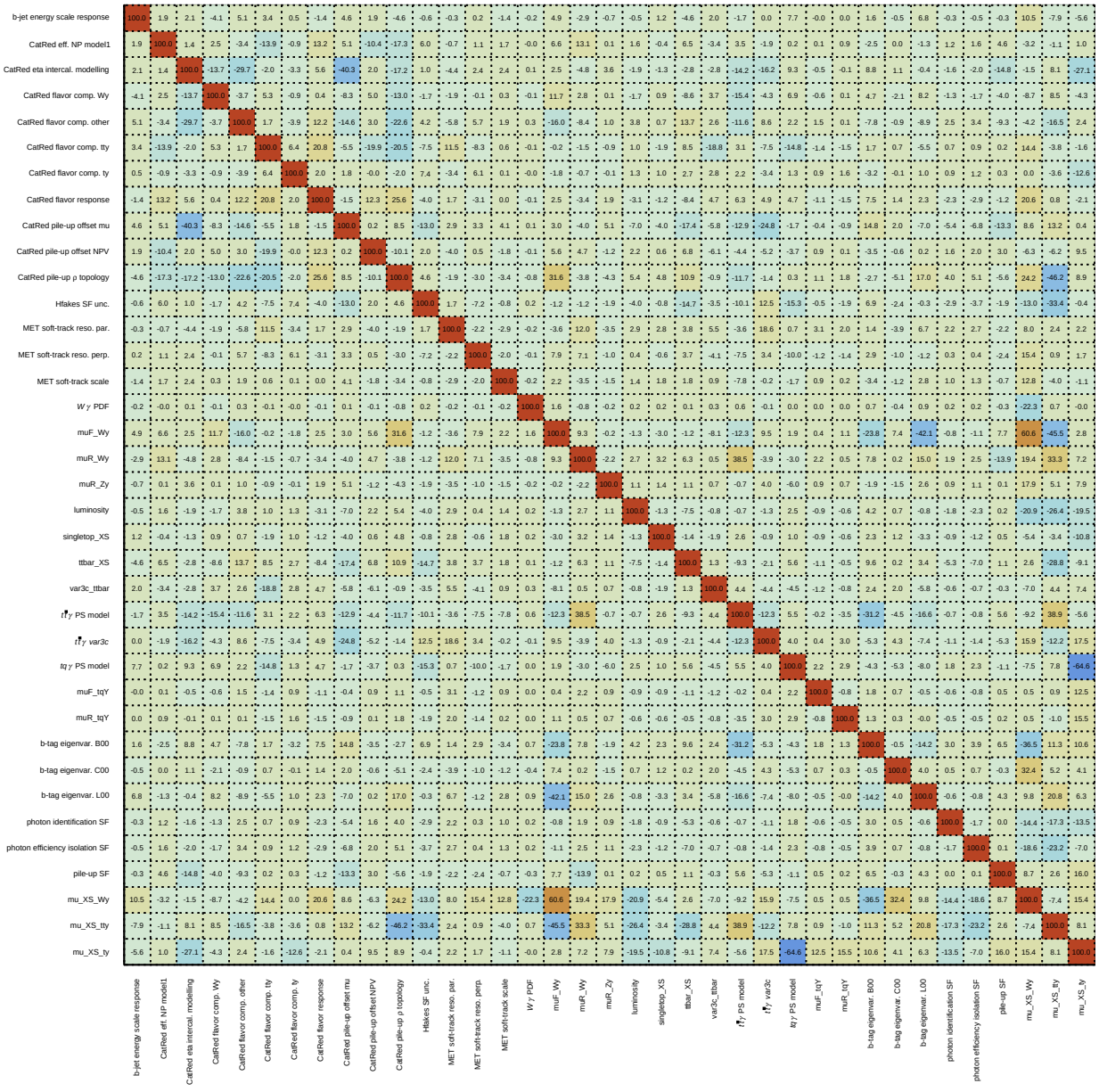

Figure 12.3: Correlation matrix of the nuisance parameters that are included in the Asimov fit.

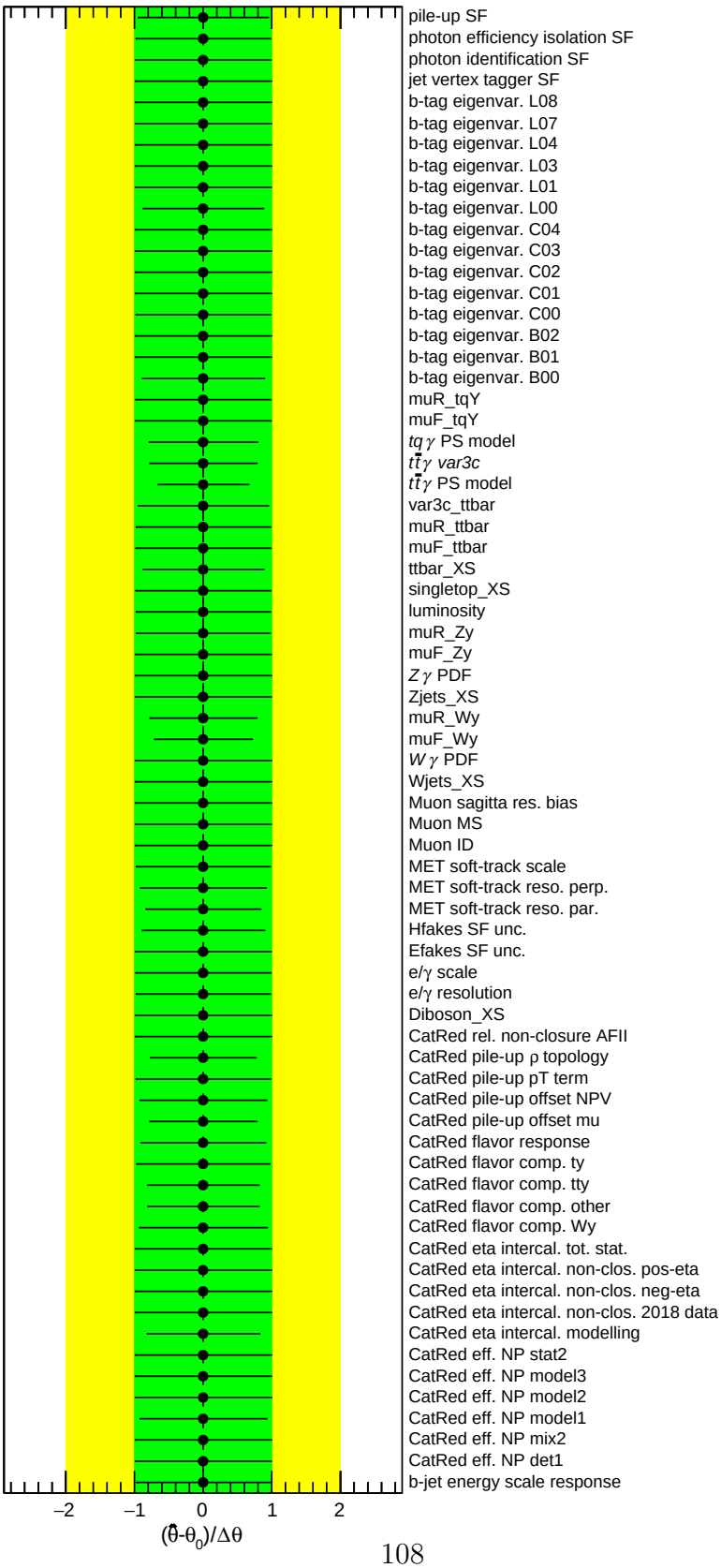

Figure 12.4: Pre- and post-fit values of the nuisance parameters considered in the Asimov fit

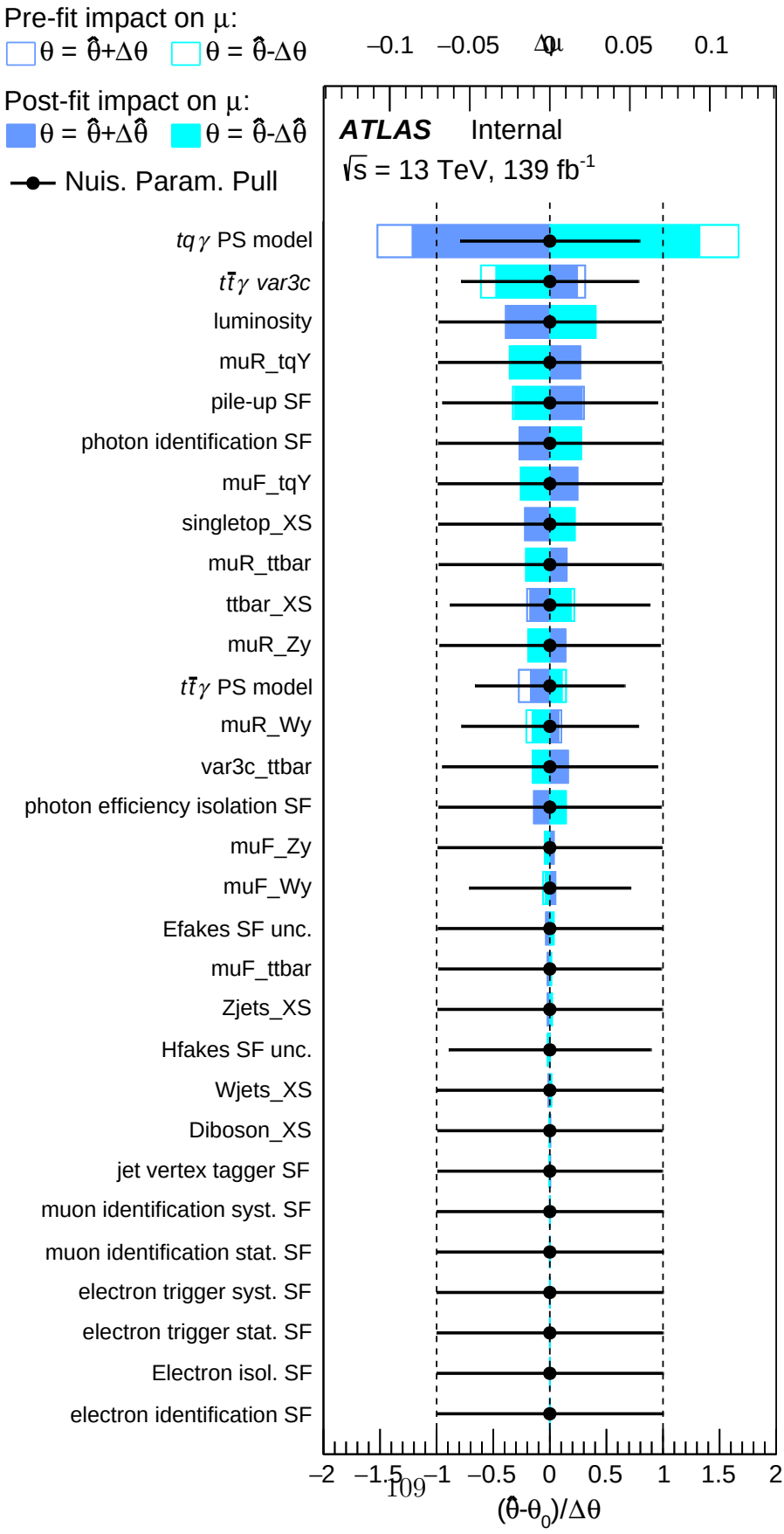

Figure 12.5: Ranking of NPs based on the impact on $\mu_{tq\gamma}$ for Asimov fit

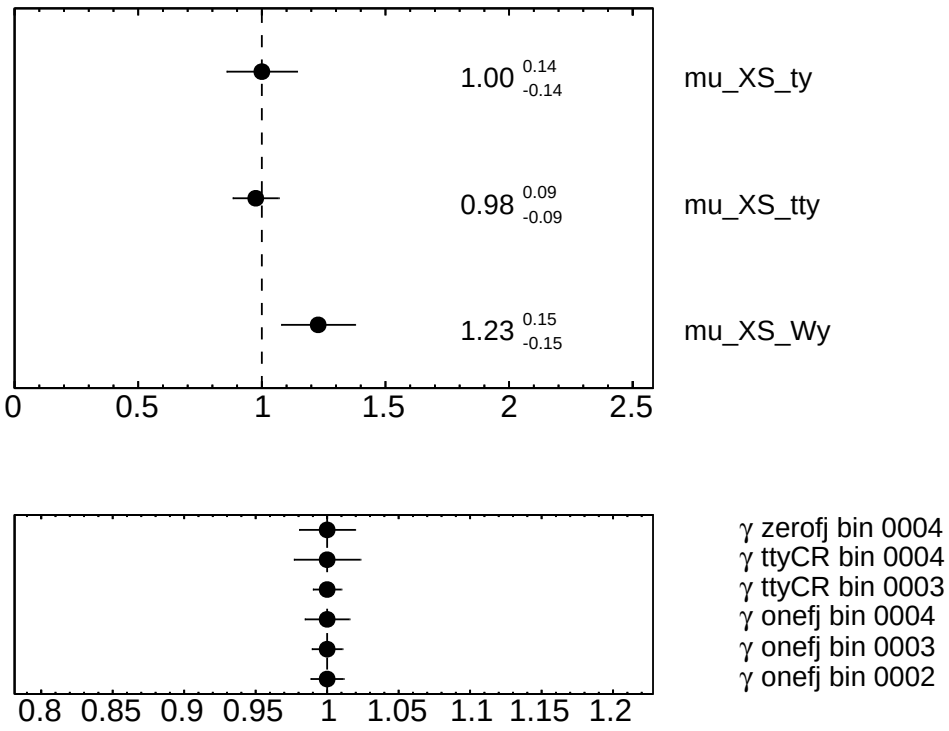

Figure 12.6: Normalization factors that are treated as free parameters in the Asimov fit and the value of the gamma factors that are assigned to each bin as nuisance parameter due to the limited MC sample statistic.

nuisance parameters having at least one correlation coefficient above 10% is shown in Figure 12.9. In general correlations are small, although there are several nuisance parameters correlated at the level of 40-70% which is not unexpected as several of them have large uncertainties that cause similar changes in the background prediction.

The norm factors and the γ-factors which describe the per-bin statistical uncertainties are shown in Figure 12.11. The best-fit value of $\mu_{t\bar{t}\gamma}$ is $0.98\ ^{+0.07}_{-0.07}$ and $\mu_{W\gamma}$ is $1.23\ ^{+0.13}_{-0.13}$.

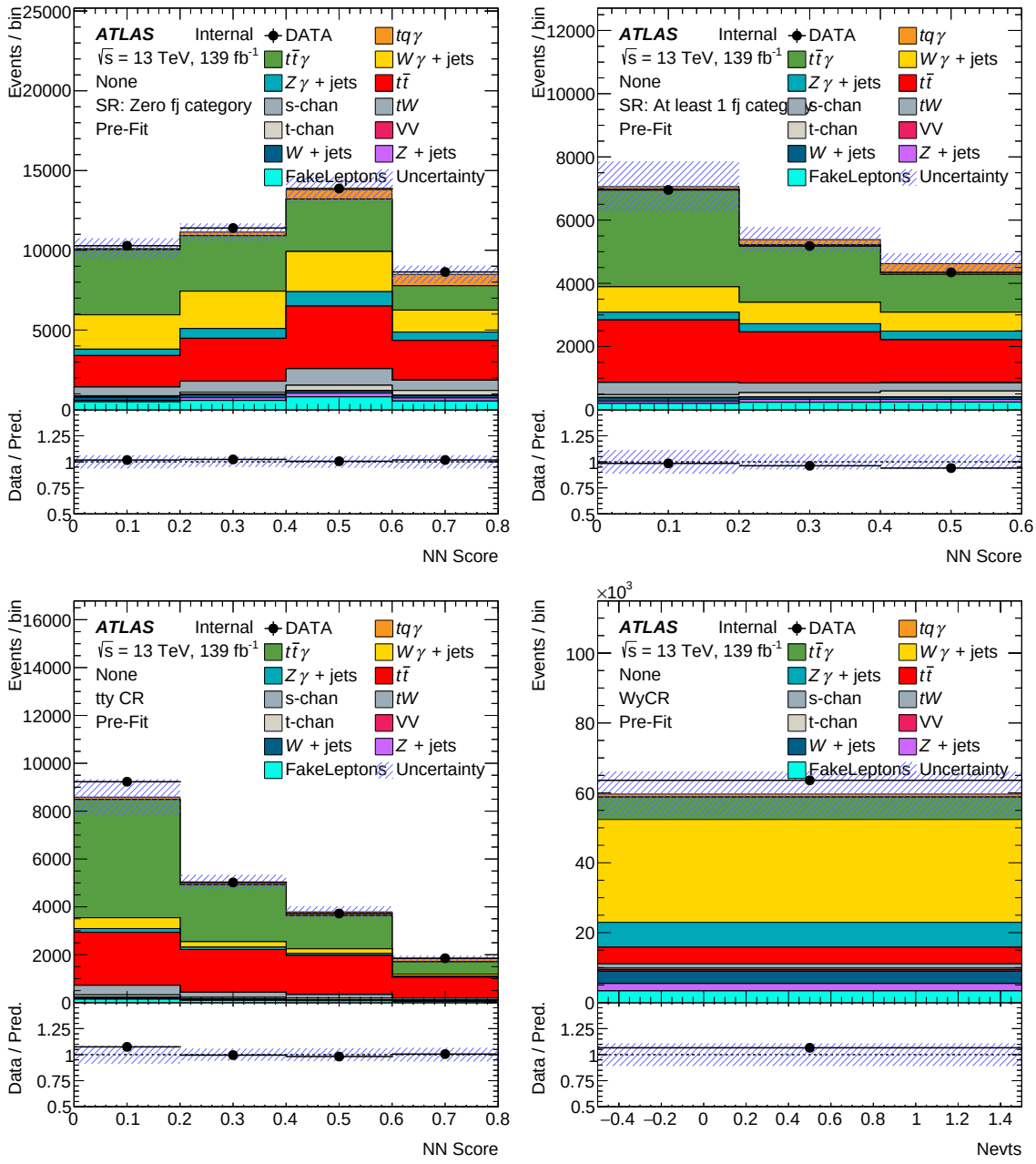

Figure 12.7: Pre-fit plots with data for bins with S/B $< 10\%$. Statistical and Systematic uncertainties are included in these plots.

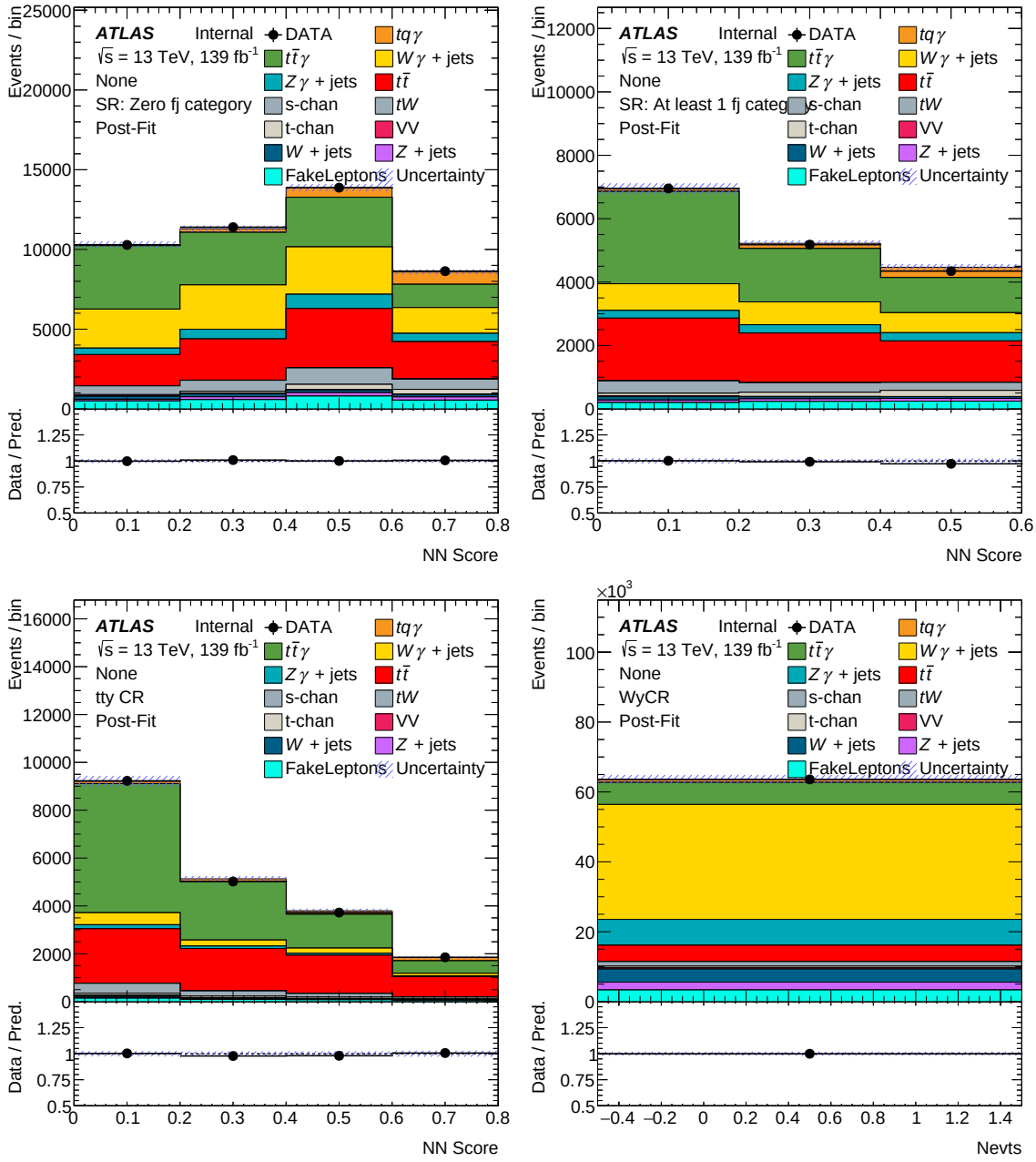

Figure 12.8: Post-fit distributions obtained from background-only fit to data for bins with S/B $< 10\%$. Statistical and Systematic uncertainties are included in these plots.

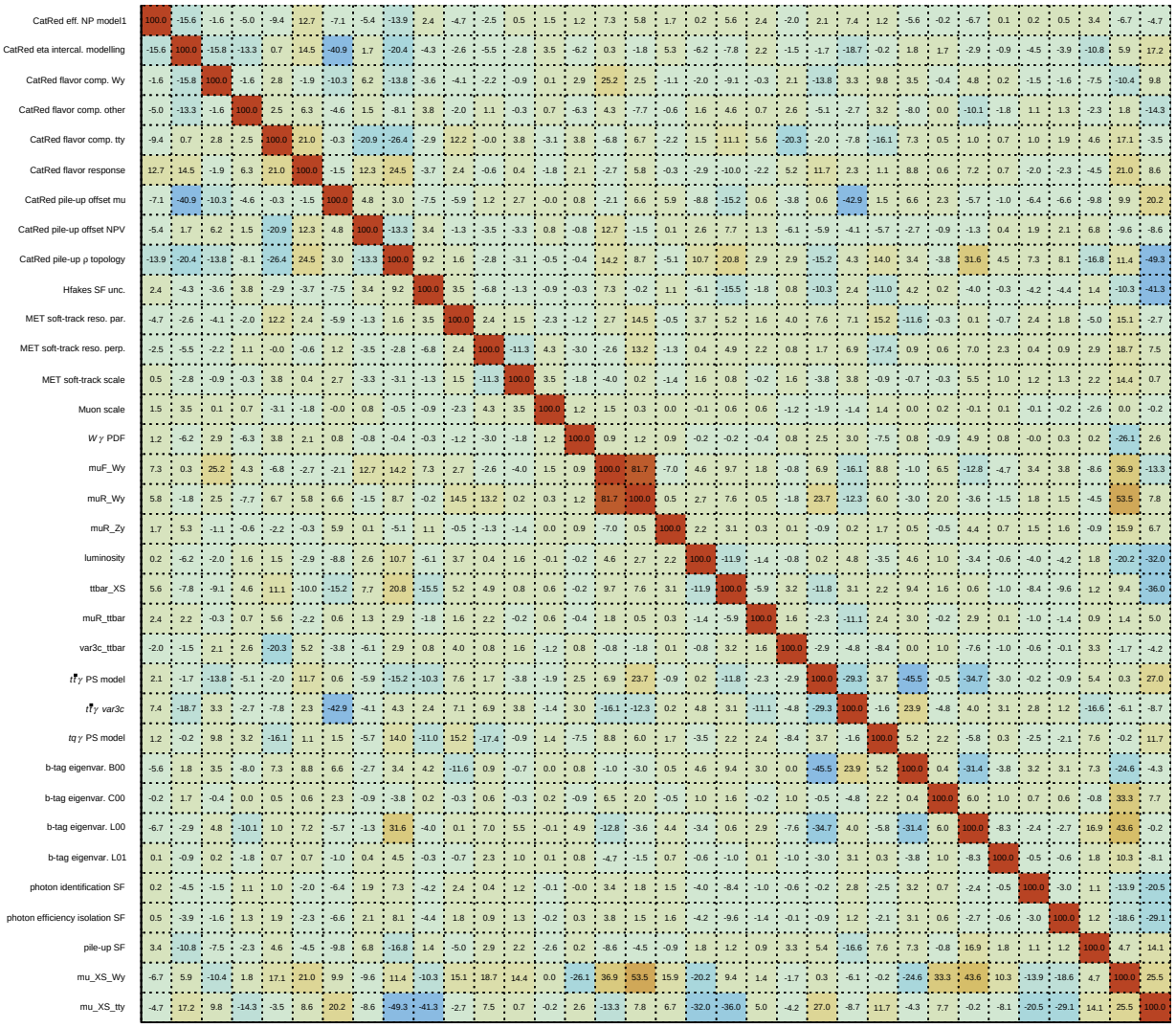

Figure 12.9: Correlation matrix of the nuisance parameters included in the background-only fit to data.

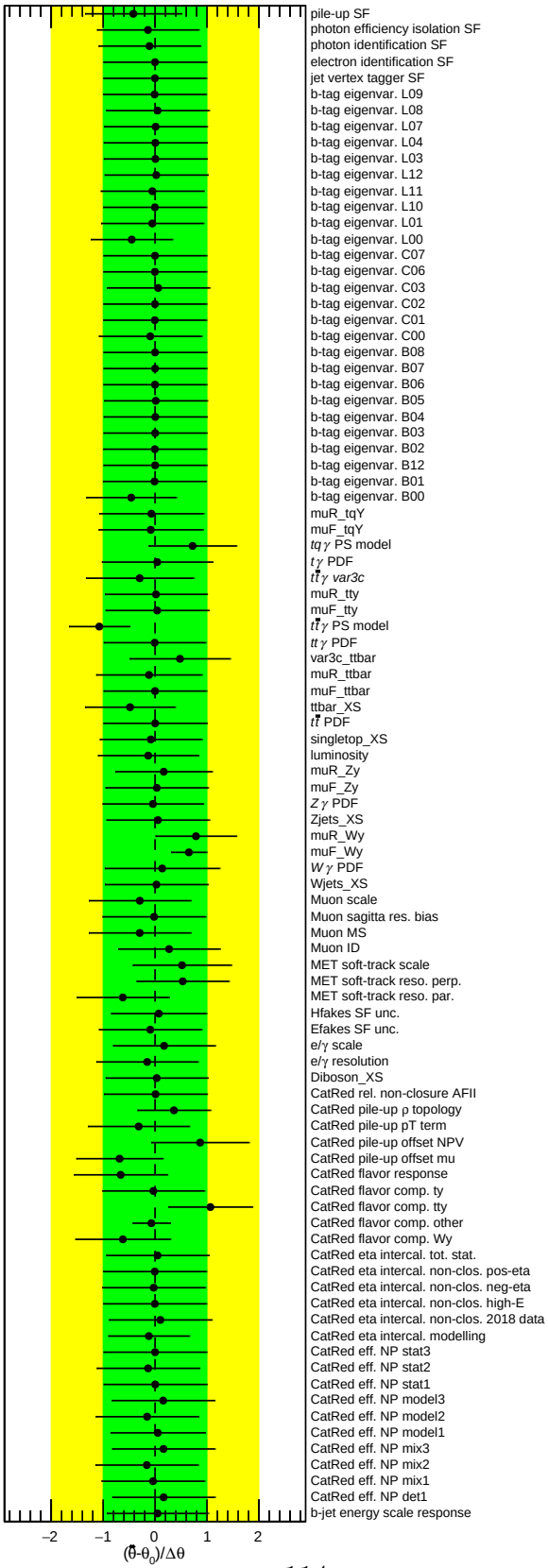

Figure 12.10: Pre- and post-fit values of the nuisance parameters considered in the background-only fit to data.

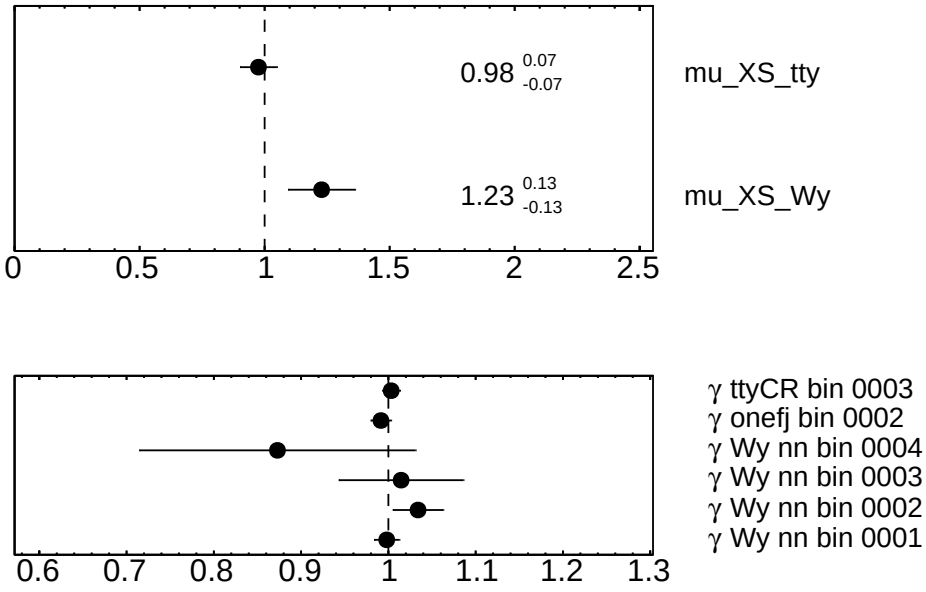

Figure 12.11: Normalization factors that are treated as free parameters in the background-only fit to data and the value of the gamma factors that are assigned to each bin as nuisance parameter due to the limited MC sample statistic.

Chapter Thirteen: Conclusion

A first ATLAS search for the associated production of a single top quark and a photon is presented in this dissertation. The analysis is based on the full Run-2 dataset of pp collisions at $\sqrt{s} = 13$ TeV collected by the ATLAS experiment at the CERN Large Hadron Collider and corresponding to an integrated luminosity of 139 fb^{-1}.

Major backgrounds for the signal are $t\bar{t}\gamma,\ W\gamma,\ t\bar{t}$. A small contribution from other processes like $Z\gamma,\ Z$+jets is also expected. Backgrounds with prompt photon and prompt lepton are estimated using simulation. For estimating backgrounds with fake photons, simulation is corrected using data-driven scale factors. In particular, for estimating fake photon backgrounds due to mis-reconstructed electrons, $e \to \gamma$ fake rates are measured in data and simulation in bins of η_γ and photon conversion type. Scale factor SF($e \to \gamma$) is obtained from the ratio of $e \to \gamma$ fake rate in data over that in simulation. For backgrounds with $j \to \gamma$ fakes, scale factors SF ($j \to \gamma$) are derived in bins of $\eta_\gamma,\ p_{T,\gamma}$ and photon conversion type using the ABCD method. SF($j \to \gamma$), defined as the ratio of number of events with a hadronic fake photon in data over that in simuation, is estimated from four regions A, B, C and D constructed using photon isolation and identification criteria. Dedicated control regions are used for validating $t\bar{t}\gamma$, $W\gamma$ backgrounds.

To optimize the sensitivity of the analysis, signal region events are classified into two categories based on the number of forward jets (0 fj or $\geq$1 fj). In each category, a neural network trained with kinematic and topological event variables is used to separate signal from background. Signal strength $\mu_{tq\gamma}$, defined as the ratio of measured $tq\gamma$ cross-section to the SM expectation, is extracted by performing a simultaneous profile likelihood fit to signal regions, $t\bar{t}\gamma$ CR and $W\gamma$ CR.

The expected best-fit value of the ratio of the observed $tq\gamma$ cross-section to that of the SM prediction is $1.0^{+0.14}_{-0.14} = 1.0\ ^{+0.05}_{-0.05}$ (stat.) $^{+0.13}_{-0.13}$ (syst.). This corresponds to a p-value of 6.5 σ for the no-signal hypothesis.

Part II

The combination of ATLAS searches for flavour changing neutral currents in $t \to Hq$ decays

Chapter Fourteen: Flavour Changing Neutral Currents in $t \to Hq$ decays

Flavour changing neutral current (FCNC) interactions, like the decay of a top quark to an up-type quark and a Higgs boson, are forbidden at tree level in the Standard Model (SM). These decays are possible at higher orders via loop diagrams, but highly suppressed compared to the dominant top quark decay mode ($t \to bW$) due to the Glashow-Iliopoulos-Maiani mechanism [89]. In the SM, the predicted branching ratios for $t \to qH$ decays are exceedingly small: $\mathscr{B}(t \to Hu) \sim 10^{-17}$ and $\mathscr{B}(t \to Hc) \sim 10^{-15}$ [90]. Thus, any observation of this process will be a clear hint towards the physics beyond the SM.

An examples of an FCNC process at tree level is shown in Figure 14.1.

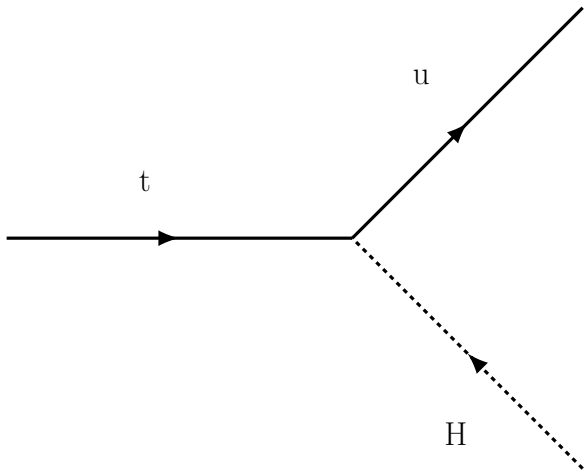

Figure 14.1: The diagram illustrates the tree level FCNC decay of the top quark. FCNC interactions like this decay are forbidden in the SM at tree level.

In many theories beyond the SM, large enhancements in $\mathscr{B}(t \to Hq)$ are possible due to contributions from loop diagrams mediated by new bosons. Examples include quark-singlet models[91–93], two-Higgs doublet model with (FC-2HDM) or without (FV-2HDM) flavour-conservation [94], the minimal supersymmetric model [95], supersymmetry models with R-parity violation [96], or models with warped extra di-

mensions [97]. Among them, the largest branching ratio, $\mathscr{B}(t \to Hc) \sim 1.5 \times 10^{-3}$, appears in the 2HDM in which the tree level FCNC coupling is not forbidden by any additional symmetry. The quoted branching ratio corresponds to a tree level coupling that scales with quark masses as $\lambda_{tHq} \sim \sqrt{2m_t m_q}/\nu$, where m_t is the top quark mass, m_q is the light up-type quark mass and ν is the SM Higgs field vacuum expectation value [98].

The ATLAS and CMS collaborations have performed searches [99–105] for $t \to Hq$ decays using 7, 8 and 13 TeV pp collision data collected during Run-1 and Run-2 of the LHC. These analyses primarily searched for $t\bar{t}$ events where one top quark decays via $t \to Wb$ and the other decays via $t \to Hq$. The Higgs boson is assumed to have a mass of 125 GeV and to decay as predicted by the SM. With Run-1 data, ATLAS obtained $\mathscr{B}(t \to Hc) < 0.46\%$ and $\mathscr{B}(t \to Hu) < 0.45\%$ [99] and CMS obtained $\mathscr{B}(t \to Hc) < 0.40\%$ and $\mathscr{B}(t \to Hu) < 0.55\%$ [101], in both cases at 95% confidence level (CL). Compared with Run-1, Run-2 searches benefit from the increased $t\bar{t}$ cross-section at $\sqrt{s} = 13$ TeV, as well as the larger integrated luminosity delivered by the LHC. Using 35.9 fb^{-1} of data at $\sqrt{s} = 13$ TeV, the CMS collaboration has performed a search using $t\bar{t} \to WbHq$ events targeting $H \to b\bar{b}$ decays, resulting in upper limits of $\mathscr{B}(t \to Hc) < 0.47\%$ and $\mathscr{B}(t \to Hu) < 0.47\%$ [102].

Using 36.1 fb^{-1} of data at $\sqrt{s} = 13$ TeV, the ATLAS collaboration has performed four analyses searching for $t\bar{t} \to WbHq$ events, and targeting $H \to b\bar{b}$, $H \to WW^*, \tau\tau, ZZ^*$, $H \to \gamma\gamma$, $H \to \tau\tau$ decay modes [103–105]. Results from the combination of these searches are presented in Chapter 15.

Chapter Fifteen: The combination of ATLAS searches for FCNC in $t \to Hq$ decays

The ATLAS collaboration has performed four searches for flavour changing neutral current decays of a top quark into an up-type quark ($q = u, c$) and the Standard Model Higgs boson ($t \to Hq$) using partial run-2 data, corresponding to an integrated luminosity of 36.1 fb^{-1} collected in 2015 and 16. All the analyses search for top-quark pair events in which one top quark decays into Wb and the other top quark decay into Hq. The targeted higgs decay modes in each analysis are:

- $H \to \gamma\gamma$ in both hadronic and leptonic $t\bar{t}$ decay channels [$tqH(\gamma\gamma)$] [103]
- $H \to WW^*, \tau\tau, ZZ^* \to$ leptons with either two same-sign light leptons or three light leptons [tqH(ML)] [104]
- $H \to \tau\tau$ [$tqH(\tau\tau)$] [105]
- $H \to b\bar{b}$ in the single lepton and opposite-sign dilepton $t\bar{t}$ decay channels [$tqH(b\bar{b})$] [105]

Here, light leptons refers to electrons and muons, including those from τ lepton decay.

Results from the combination of these four searches are presented in this chapter following a brief summary of individual FCNC analyses is Section 15.1.

15.1 Individual ATLAS FCNC searches

15.1.1 $tqH(\gamma\gamma)$ analysis

This FCNC analysis (documentation found in Ref. [103]) exploits the excellent diphoton mass resolution to identify $H \to \gamma\gamma$ decay over the continuum background. Major backgrounds for the signal are $\gamma\gamma j$, $t\bar{t}\gamma$, $W\gamma\gamma$ and $Z\gamma\gamma$. Based on the decay mode of the W boson, the analysis is split into two categories, namely, events with only one lepton in the final state (leptonic category) and events with no leptons in the final

state (hadronic category).

The two top quarks are reconstructed with corresponding masses (M_1, M_2) by forming three-body objects from photons, leptons, jets and MET. Signal and background events are separated by applying selection cuts on M_1 and M_2. As shown in Figure 15.1, an unbinned maximum likelihood fit is performed as a function of $m_{\gamma\gamma}$ to determine the best-fit value of the parameter of interest $\mu_{\gamma\gamma}$, defined as:

$$\mu_{\gamma\gamma} = \mathscr{B}(t \to qH) \tag{15.1}$$

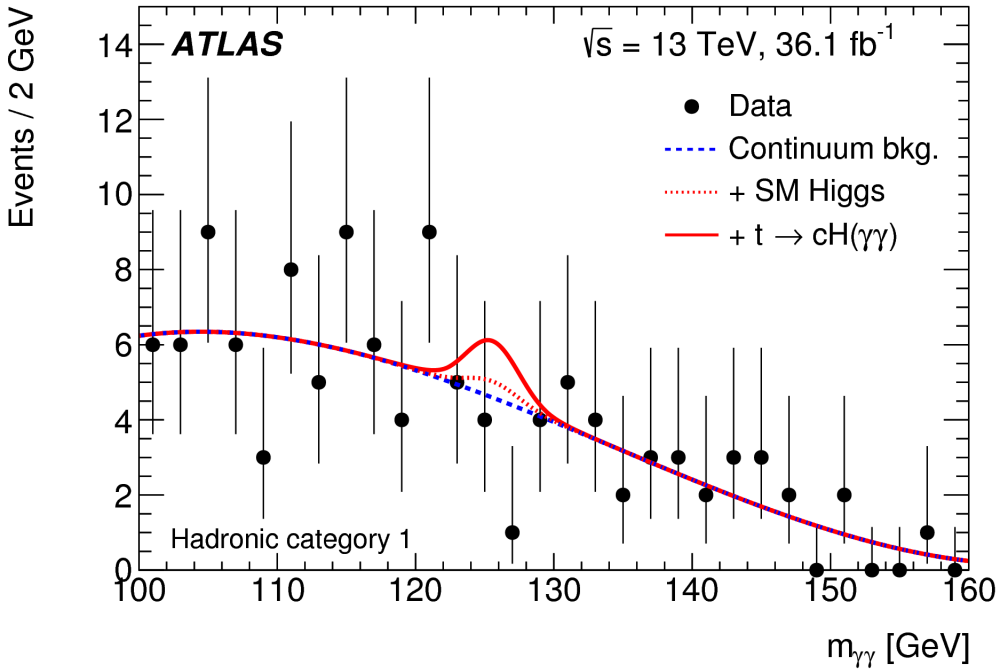

Figure 15.1: An unbinned maximum likelihood fit of $m_{\gamma\gamma}$ distribution to data

A total of 33 nuisance parameters (NP) are introduced in the construction of the likelihood function. Leading systematic uncertainties in this analysis are $t\bar{t}$ production cross-section, $\mathscr{B}(H \to \gamma\gamma)$, integrated luminosity and photon energy scale & resolution.

15.1.2 tqH(ML) analysis

This analysis (documentation found in Ref. [104]) exploits multilepton signatures resulting from Higgs decays to vector boson and/or τ leptons. Two final states are considered in this analysis: two same-sign light leptons(2ℓSS) and three light leptons (3ℓ). Events with τ_{had} are vetoed to avoid overlap with $tqH(\tau\tau)$ analysis.

Major backgrounds in this analysis are $t\bar{t}V$ and $t\bar{t}$ events with fake leptons. In each channel, two different Boosted Decision Tree (BDT) discriminants are constructed for separating signal events from $t\bar{t}V$ and $t\bar{t}$ backgrounds, respectively. Flavor and kinematic properties of leptons, jets & angular separations between them are used as the inputs to the BDT training. Figure 15.2 illustrates the BDT discriminant distribution for $t \to uH$ signal in the 3ℓ channel.

The distributions of BDT discriminants are fitted to data to determine the best-fit value of the parameter of interest μ_{ML}, that is defined as:

$$\mu_{ML} = \frac{\mathscr{B}(t \to qH)}{0.002} \tag{15.2}$$

A total of 152 nuisance parameters (NP) are introduced in the construction of the likelihood function.

15.1.3 $tqH(\tau\tau)$ analysis

This analysis (documentation found in Ref. [105]) is sensitive to $t\bar{t} \longrightarrow Wb + Hq$ events with $H \to \tau\tau$ and $W \to jj$. Major backgrounds in this analysis are due to fake τ-lepton bkgs from $t\bar{t}$ & QCD multijet production processes. Signal selection is optimized in four different categories based on the number of jets (exactly 3j or $\geq$ 4j) and the decay modes of τ leptons ($\tau_{had}\tau_{had}$ or $\tau_{lep}\tau_{had}$).

In each category, a BDT discriminant, constructed using variables like $m_{\tau\tau}$, m_{Hq}, is used for separating signal from the background. BDT discriminant distribution for the ($\tau_{had}\tau_{had}$, $3j$) category is shown in Figure 15.3.

The parameter of interest in this analysis is $\mu_{\tau\tau}$, defined as:

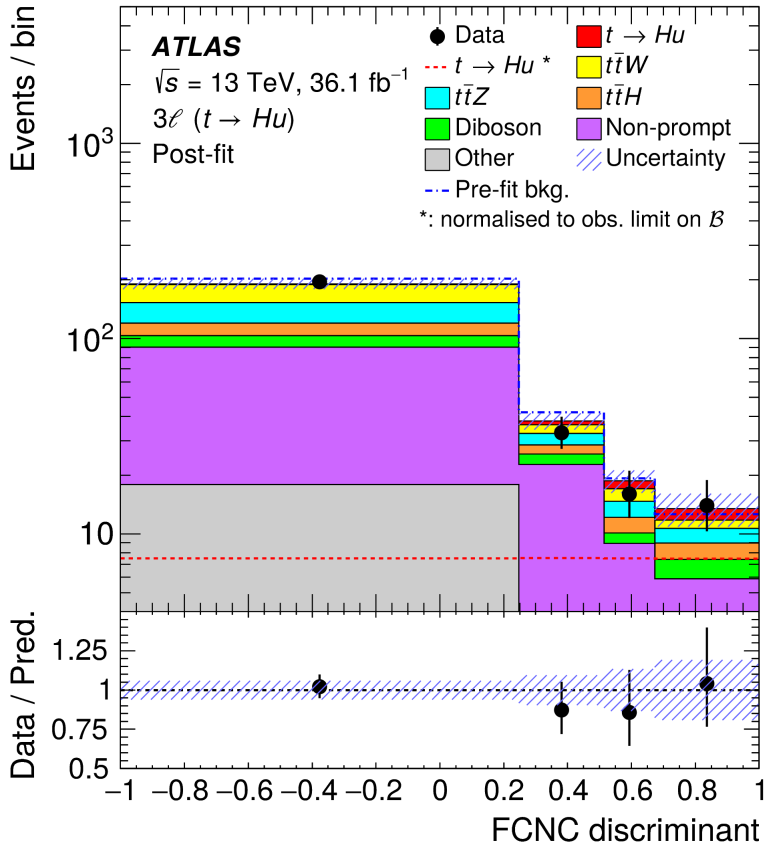

Figure 15.2: BDT discriminant distribution for $t \to uH$ signal in the 3ℓ channel

$$\mu_{\tau\tau} = \frac{\mathscr{B}(t \to qH)}{0.01} \tag{15.3}$$

A total of 109 nuisance parameters (NP) are introduced in the construction of the likelihood function.

15.1.4 $tqH(b\bar{b})$ analysis

This analysis (documentation found in Ref. [105]) targets $t\bar{t} \to WbHq$ process, with $H \to b\bar{b}$ and $W \to l\nu$. Events with exactly one lepton are selected. Major backgrounds for the signal arise due to $t\bar{t}$+jets and QCD multi-jet processes.

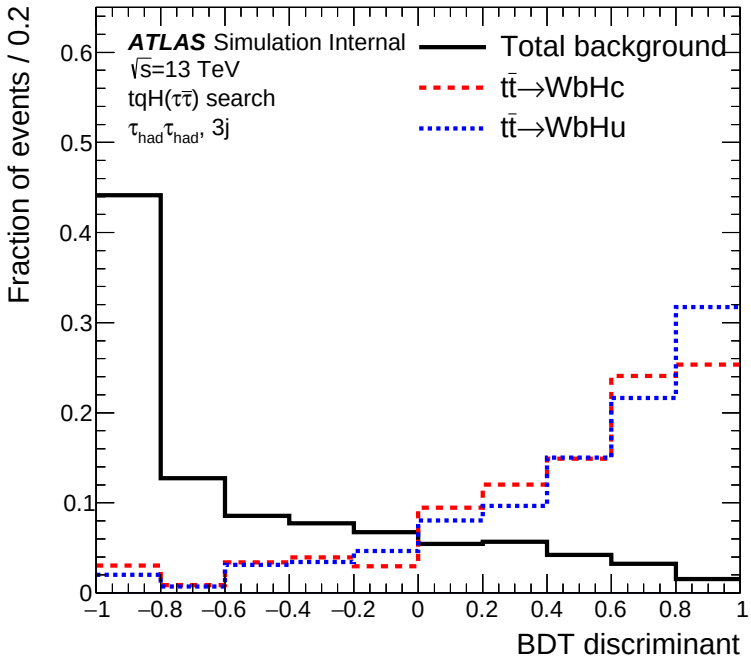

Figure 15.3: BDT discriminant distribution for the ($\tau_{had}\tau_{had}$, $3j$) category

Based on the number of jets (4, 5, ≥6) and b-tagged jets (2, 3, ≥4), this analysis is split in 9 different regions. In each region, a likelihood discriminant used to separate signal from the background. Invariant masses of leptons, jets and MET, and those corresponding to W, t and H resonances are used as the inputs for constructing the likelihood. BDT discriminant distribution for ($4j$, $2b$) category is shown in Figure 15.4.

The parameter of interest in this analysis is μ_{bb}:

$$\mu_{bb} = \frac{\mathscr{B}(t \to qH)}{0.005} \tag{15.4}$$

A total of 140 nuisance parameters (NP) are introduced in the construction of the likelihood function. Leading systematic uncertainties in this analysis are the b-tagging and c-tagging calibration uncertainties.

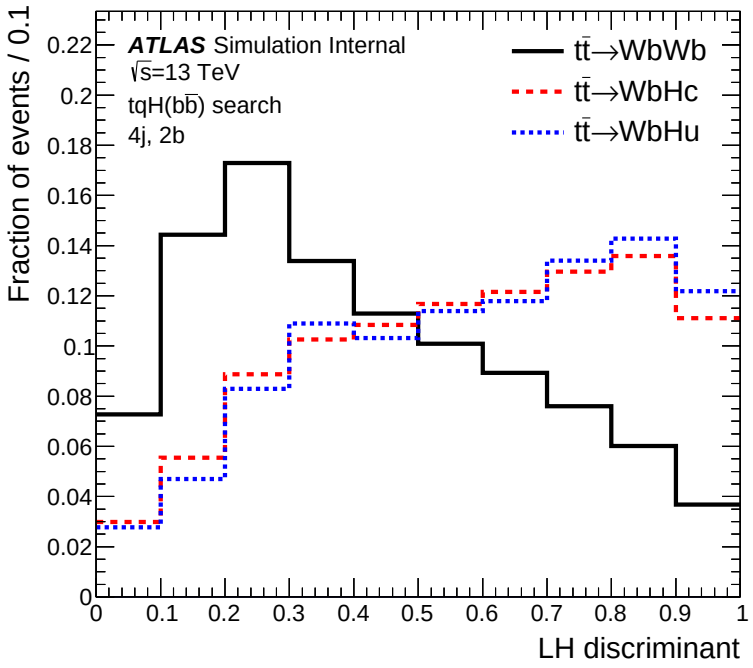

Figure 15.4: BDT discriminant distribution for $(4j,\ 2b)$ category

15.2 The Combination of ATLAS FCNC searches

A binned likelihood function $\mathcal{L}(\mathscr{B}_{comb}, \vec{\theta})$ is constructed by combining the distributions of discriminants from each individual analysis. The likelihood function depends on the signal-strength parameter $\mathscr{B}_{comb}$, defined as the branching ratio $\mathscr{B}$ of the decay $t \to c(u)H$, and nuisance parameters $\vec{\theta}$, denoting a continuous set of parameters that parametrise the effect of each systematic uncertainty on the signal and background expectations in each region.

As the parameter of interest (POI) is defined differently in each individual analysis, a parametrization scheme (shown in Table 15.1) is introduced in the combined workspace to correlate the signal strength parameter across all channels.

A total of 434 nuisance parameters are incorporated in the combined likelihood function. These are constrained by Gaussian or log-normal probability density functions in the likelihood fit.

Channel	Parametrization
$H \to \gamma\gamma$	$\mu_{\gamma\gamma} = 0.01 \times \mathscr{B}_{comb}$
$H \to WW^*, \tau\tau, ZZ^* \to$ leptons	$\mu_{ML} = 5 \times \mathscr{B}_{comb}$
$H \to \tau\tau$	$\mu_{\tau\tau} = 1 \times \mathscr{B}_{comb}$
$H \to b\bar{b}$	$\mu_{bb} = 2 \times \mathscr{B}_{comb}$

Table 15.1: Parametrization scheme for correlating POIs across all individual channels.

15.2.1 Correlation Schemes

The following correlation scheme for nuisance parameters has been implemented across all individual analyses.

- *Signal modelling systematics*: Uncertainties related to the signal cross section and the signal parton shower modelling are correlated across all analyses. Uncertainties due to the variation of initial state radiation/final state radiation (ISR/FSR) scales are also correlated
- *Jet Energy Resolution*: The NP corresponding to the Jet Energy Resolution uncertainty is correlated across all analyses
- *Jet Energy Scale*: 20 NPs corresponding to uncertainties on Jet Energy Scale are correlated across *bb*, $\tau\tau$ and multilepton analyses. (In $H \to \gamma\gamma$ analysis, Jet Energy Scale uncertainty is represented with only one 1NP. Thus, it is treated as uncorrelated in this analysis)
- *Jet Vertex Tagging*: The NP corresponding to the Jet Vertex Tagging uncertainty is correlated across all analyses
- *Luminosity & pileup reweighting scale factor*: The NPs related to the uncertainties on luminosity and the pileup reweighting scale factor are treated as correlated across all analyses
- *b-tagging*: Although all analyses use MV2c10 tagger, the b-tagging working points are different in each analysis: $H \to \gamma\gamma$ analysis uses 77% WP, $H \to bb$ analysis uses 60% WP, where as multilepton and $H \to \tau\tau$ analyses use 70%

WP. 27 NPs related to the flavour tagging uncertainties are correlated across bb, $\tau\tau$ and multilepton analyses.

- *Background modelling systematics*: The NPs related to background modelling systematics are kept uncorrelated as the composition of real and fake backgrounds is different across all analyses

As shown in Table 15.2, the above correlation scheme has negligible impact on the best fit value of the signal strength parameter.

Correlated NP	Asimov fit to $\mathscr{B}_{comb}$=0%	Asimov fit to $\mathscr{B}_{comb}$=0.2%
None (Only POI)	$0^{+0.04100}_{-0.07597}$	$0.2^{+0.056}_{-0.052}$
Luminosity	$0^{+0.04105}_{-0.07597}$	$0.2^{+0.056}_{-0.052}$
Jet Energy Resolution	$0^{+0.04101}_{-0.07579}$	$0.2^{+0.056}_{-0.052}$
Jet Vertex Tagger	$0^{+0.04100}_{-0.07593}$	$0.2^{+0.056}_{-0.052}$
Pileup Reweighting	$0^{+0.04106}_{-0.07591}$	$0.2^{+0.056}_{-0.052}$
Parton Shower Modelling	$0^{+0.04108}_{-0.07596}$	$0.2^{+0.057}_{-0.052}$
Signal cross-section	$0^{+0.04095}_{-0.07570}$	$0.2^{+0.057}_{-0.052}$
ISR/FSR	$0^{+0.04101}_{-0.07599}$	$0.2^{+0.057}_{-0.052}$
Jet Energy Scale (20 NPs)	$0^{+0.04073}_{-0.07529}$	$0.2^{+0.056}_{-0.052}$
Flavour-tagging (27 NPs)		$0.2^{+0.056}_{-0.052}$
All of above NPs	$0^{+0.04088}_{-0.07560}$	$0.2^{+0.056}_{-0.051}$

Table 15.2: Best fit value (Asimov) of $\mathscr{B}(t \to Hc)$ is shown for different correlation scenarios. Impact on $\mathscr{B}_{comb}$ due to the NP correlations is found to be negligible as the analysis is dominated by statistical uncertainties.

15.3 Results from the Combination

A binned profile likelihood fit is performed simultaneously in all channels to obtain the best fit value of the $t \to qH$ branching ratio($\hat{\mathscr{B}}$). Uncertainties on the $\hat{\mathscr{B}}$ measurement are determined by varying the test statistic $q_{\mathscr{B}}$, as defined in Equation 15.5, by one unit from its minimum. 95% CL upper limits on the branching ratio

$\mathscr{B}(t \rightarrow qH)$ are determined from the $q_{\mathscr{B}}$ distribution using the CL_s method.

$$q_{\mathscr{B}} = -2\ln\left[\mathcal{L}(\mathscr{B},\hat{\hat{\vec{\theta}}})/\mathcal{L}(\hat{\mathscr{B}},\hat{\vec{\theta}})\right], \tag{15.5}$$

where, $\hat{\mathscr{B}}$, $\hat{\vec{\theta}}$ are the branching ratio and nuisance parameter values obtained from the profile likelihood fit; $\hat{\hat{\vec{\theta}}}$ represent nuisance parameter values which maximizes the likelihood $\mathcal{L}$ for a given branching ratio $\mathscr{B}$.

Negative Log-likelihood (NLL) scan plot for Asimov and data fits are presented in Figures 15.5, 15.6 and 15.7.

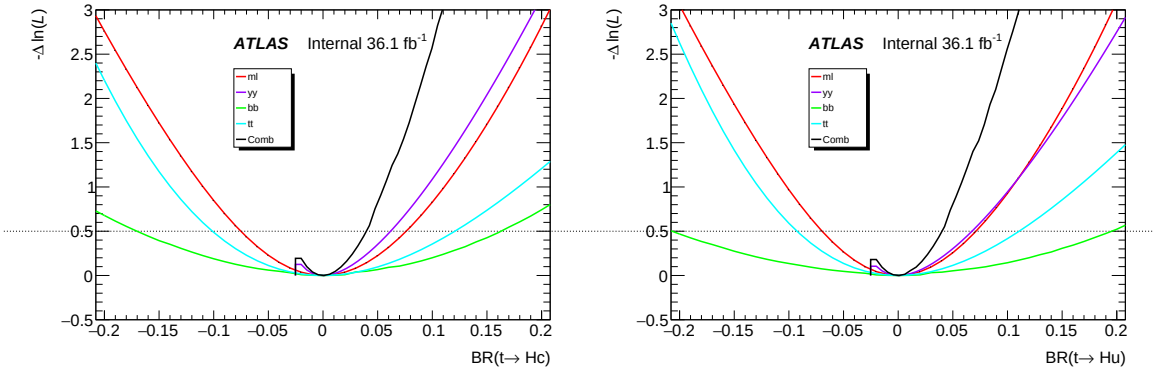

Figure 15.5: Negative Log-likelihood (NLL) scan plot for Asimov fit to $\mathscr{B}$= 0%.

The first set of combined results is obtained for each branching ratio separately, setting the other branching ratio to zero. The best-fit combined branching ratios are $\mathscr{B}(t \rightarrow cH) = 3.0^{+4.0}_{-3.4} \times 10^{-4}$ and $\mathscr{B}(t \rightarrow uH) = 4.2^{+4.2}_{-3.6} \times 10^{-4}$. A comparison of the best-fit branching ratios for the individual searches and their combination is shown in Table 15.3 and Figure 15.8 for $\mathscr{B}(t \rightarrow cH)$ and in Table 15.4 and Figure 15.9 for $\mathscr{B}(t \rightarrow uH)$.

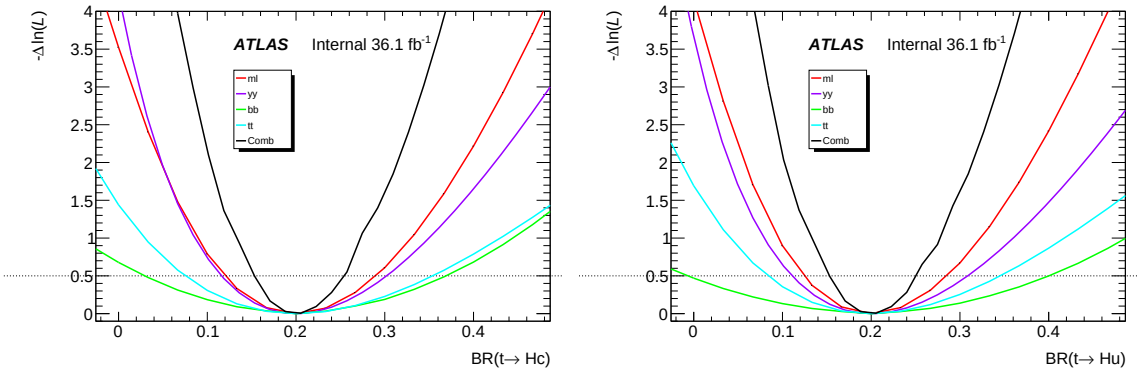

Figure 15.6: NLL scan plot for Asimov fit to $\mathscr{B}$= 0.2%.

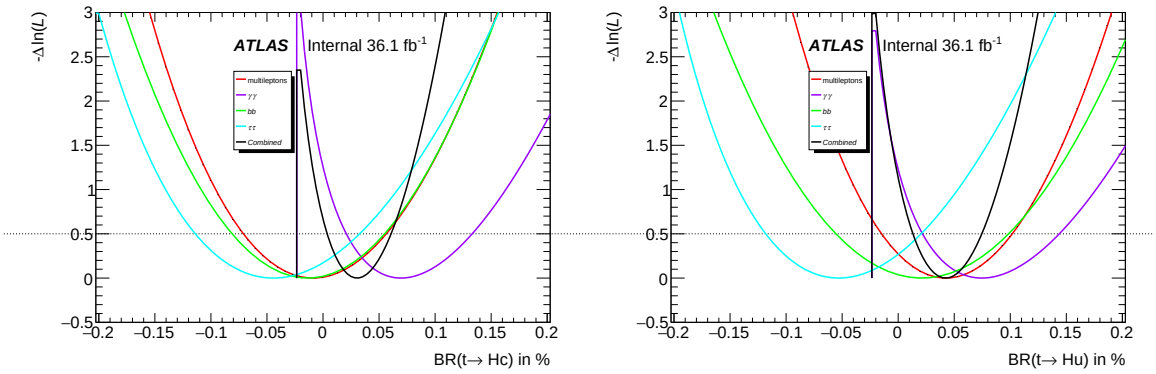

Figure 15.7: NLL scan plot for data fit.

Channel	Observed $\mathscr{B}(t \to cH)$	Expected $\mathscr{B}(t \to cH)$=0%	Expected $\mathscr{B}(t \to cH)$=0.2%
multilepton	$-0.82^{+8.0}_{-8.0} \times 10^{-4}$	$0^{+0.08}_{-0.07}$	$0.2^{+0.09}_{-0.08}$
$\gamma\gamma$	$6.9^{+7.4}_{-5.4} \times 10^{-4}$	$0^{+0.06}_{-0.02}$	$0.2^{+0.10}_{-0.08}$
$\tau\tau$	$-4.4^{+9.9}_{-8.5} \times 10^{-4}$	$0^{+0.12}_{-0.10}$	$0.2^{+0.15}_{-0.13}$
bb	$-0.2^{+2.3}_{-2.4} \times 10^{-3}$	$0^{+0.16}_{-0.17}$	$0.2^{+0.17}_{-0.17}$
Combination	$3.0^{+4.0}_{-3.4} \times 10^{-4}$	$0^{+0.04}_{-0.02}$	$0.2^{+0.06}_{-0.05}$

Table 15.3: Observed and Asimov (in %) fitted $\mathscr{B}(t \to cH)$ results are shown for individual analyses and their combination.

Channel	Observed $\mathscr{B}(t \to uH)$	Expected $\mathscr{B}(t \to uH)$=0%	Expected $\mathscr{B}(t \to uH)$=0.2%
multilepton	$4.2^{+7.6}_{-6.7} \times 10^{-4}$	$0^{+0.07}_{-0.07}$	$0.2^{+0.09}_{-0.08}$
$\gamma\gamma$	$7.5^{+8.1}_{-5.9} \times 10^{-4}$	$0^{+0.07}_{-0.02}$	$0.2^{+0.11}_{-0.09}$
$\tau\tau$	$-5.3^{+9.1}_{-7.8} \times 10^{-4}$	$0^{+0.11}_{-0.09}$	$0.2^{+0.15}_{-0.12}$
bb	$0.2^{+2.7}_{-3.0} \times 10^{-3}$	$0^{+0.20}_{-0.21}$	$0.2^{+0.20}_{-0.21}$
Combination	$4.2^{+4.2}_{-3.6} \times 10^{-4}$	$0^{+0.04}_{-0.02}$	$0.2^{+0.06}_{-0.05}$

Table 15.4: Observed and Asimov (in %) fitted $\mathscr{B}(t \to uH)$ results are shown for individual analyses and their combination.

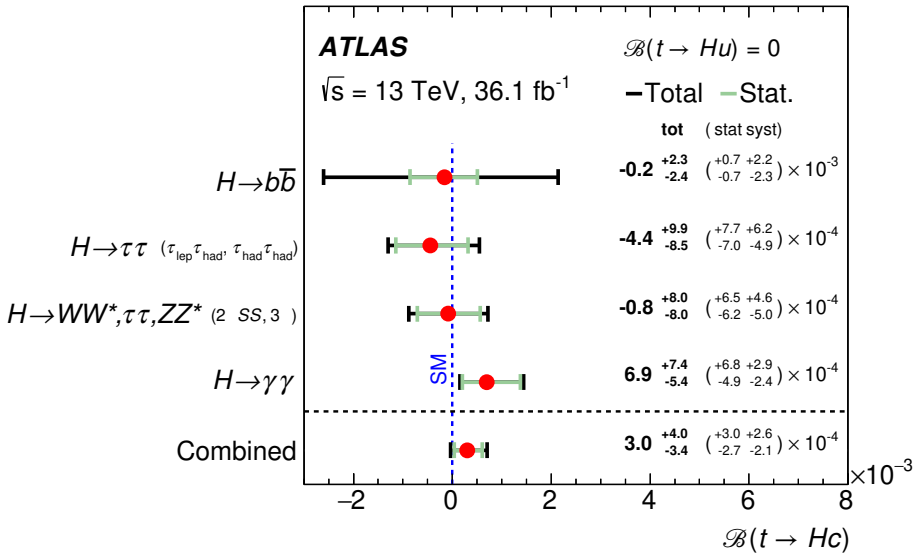

Figure 15.8: Best-fit $\mathscr{B}(t \to cH)$ for the individual analyses and their combination

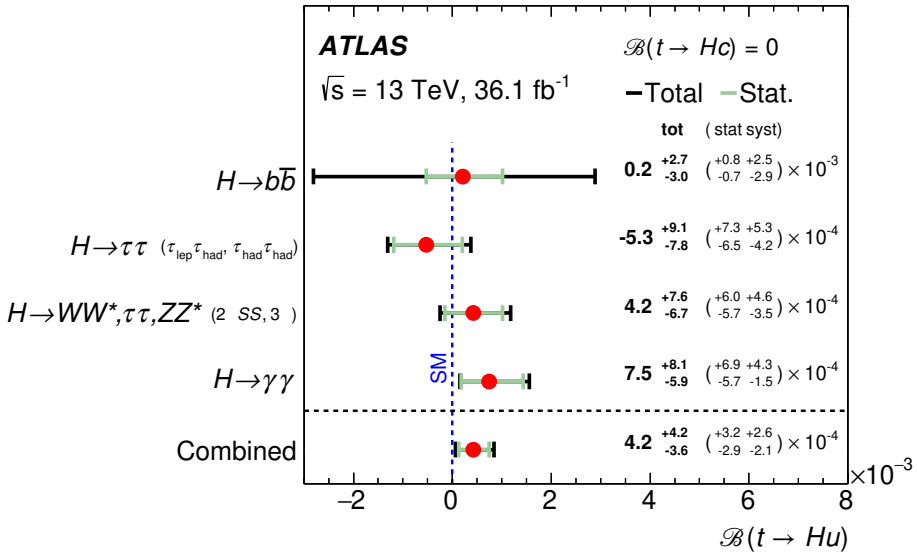

Figure 15.9: Best-fit $\mathscr{B}(t \to uH)$ for the individual analyses and their combination

The observed (expected) 95% CL combined upper limits on the branching ratios are $\mathscr{B}(t \to cH) < 1.1 \times 10^{-3}$ (8.3×10^{-4}) and $\mathscr{B}(t \to uH) < 1.2 \times 10^{-3}$ (8.3×10^{-4}).

A summary of the upper limits on the branching ratios obtained by the individual searches, as well as their combination, is illustrated in Figures 15.10 and 15.11.

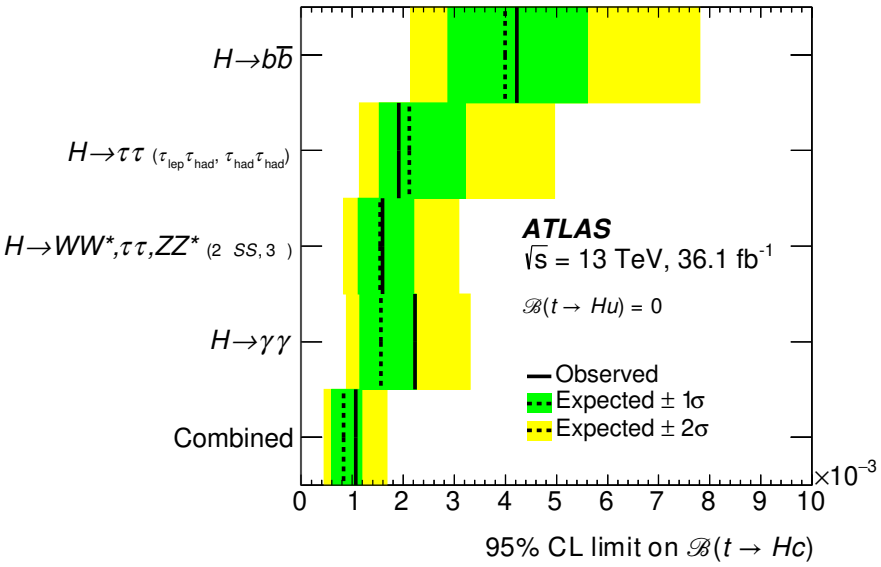

Figure 15.10: Observed and expected 95% CL upper limits on $\mathscr{B}(t \to cH)$ for individual searches and their combination.

Upper limits on the branching ratios $\mathscr{B}(t \to Hq)$ $(q = u, c)$ can be translated into upper limits on the non-flavour-diagonal Yukawa couplings λ_{tqH} appearing in the Lagrangian [106]:

$$\mathcal{L}_{\mathrm{FCNC}} = -\lambda_{t_{\mathrm{L}}q_{\mathrm{R}}}\bar{t}_{\mathrm{L}}q_{\mathrm{R}}H - \lambda_{q_{\mathrm{L}}t_{\mathrm{R}}}\bar{q}_{\mathrm{L}}t_{\mathrm{R}}H + \mathrm{h.c.}$$

Using the expression derived in Ref. [100], the coupling $|\lambda_{tqH}|$ can be extracted as $|\lambda_{tqH}| = (1.92 \pm 0.02)\sqrt{\mathscr{B}(t \to Hq)}$. The observed (expected) upper limits on the couplings from the combination of the searches are $|\lambda_{tcH}| < 0.064\,(0.055)$ and $|\lambda_{tuH}| < 0.066\,(0.055)$.

A similar set of results can be obtained by simultaneously varying both branching ratios in the likelihood function. Figure 15.12 shows the 95% CL upper limits on the branching ratios in the $\mathscr{B}(t \to Hu)$ versus $\mathscr{B}(t \to Hc)$ plane. The corre-

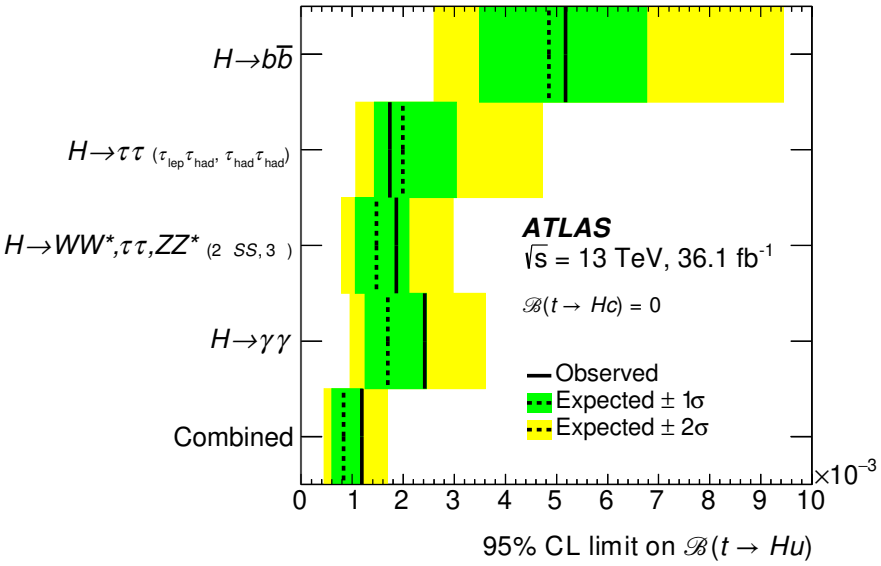

Figure 15.11: Observed and expected 95% CL upper limits on $\mathscr{B}(t \to uH)$ for individual searches and their combination.

sponding upper limits on the couplings in the $|\lambda_{tuH}|$ versus $|\lambda_{tcH}|$ plane are shown in Figure 15.13.

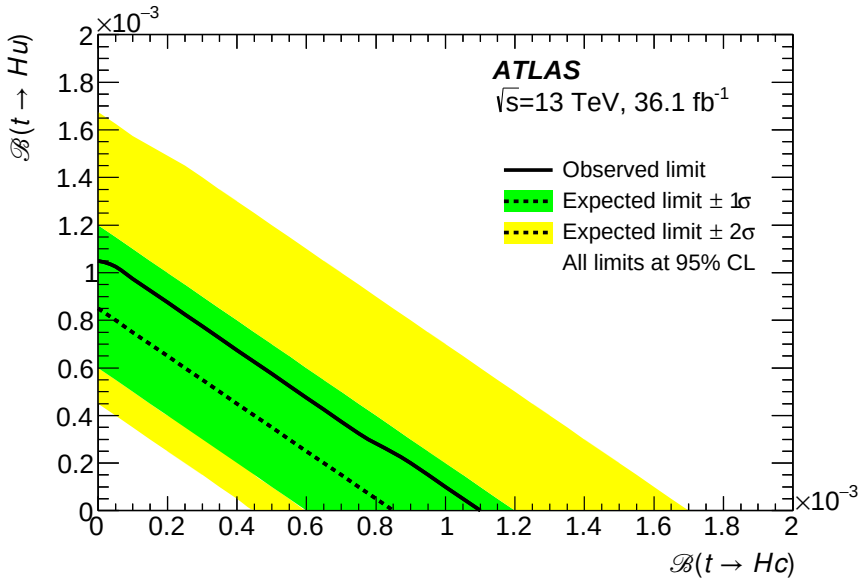

Figure 15.12: 95% upper limits on the plane of $\mathscr{B}(t \to cH)$ and $\mathscr{B}(t \to uH)$

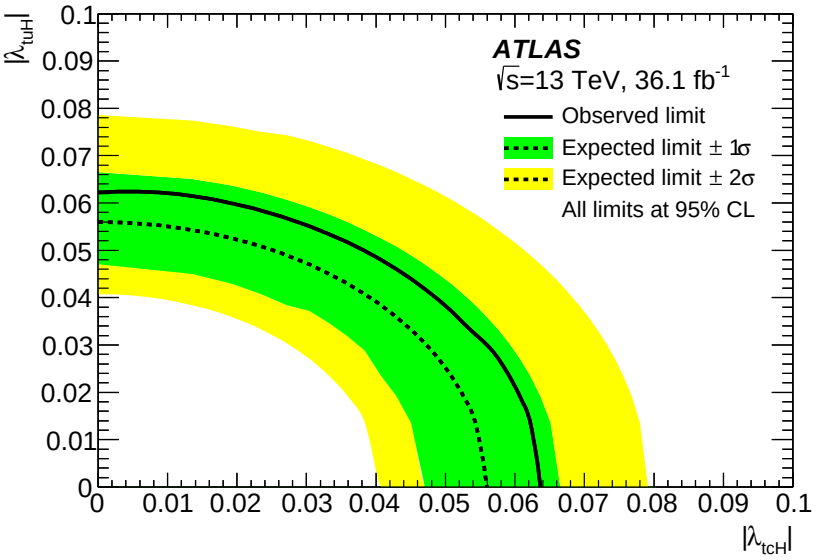

Figure 15.13: 95% upper limits on the plane of $|\lambda_{tcH}|$ and $|\lambda_{tuH}|$

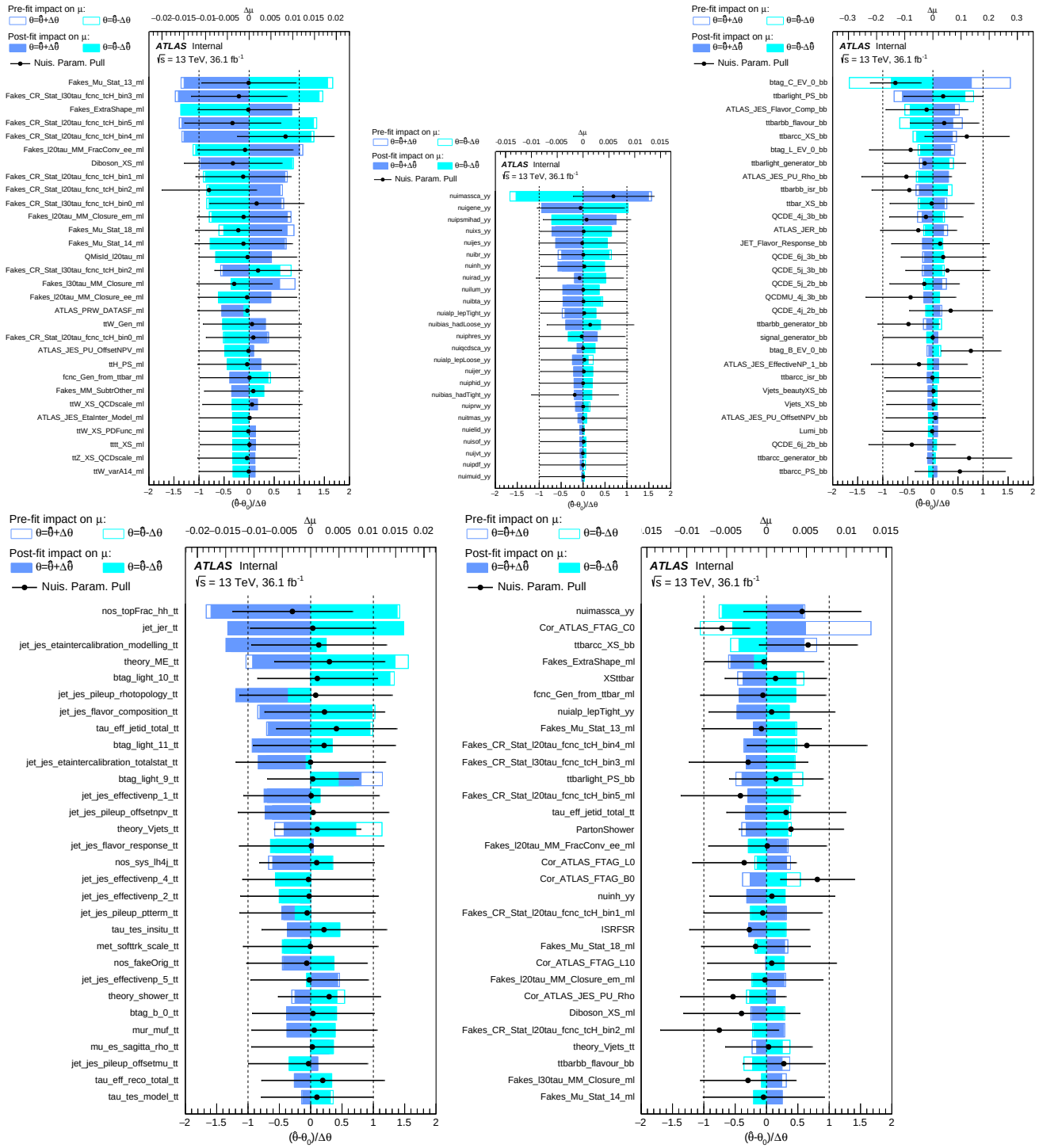

Figure 15.14: Nuisance parameter Ranking plot for $t \to Hc$ analyses (fit to Data); Top Row: Multilepton (left), $\gamma\gamma$ (Middle), bb (Right); Bottom Row: $\tau\tau$ (left), Combination (Right); Only systematic NPs are shown in the plot. NPs related to MC statistics are excluded in above plots

Ranking of the nuisance parameters included in the fit according to their impact on the measured branching ratio are shown in Figure 15.14 for $\mathscr{B}(t \to Hc)$ and in Figure 15.15 for $\mathscr{B}(t \to Hu)$.

Figure 15.16 shows the summary of the current 95% confidence level observed limits the branching ratios of the top quark decays via flavour changing neutral currents to a quark and a neutral boson $t \to Xq$ (X=g, Z, γ or H, q=u or c) by the ATLAS and CMS Collaborations compared to several new physics models.

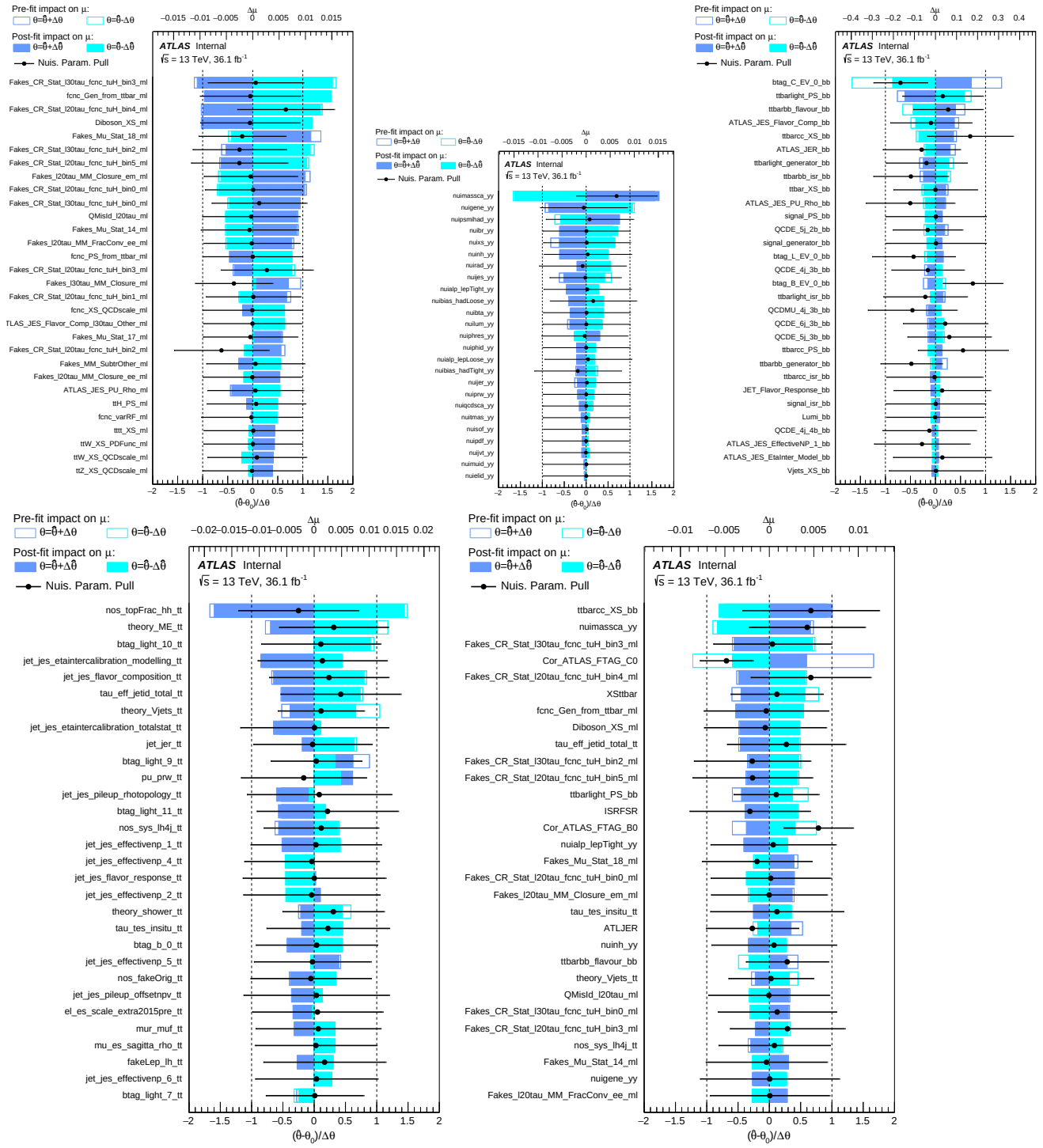

Figure 15.15: Nuisance parameter Ranking plot for $t \to uH$ analyses (fit to Data); Top Row: Multilepton (left), $\gamma\gamma$ (Middle), bb (Right); Bottom Row: $\tau\tau$ (left), Combination (Right); Only systematic NPs are shown in the plot. NPs related to MC statistics are excluded in above plots

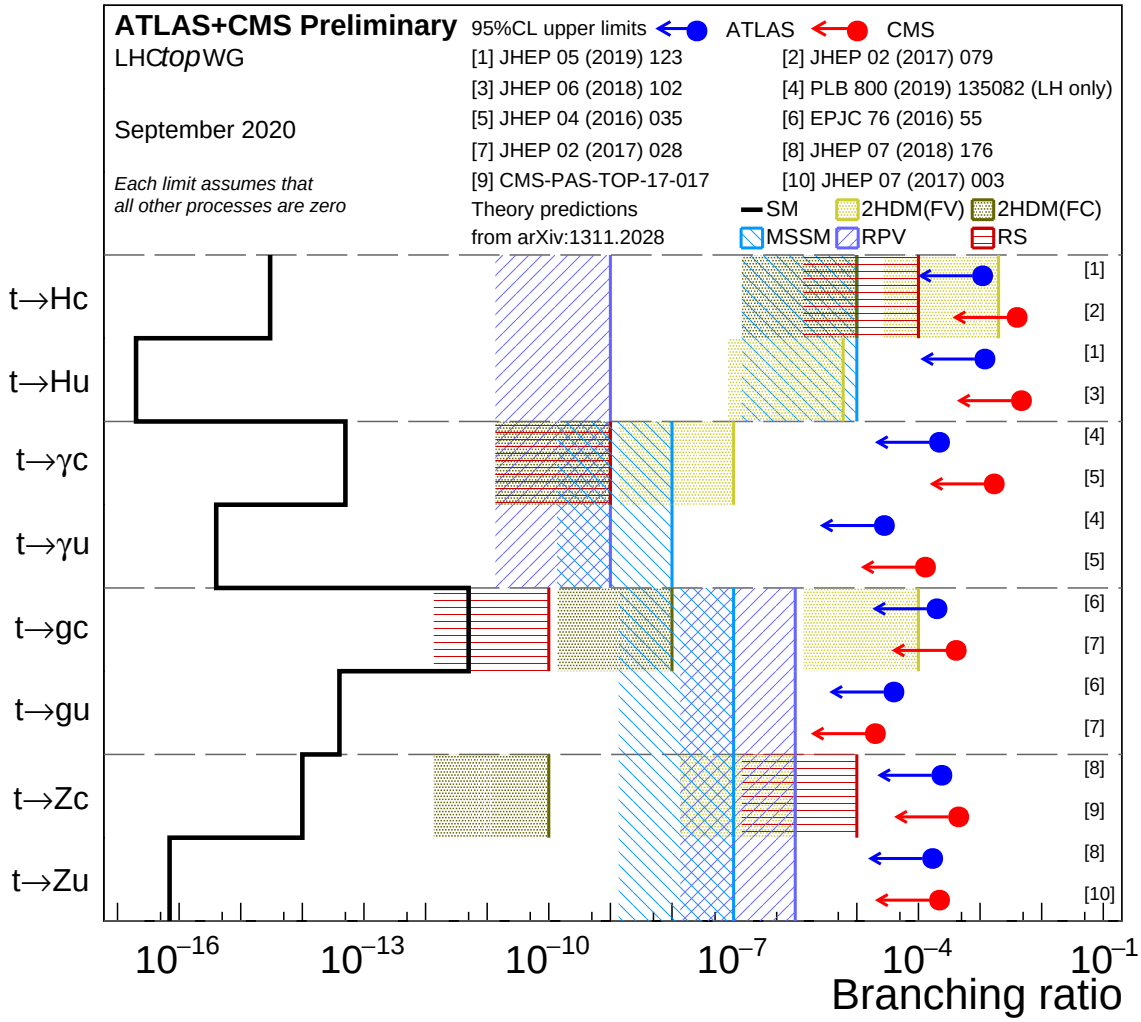

Figure 15.16: Summary of the current 95% confidence level observed limits on the $\mathscr{B}(t \to Xq)$ ($X = g,\ Z,\ \gamma$ or H; $q = u,\ c$) by the ATLAS and CMS Collaborations compared to several new physics models.

Chapter Sixteen: Conclusion

The combination of ATLAS searches for flavour-changing neutral-current decays of a top quark into an up-type quark ($q = u, c$) and the Standard Model Higgs boson, $t \to Hq$, is presented. Four ATLAS searches for $t\bar{t} \to WbHq$ events, probing the $H \to b\bar{b}$, $H \to WW^*, \tau\tau, ZZ^*$, $H \to \gamma\gamma$, $H \to \tau\tau$ decay modes, are considered in the combination.

The combined measurement yields observed (expected) 95% CL upper limits on the $t \to Hc$ and $t \to Hu$ branching ratios of 1.1×10^{-3} (8.3×10^{-4}) and 1.2×10^{-3} (8.3×10^{-4}), assuming $\mathscr{B}(t \to Hu)$ =0 and $\mathscr{B}(t \to Hc)$ =0 respectively. The corresponding combined observed (expected) upper limits on the $|\lambda_{tcH}|$ and $|\lambda_{tuH}|$ are 0.064 (0.055) and 0.066 (0.055) respectively. These results are the most restrictive direct bounds on tqH interactions measured to date.

Bibliography

1. Weinberg, S. A Model of Leptons. *Phys. Rev. Lett.* **19,** 1264–1266. https://link.aps.org/doi/10.1103/PhysRevLett.19.1264 (21 Nov. 1967) (cit. on p. 1).
2. Glashow, S. L. Partial-symmetries of weak interactions. *Nuclear Physics* **22,** 579–588. ISSN: 0029-5582. http://www.sciencedirect.com/science/article/pii/0029558261904692 (1961) (cit. on p. 1).
3. Salam, A. Weak and Electromagnetic Interactions. *Conf. Proc. C* **680519,** 367–377 (1968) (cit. on p. 1).
4. Arnison, G. *et al.* Experimental Observation of Isolated Large Transverse Energy Electrons with Associated Missing Energy at s**(1/2) = 540-GeV. *Phys. Lett. B* **122,** 103–116 (1983) (cit. on p. 2).
5. Banner, M. *et al.* Observation of Single Isolated Electrons of High Transverse Momentum in Events with Missing Transverse Energy at the CERN anti-p p Collider. *Phys. Lett. B* **122,** 476–485 (1983) (cit. on p. 2).
6. Bagnaia, P. *et al.* Evidence for Z0e+e at the CERN pp collider. *Physics Letters B* **129,** 130–140. ISSN: 0370-2693. http://www.sciencedirect.com/science/article/pii/037026938390744X (1983) (cit. on p. 2).
7. Arnison, G. *et al.* Experimental observation of lepton pairs of invariant mass around 95 GeV/c2 at the CERN SPS collider. *Physics Letters B* **126,** 398–410. ISSN: 0370-2693. http://www.sciencedirect.com/science/article/pii/0370269383901880 (1983) (cit. on p. 2).
8. Englert, F. & Brout, R. Broken Symmetry and the Mass of Gauge Vector Mesons. *Phys. Rev. Lett.* **13,** 321–323. https://link.aps.org/doi/10.1103/PhysRevLett.13.321 (9 Aug. 1964) (cit. on p. 2).
9. Higgs, P. W. Broken Symmetries and the Masses of Gauge Bosons. *Phys. Rev. Lett.* **13,** 508–509. https://link.aps.org/doi/10.1103/PhysRevLett.13.508 (16 Oct. 1964) (cit. on p. 2).

10. Higgs, P. Broken symmetries, massless particles and gauge fields. *Physics Letters* **12,** 132–133. ISSN: 0031-9163. http://www.sciencedirect.com/science/article/pii/0031916364911369 (1964) (cit. on p. 2).

11. ATLAS Collaboration. Observation of a new particle in the search for the Standard Model Higgs boson with the ATLAS detector at the LHC. *Phys. Lett. B* **716,** 1. arXiv: 1207.7214 [hep-ex] (2012) (cit. on p. 2).

12. CMS Collaboration. Observation of a new boson at a mass of 125 GeV with the CMS experiment at the LHC. *Phys. Lett. B* **716,** 30. arXiv: 1207.7235 [hep-ex] (2012) (cit. on p. 2).

13. ATLAS and CMS Collaborations. Combined Measurement of the Higgs Boson Mass in *pp* Collisions at $\sqrt{s} = 7$ and 8 TeV with the ATLAS and CMS Experiments. *Phys. Rev. Lett.* **114,** 191803. arXiv: 1503.07589 [hep-ex] (2015) (cit. on p. 2).

14. Group, P. D. *et al.* Review of Particle Physics. *Progress of Theoretical and Experimental Physics* **2020.** 083C01. ISSN: 2050-3911. eprint: https://academic.oup.com/ptep/article-pdf/2020/8/083C01/33653179/ptaa104.pdf. https://doi.org/10.1093/ptep/ptaa104 (Aug. 2020) (cit. on p. 4).

15. *Standard Model Summary Plots Summer 2019* tech. rep. ATL-PHYS-PUB-2019-024 (CERN, Geneva, July 2019). http://cds.cern.ch/record/2682186 (cit. on p. 5).

16. Sakharov, A. Violation of CP Invariance, C asymmetry, and baryon asymmetry of the universe. *Sov. Phys. Usp.* **34,** 392–393 (1991) (cit. on p. 4).

17. Rubin, V. C. & Ford W. Kent, J. Rotation of the Andromeda Nebula from a Spectroscopic Survey of Emission Regions. **159,** 379 (Feb. 1970) (cit. on p. 6).

18. Riess, A. G. *et al.* Observational Evidence from Supernovae for an Accelerating Universe and a Cosmological Constant. *The Astronomical Journal* **116,** 1009–1038. ISSN: 0004-6256. http://dx.doi.org/10.1086/300499 (Sept. 1998) (cit. on p. 6).

19. Perlmutter, S. *et al.* Measurements of Omega and Lambda from 42 High-Redshift Supernovae. *The Astrophysical Journal* **517,** 565–586. ISSN: 1538-4357. http://dx.doi.org/10.1086/307221 (June 1999) (cit. on p. 6).

20. Clowe, D. *et al.* A Direct Empirical Proof of the Existence of Dark Matter. *The Astrophysical Journal* **648,** L109–L113. ISSN: 1538-4357. http://dx.doi.org/10.1086/508162 (Aug. 2006) (cit. on p. 6).

21. Fukuda, Y. *et al.* Evidence for Oscillation of Atmospheric Neutrinos. *Phys. Rev. Lett.* **81,** 1562–1567. https://link.aps.org/doi/10.1103/PhysRevLett.81.1562 (8 Aug. 1998) (cit. on p. 6).

22. Branco, G. *et al.* Theory and phenomenology of two-Higgs-doublet models. *Phys. Rept.* **516,** 1–102. arXiv: 1106.0034 [hep-ph] (2012) (cit. on p. 7).

23. Evans, L. & Bryant, P. LHC Machine. *JINST* **3,** S08001 (2008) (cit. on p. 8).

24. Brüning, O. S. *et al. LHC Design Report* https://cds.cern.ch/record/782076 (CERN, Geneva, 2004) (cit. on p. 8).

25. Brüning, O. S. *et al. LHC Design Report* https://cds.cern.ch/record/815187 (CERN, Geneva, 2004) (cit. on p. 8).

26. Aamodt, K. *et al.* The ALICE experiment at the CERN LHC. *JINST* **3,** S08002 (2008) (cit. on p. 8).

27. Aad, G. *et al.* The ATLAS Experiment at the CERN Large Hadron Collider. *JINST* **3,** S08003 (2008) (cit. on pp. 8, 14–16, 19).

28. Chatrchyan, S. *et al.* The CMS Experiment at the CERN LHC. *JINST* **3,** S08004 (2008) (cit. on p. 8).

29. Alves A.Augusto, J. *et al.* The LHCb Detector at the LHC. *JINST* **3,** S08005 (2008) (cit. on p. 8).

30. Benedikt, M. *et al. LHC Design Report* https://cds.cern.ch/record/823808 (CERN, Geneva, 2004) (cit. on p. 8).

31. Lefèvre, C. *The CERN accelerator complex. Complexe des accélérateurs du CERN* Dec. 2008. https://cds.cern.ch/record/1260465 (cit. on p. 9).

32. Boussard, D. & Linnecar, T. P. R. *The LHC Superconducting RF System* tech. rep. LHC-Project-Report-316. CERN-LHC-Project-Report-316 (CERN, Geneva, Dec. 1999). https://cds.cern.ch/record/410377 (cit. on p. 9).

33. Herr, W. & Muratori, B. Concept of luminosity. https://cds.cern.ch/record/941318 (2006) (cit. on p. 10).

34. Goodson, J. *ATLAS magnetic systems* Apr. 2016. http://www.jetgoodson.com/images/thesisImages/magnetSystems.png (cit. on p. 14).

35. Haywood, S., Rossi, L., Nickerson, R. & Romaniouk, A. *ATLAS inner detector: Technical Design Report, 2* http://cds.cern.ch/record/331064 (CERN, Geneva, 1997) (cit. on p. 15).

36. Capeans, M. *et al. ATLAS Insertable B-Layer Technical Design Report* tech. rep. CERN-LHCC-2010-013. ATLAS-TDR-19 (Sept. 2010). https://cds.cern.ch/record/1291633 (cit. on p. 15).

37. *ATLAS liquid-argon calorimeter: Technical Design Report* https://cds.cern.ch/record/331061 (CERN, Geneva, 1996) (cit. on pp. 18, 20).

38. *ATLAS tile calorimeter: Technical Design Report* https://cds.cern.ch/record/331062 (CERN, Geneva, 1996) (cit. on p. 21).

39. Artamonov, A. *et al.* The ATLAS forward calorimeters. *JINST* **3,** P02010 (2008) (cit. on pp. 21, 22).

40. *ATLAS muon spectrometer: Technical Design Report* https://cds.cern.ch/record/331068 (CERN, Geneva, 1997) (cit. on p. 21).

41. Aad, G. *et al.* Performance of the ATLAS muon triggers in Run 2. *JINST* **15,** P09015. arXiv: 2004.13447 [hep-ex] (2020) (cit. on p. 23).

42. Bauer, F. *et al.* Construction and Test of MDT Chambers for the ATLAS Muon Spectrometer. *Nucl. Instrum. Meth. A* **461** (eds Batignani, G., Cervelli, F., Chiarelli, G. & Scribano, A.) 17–20. arXiv: 1604.02000 [physics.ins-det] (2001) (cit. on p. 22).

43. Argyropoulos, T. *et al.* Cathode strip chambers in ATLAS: Installation, commissioning and in situ performance. *IEEE Trans. Nucl. Sci.* **56,** 1568–1574 (2009) (cit. on p. 22).

44. Aielli, G. *et al.* The RPC first level muon trigger in the barrel of the ATLAS experiment. *Nucl. Phys. B Proc. Suppl.* **158** (eds Park, S., Ratti, S. & Santonico, R.) 11–15 (2006) (cit. on p. 22).

45. Majewski, S. R., Charpak, G., Breskin, A. & Mikenberg, G. A thin multiwire chamber operating in the high multiplication mode. *Nucl. Instrum. Methods Phys. Res.* **217,** 265–271. https://cds.cern.ch/record/149171 (1983) (cit. on p. 22).

46. Jenni, P., Nessi, M., Nordberg, M. & Smith, K. *ATLAS high-level trigger, data-acquisition and controls: Technical Design Report* https://cds.cern.ch/record/616089 (CERN, Geneva, 2003) (cit. on p. 24).

47. Panduro Vazquez, W. & Collaboration, A. *The ATLAS Data Acquisition system in LHC Run 2* tech. rep. ATL-DAQ-PROC-2017-007. 3 (CERN, Geneva, Feb. 2017). https://cds.cern.ch/record/2244345 (cit. on pp. 24, 25).

48. Cornelissen, T. *et al. Concepts, Design and Implementation of the ATLAS New Tracking (NEWT)* tech. rep. ATL-SOFT-PUB-2007-007. ATL-COM-SOFT-2007-002 (CERN, Geneva, Mar. 2007). https://cds.cern.ch/record/1020106 (cit. on p. 26).

49. ATLAS Collaboration. *The Optimization of ATLAS Track Reconstruction in Dense Environments* ATL-PHYS-PUB-2015-006. 2015. https://cds.cern.ch/record/2002609 (cit. on p. 26).

50. ATLAS Collaboration. Reconstruction of primary vertices at the ATLAS experiment in Run 1 proton–proton collisions at the LHC. *Eur. Phys. J. C* **77,** 332. arXiv: 1611.10235 [hep-ex] (2017) (cit. on p. 27).

51. ATLAS Collaboration. *Performance of primary vertex reconstruction in proton–proton collisions at* $\sqrt{s} = 7$ *TeV in the ATLAS experiment* ATLAS-CONF-2010-069. 2010. https://cds.cern.ch/record/1281344 (cit. on p. 27).

52. ATLAS Collaboration. Measurement of the photon identification efficiencies with the ATLAS detector using LHC Run 2 data collected in 2015 and 2016. *Eur. Phys. J. C* **79,** 205. arXiv: 1810.05087 [hep-ex] (2019) (cit. on p. 28).

53. ATLAS Collaboration. Electron and photon energy calibration with the ATLAS detector using 2015–2016 LHC proton–proton collision data. *JINST* **14,** P03017. arXiv: 1812.03848 [hep-ex] (2019) (cit. on pp. 28, 29, 58).

54. ATLAS Collaboration. Electron reconstruction and identification in the ATLAS experiment using the 2015 and 2016 LHC proton–proton collision data at $\sqrt{s} = 13\,\text{TeV}$. *Eur. Phys. J. C* **79,** 639. arXiv: 1902.04655 [hep-ex] (2019) (cit. on p. 28).

55. ATLAS Collaboration. *Properties of jets and inputs to jet reconstruction and calibration with the ATLAS detector using proton–proton collisions at* $\sqrt{s} = 13$ *TeV* ATL-PHYS-PUB-2015-036. 2015. https://cds.cern.ch/record/2044564 (cit. on p. 29).

56. Cacciari, M., Salam, G. P. & Soyez, G. The anti-k_t jet clustering algorithm. *JHEP* **04,** 063. arXiv: 0802.1189 [hep-ph] (2008) (cit. on p. 29).

57. ATLAS Collaboration. Jet energy scale measurements and their systematic uncertainties in proton–proton collisions at $\sqrt{s} = 13\,\text{TeV}$ with the ATLAS detector. *Phys. Rev. D* **96,** 072002. arXiv: 1703.09665 [hep-ex] (2017) (cit. on p. 29).

58. ATLAS Collaboration. *Tagging and suppression of pileup jets with the ATLAS detector* ATLAS-CONF-2014-018. 2014. https://cds.cern.ch/record/1700870 (cit. on p. 29).

59. ATLAS Collaboration. *Optimisation and performance studies of the ATLAS b-tagging algorithms for the 2017-18 LHC run* ATL-PHYS-PUB-2017-013. 2017. https://cds.cern.ch/record/2273281 (cit. on p. 29).

60. ATLAS Collaboration. ATLAS b-jet identification performance and efficiency measurement with $t\bar{t}$ events in pp collisions at $\sqrt{s} = 13\,\text{TeV}$. *Eur. Phys. J. C* **79,** 970. arXiv: 1907.05120 [hep-ex] (2019) (cit. on p. 29).

61. ATLAS Collaboration. Measurements of b-jet tagging efficiency with the ATLAS detector using $t\bar{t}$ events at $\sqrt{s} = 13\,\text{TeV}$. *JHEP* **08,** 089. arXiv: 1805.01845 [hep-ex] (2018) (cit. on p. 29).

62. ATLAS Collaboration. Muon reconstruction performance of the ATLAS detector in proton–proton collision data at $\sqrt{s} = 13\,\text{TeV}$. *Eur. Phys. J. C* **76,** 292. arXiv: 1603.05598 [hep-ex] (2016) (cit. on p. 31).

63. ATLAS Collaboration. E_T^{miss} *performance in the ATLAS detector using 2015–2016 LHC pp collisions* ATLAS-CONF-2018-023. 2018. https://cds.cern.ch/record/2625233 (cit. on p. 32).

64. Fael, M. & Gehrmann, T. Probing top quark electromagnetic dipole moments in single-top-plus-photon production. *Phys. Rev. D* **88,** 033003. https://link.aps.org/doi/10.1103/PhysRevD.88.033003 (3 Aug. 2013) (cit. on pp. 35, 36).

65. Etesami, S. M., Khatibi, S. & Najafabadi, M. M. Measuring anomalous $WW\gamma$ and $t\bar{t}\gamma$ couplings using top+γ production at the LHC. *The European Physical Journal C* **76.** ISSN: 1434-6052. http://dx.doi.org/10.1140/epjc/s10052-016-4376-2 (Sept. 2016) (cit. on p. 35).

66. CMS Collaboration. Evidence for the Associated Production of a Single Top Quark and a Photon in Proton–Proton Collisions at $\sqrt{s} = 13\,\text{TeV}$. *Phys. Rev. Lett.* **121,** 221802. arXiv: 1808.02913 [hep-ex] (2018) (cit. on p. 36).

67. Avoni, G. *et al.* The new LUCID-2 detector for luminosity measurement and monitoring in ATLAS. *JINST* **13,** P07017 (2018) (cit. on p. 38).

68. ATLAS Collaboration. Luminosity determination in pp collisions at $\sqrt{s} = 8\,\text{TeV}$ using the ATLAS detector at the LHC. *Eur. Phys. J. C* **76,** 653. arXiv: 1608.03953 [hep-ex] (2016) (cit. on p. 38).

69. ATLAS Collaboration. The ATLAS Simulation Infrastructure. *Eur. Phys. J. C* **70,** 823. arXiv: 1005.4568 [physics.ins-det] (2010) (cit. on p. 39).

70. Alwall, J. *et al.* The automated computation of tree-level and next-to-leading order differential cross sections, and their matching to parton shower simulations. *JHEP* **07,** 079. arXiv: 1405.0301 [hep-ph] (2014) (cit. on p. 39).

71. Sjöstrand, T. *et al.* An introduction to PYTHIA 8.2. *Comput. Phys. Commun.* **191,** 159. arXiv: 1410.3012 [hep-ph] (2015) (cit. on p. 39).

72. Lange, D. J. The EvtGen particle decay simulation package. *Nuclear Instruments and Methods in Physics Research Section A: Accelerators, Spectrometers, Detectors and Associated Equipment* **462.** BEAUTY2000, Proceedings of the 7th Int. Conf. on B-Physics at Hadron Machines, 152–155. ISSN: 0168-9002. http://www.sciencedirect.com/science/article/pii/S0168900201000894 (2001) (cit. on p. 39).

73. ATLAS Collaboration. *ATLAS Pythia 8 tunes to 7 TeV data* ATL-PHYS-PUB-2014-021. 2014. https://cds.cern.ch/record/1966419 (cit. on p. 40).

74. Ball, R. D. *et al.* Parton distributions with LHC data. *Nucl. Phys. B* **867,** 244. arXiv: 1207.1303 [hep-ph] (2013) (cit. on p. 40).

75. Ball, R. D. *et al.* Parton distributions for the LHC Run II. *JHEP* **04,** 040. arXiv: 1410.8849 [hep-ph] (2015) (cit. on p. 40).

76. Bevilacqua, G. *et al.* Hard Photons in Hadroproduction of Top Quarks with Realistic Final States. *JHEP* **10,** 158. arXiv: 1803.09916 [hep-ph] (2018) (cit. on p. 40).

77. Gleisberg, T. *et al.* Event generation with SHERPA 1.1. *JHEP* **02,** 007. arXiv: 0811.4622 [hep-ph] (2009) (cit. on p. 40).

78. Höche, S., Krauss, F., Schumann, S. & Siegert, F. QCD matrix elements and truncated showers. *JHEP* **05,** 053. arXiv: 0903.1219 [hep-ph] (2009) (cit. on p. 40).

79. Nason, P. A new method for combining NLO QCD with shower Monte Carlo algorithms. *JHEP* **11,** 040. arXiv: hep-ph/0409146 (2004) (cit. on p. 40).

80. Frixione, S., Nason, P. & Oleari, C. Matching NLO QCD computations with parton shower simulations: the POWHEG method. *JHEP* **11,** 070. arXiv: 0709.2092 [hep-ph] (2007) (cit. on p. 40).

81. Alioli, S., Nason, P., Oleari, C. & Re, E. A general framework for implementing NLO calculations in shower Monte Carlo programs: the POWHEG BOX. *JHEP* **06,** 043. arXiv: 1002.2581 [hep-ph] (2010) (cit. on p. 40).

82. Czakon, M. & Mitov, A. Top++: A program for the calculation of the top-pair cross-section at hadron colliders. *Comput. Phys. Commun.* **185,** 2930. arXiv: 1112.5675 [hep-ph] (2014) (cit. on p. 40).

83. Kidonakis, N. NNLL resummation for s-channel single top quark production. *Phys. Rev. D* **81,** 054028. arXiv: 1001.5034 [hep-ph] (2010) (cit. on p. 40).

84. Kidonakis, N. Two-loop soft anomalous dimensions for single top quark associated production with a W- or H-. *Phys. Rev. D* **82,** 054018. arXiv: 1005.4451 [hep-ph] (2010) (cit. on p. 40).

85. Kidonakis, N. Next-to-next-to-leading-order collinear and soft gluon corrections for t-channel single top quark production. *Phys. Rev. D* **83,** 091503. arXiv: 1103.2792 [hep-ph] (2011) (cit. on p. 40).

86. ATLAS Collaboration. *Measurement of $W^{\pm}$ and Z Boson Production Cross Sections in pp Collisions at $\sqrt{s} = 13$ TeV with the ATLAS Detector* ATLAS-CONF-2015-039. 2015. https://cds.cern.ch/record/2045487 (cit. on p. 40).

87. Agostinelli, S. *et al.* GEANT4 – a simulation toolkit. *Nucl. Instrum. Meth. A* **506,** 250 (2003) (cit. on p. 40).

88. ATLAS Collaboration. *Photon identification in 2015 ATLAS data* ATL-PHYS-PUB-2016-014. 2016. https://cds.cern.ch/record/2203125 (cit. on p. 93).

89. Glashow, S., Iliopoulos, J. & Maiani, L. Weak Interactions with Lepton-Hadron Symmetry. *Phys. Rev. D* **2,** 1285–1292 (1970) (cit. on p. 118).

90. Aguilar-Saavedra, J. Top flavor-changing neutral interactions: Theoretical expectations and experimental detection. *Acta Phys. Polon. B* **35** (eds del Aguila, F., Pittau, R., Djouadi, A. & Papadopoulos, C.) 2695–2710. arXiv: hep-ph/0409342 (2004) (cit. on p. 118).

91. Aguilar-Saavedra, J. & Nobre, B. Rare top decays t —> c gamma, t —> cg and CKM unitarity. *Phys. Lett. B* **553,** 251–260. arXiv: hep-ph/0210360 (2003) (cit. on p. 118).

92. Del Aguila, F., Aguilar-Saavedra, J. & Miquel, R. Constraints on top couplings in models with exotic quarks. *Phys. Rev. Lett.* **82,** 1628–1631. arXiv: hep-ph/9808400 (1999) (cit. on p. 118).

93. Aguilar-Saavedra, J. Effects of mixing with quark singlets. *Phys. Rev. D* **67.** [Erratum: Phys.Rev.D 69, 099901 (2004)], 035003. arXiv: hep-ph/0210112 (2003) (cit. on p. 118).

94. Béjar, S., Guasch, J. & Solà, J. Loop induced flavor changing neutral decays of the top quark in a general two-Higgs-doublet model. *Nuclear Physics B* **600,** 21–38. ISSN: 0550-3213. http://dx.doi.org/10.1016/S0550-3213(01)00044-X (Apr. 2001) (cit. on p. 118).

95. Guasch, J. & Sola, J. FCNC top quark decays: A Door to SUSY physics in high luminosity colliders? *Nucl. Phys. B* **562,** 3–28. arXiv: hep-ph/9906268 (1999) (cit. on p. 118).

96. Yang, J. M., Young, B.-L. & Zhang, X. Flavor changing top quark decays in r parity violating SUSY. *Phys. Rev. D* **58,** 055001. arXiv: hep-ph/9705341 (1998) (cit. on p. 118).

97. Agashe, K., Perez, G. & Soni, A. Collider Signals of Top Quark Flavor Violation from a Warped Extra Dimension. *Phys. Rev. D* **75,** 015002. arXiv: hep-ph/0606293 (2007) (cit. on p. 119).

98. Cheng, T. & Sher, M. Mass Matrix Ansatz and Flavor Nonconservation in Models with Multiple Higgs Doublets. *Phys. Rev. D* **35,** 3484 (1987) (cit. on p. 119).

99. Aad, G. *et al.* Search for flavour-changing neutral current top quark decays $t \to Hq$ in pp collisions at $\sqrt{s} = 8$ TeV with the ATLAS detector. *JHEP* **12,** 061. arXiv: 1509.06047 [hep-ex] (2015) (cit. on p. 119).

100. Aad, G. *et al.* Search for top quark decays $t \to qH$ with $H \to \gamma\gamma$ using the ATLAS detector. *JHEP* **06,** 008. arXiv: 1403.6293 [hep-ex] (2014) (cit. on pp. 119, 132).

101. Khachatryan, V. *et al.* Search for top quark decays via Higgs-boson-mediated flavor-changing neutral currents in pp collisions at $\sqrt{s} = 8$ TeV. *JHEP* **02,** 079. arXiv: 1610.04857 [hep-ex] (2017) (cit. on p. 119).

102. Sirunyan, A. M. *et al.* Search for the flavor-changing neutral current interactions of the top quark and the Higgs boson which decays into a pair of b quarks at $\sqrt{s} = 13$ TeV. *JHEP* **06,** 102. arXiv: 1712.02399 [hep-ex] (2018) (cit. on p. 119).

103. Aaboud, M. *et al.* Search for top quark decays $t \to qH$, with $H \to \gamma\gamma$, in $\sqrt{s} = 13$ TeV pp collisions using the ATLAS detector. *JHEP* **10,** 129. arXiv: 1707.01404 [hep-ex] (2017) (cit. on pp. 119, 120).

104. Aaboud, M. *et al.* Search for flavor-changing neutral currents in top quark decays $t \to Hc$ and $t \to Hu$ in multilepton final states in proton-proton collisions at $\sqrt{s} = 13$ TeV with the ATLAS detector. *Phys. Rev. D* **98,** 032002. arXiv: 1805.03483 [hep-ex] (2018) (cit. on pp. 119, 120, 122).

105. Aaboud, M. *et al.* Search for top-quark decays $t \to Hq$ with 36 fb^{-1} of pp collision data at $\sqrt{s} = 13$ TeV with the ATLAS detector. *JHEP* **05,** 123. arXiv: 1812.11568 [hep-ex] (2019) (cit. on pp. 119, 120, 122, 123).

106. Harnik, R., Kopp, J. & Zupan, J. Flavor Violating Higgs Decays. *JHEP* **03,** 026. arXiv: 1209.1397 [hep-ph] (2013) (cit. on p. 132).